A staggered finite volume method for the Euler equations using an acoustic-transport operator splitting

A. El Halabi[†], T. Galié[⋆], S. Kokh[♯], and K. Saleh[‡]

[†]Université Paris-Saclay, CEA, Service de Thermo-hydraulique et de Mécanique des Fluides, 91191, Gif-sur-Yvette, France — ahmad.elhalabi@cea.fr

[⋆]Université Paris-Saclay, CEA, Service de Thermo-hydraulique et de Mécanique des Fluides, 91191, Gif-sur-Yvette, France — thomas.galie@cea.fr

[♯]Université Paris-Saclay, Maison de la Simulation, 91191, Gif-sur-Yvette, France — samuel.kokh@cea.fr

[‡]Institut de Mathématiques de Marseille, Aix Marseille Université, site de Saint-Charles, 3 Place Victor Hugo, 13331 Marseille, France — khaled.saleh@univ-amu.fr

July 8, 2026

Abstract

This work addresses the simulation of compressible flows on unstructured meshes across a wide range of Mach numbers. To this end, we propose a staggered finite volume method for the compressible Euler equations in both barotropic and full formulations. Over the staggered grid, cell-centered unknowns include density, pressure, and energy, while face-centered variables represent velocity related quantities. The method is based on a Lagrange-projection like acoustic-transport splitting combined with a Suliciu-type relaxation approximation for the acoustic subsystem. Internal and kinetic energies are discretized on distinct sets of degrees of freedom, and a corrective mechanism is introduced to ensure consistency with the total energy conservation in the full Euler case. The proposed approach preserves the conservation properties of the compressible Euler equations, remains applicable to general equations of state, and satisfies key stability conditions: positivity of density (for barotropic and full systems), positivity of internal energy (for the full system), compliance with the second law of thermodynamics (globally for the barotropic system and both globally and locally for the full system), and local conservation of the total energy on the dual mesh for the full Euler equations. The time step is constrained only by the material velocity, and each time update requires solving a single linear system for the pressure. The low-Mach-number behavior of the scheme is analyzed, and the preservation of constant pressure–velocity profiles is established for stiffened-gas equations of state. The performance and robustness of the method are illustrated through numerical experiments for both barotropic and full Euler equations, in one and two space dimensions, on structured and unstructured meshes, over a wide range of Mach numbers including the low-Mach regime.

Contents

1 Introduction

This work is concerned with the design of discretization techniques for the Euler equations of compressible gas dynamics. These equations are relevant in many applications across a wide range of flow regimes in terms of Mach numbers. Indeed, some applications may require accounting for strong pressure effects while others involve near-incompressible flows.

Achieving a uniformly accurate and robust discretization across such regimes remains a difficult task. Conventional approaches typically rely on cell-centered finite volume formulations [73, 91, 41], which naturally ensure conservation properties at the discrete level. However, these methods can require specific adaptations to maintain accuracy and stability in regimes where compressibility effects are weak (see, for example, [92, 69, 48, 47, 74, 83, 30, 82, 49, 26, 31, 15, 67, 33, 10, 8, 90, 66]). Different arguments have been brought in the literature to examine these issues including: the analysis of the viscosity matrix associated with the discretization [92, 77], asymptotic expansion with respect to the Mach number [69, 48], a careful study in [30] that aims at transposing to the discrete level invariance properties of the continuous equations [85] and the design of numerical methods that satisfy the so-called Asymptotic Preserving property [63] for example in [49, 26, 67, 33, 90, 8].

An alternative to the standard cell-centered approach consists in adopting staggered discretizations for the compressible equations of gas dynamics. These methods, originally introduced in the context of incompressible flows [53], associate scalar quantities such as density and pressure with cell centers, while velocity components are defined on cell faces. Since their adaptation to compressible flows [52, 51], staggered schemes have been employed in a variety of contexts and have demonstrated good performance over a broad spectrum of Mach numbers (see for example [95, 60]). Nevertheless, they must be used with care, as they generally do not satisfy all the conservation properties of the compressible Euler equations, and may encounter difficulties when approximating shock waves [55].

Although staggered-grid finite volume schemes have been widely used since their early developments, few theoretical results were available until recently. Over the past years, several contributions have improved the mathematical understanding and practical robustness of such methods. Among these advances, we mention the following non-exhaustive list of references. For compressible barotropic models, stability results were established in [36, 38], and an explicit finite-volume approach using fluxes derived from kinetic considerations with stability properties was proposed in [5]. For the full compressible Euler equations, strategies including the energy equation were introduced in a semi-implicit form in [55], and subsequently in explicit formulations in [58, 42, 76]. More recently, the design of high-order staggered-grid schemes has been investigated in [89, 29, 28, 76, 39, 72, 11, 12].

A fundamental difficulty arises from the fact that, in a staggered formulation, internal and kinetic energies are not defined on the same set of discrete degrees of freedom. This separation complicates the consistent and conservative computation of total energy, which is central to the physical fidelity of compressible flow simulations. Various contributions have been proposed to address this issue, leading to formulations that ensure total energy conservation either globally [56, 29, 61, 59, 28] or locally [42, 57, 43].

In the present work, we propose a finite volume method based on a staggered discretization and applicable on unstructured meshes. The scheme is designed to preserve the conservation properties of the compressible Euler equations, either in their barotropic or full form, while remaining applicable to general Equations Of State (EOS). Particular attention is paid to maintain accuracy in a large range of Mach number regime. The time step is constrained only by the material velocity, and each iteration involves the resolution of a single linear system for the pressure. The method satisfies key stability properties: positivity of the density for both the barotropic and full Euler systems, positivity of the internal energy for the full Euler system, compliance with the second law of thermodynamics (globally for the barotropic case, globally and locally for the full system), and local conservation of the total energy for the full Euler system.

In the present work, we adopt the framework introduced in [50], combining a separate treatment of acoustic and transport phenomena through an operator splitting [2, 64, 35, 15, 19, 9] with a staggered finite volume scheme. The resulting method is reminiscent of the Lagrange-Projection technique [15, 19, 4], although it does not involve any moving mesh. The spatial discretization of our scheme draws inspiration from the schemes developed in [37, 56, 58, 55] which were based on projection methods. More specifically, for the full Euler system, the internal energy that is used as a main variable is updated by accounting for a corrective term that ensures the consistency with the total energy conservation. The operator splitting offers a straightforward IMEX (Implicit-Explicit) time integration strategy in the lines of [25, 15, 19]. The acoustic effects are treated implicitly, which allows for large time steps while maintaining stability, whereas the transport phenomena are advanced explicitly. Furthermore, a Suliciu-type relaxation approximation [87, 7, 16, 24] is employed for the acoustic subsystem, so that the implicit step involves only the solution of a linear system.

The paper is organized as follows. In Section 2, we recall the acoustic-transport splitting approximation of the barotropic Euler equations. Section 3 presents the discretization strategy, including the definition of the staggered mesh, the discrete unknowns, and the time update algorithm. In Section 4, we introduce the staggered Lagrange-projection like (SLP) scheme for the barotropic system, describing successively the acoustic and transport steps and discussing the main properties of the overall method. Section 5 extends the approach to the full Euler equations, detailing the splitting formulation, the discretization of each subsystem, and the resulting SLP scheme. Section 7 is devoted to the analysis of the scheme behavior in the low Mach regime. In section 8 we show that the SLP scheme preserves constant pressure-velocity profiles for Stiffened Gas, while Section 6 focuses on the local conservation of the total energy over the dual mesh for the full Euler system. Finally, a set of numerical experiments is presented in section 9 for both the barotropic and full Euler equations: the study includes convergence tests on one-dimensional problems as the spatial discretization is refined, as well as simulations in one and two dimensions on structured and unstructured meshes over a wide range of Mach regimes.

2 Acoustic-transport splitting approximation of the barotropic Euler equations

We consider the barotropic Euler system of gas dynamics

$$
\begin{cases}
\partial_t \rho + \boldsymbol{\nabla} \cdot (\rho \mathbf{u}) = 0, & \text{(1a)}\\
\partial_t (\rho \mathbf{u}) + \boldsymbol{\nabla} \cdot (\rho \mathbf{u} \otimes \mathbf{u}) + \boldsymbol{\nabla} p = \mathbf{0}, & \text{(1b)}
\end{cases}
$$

where ρ, $\mathbf{u}$ and p are respectively the density, the velocity, and the pressure of the fluid. We suppose that $\rho > 0$ and that the fluid is equipped with a barotropic equation of state in the form of a barotropic potential $\tau \mapsto e^{\mathrm{EOS}}(\tau)$, where $\tau = 1/\rho$ is the specific volume. We suppose that e^{EOS} verifies

$$
\frac{\mathrm{d}e^{\mathrm{EOS}}}{\mathrm{d}\tau} < 0, \qquad \frac{\mathrm{d}^2 e^{\mathrm{EOS}}}{\mathrm{d}\tau^2} > 0, \qquad \frac{\mathrm{d}^3 e^{\mathrm{EOS}}}{\mathrm{d}\tau^3} < 0, \qquad \text{for all } \tau = \frac{1}{\rho} > 0. \tag{2}
$$

The pressure p and the sound velocity c are respectively defined by

$$
p \stackrel{\mathrm{def}}{=} p^{\mathrm{EOS}}(\tau) = -(\mathrm{d}e^{\mathrm{EOS}}/\mathrm{d}\tau)(\tau), \qquad c = c^{\mathrm{EOS}}(\tau) \stackrel{\mathrm{def}}{=} \tau\sqrt{-(\mathrm{d}p^{\mathrm{EOS}}/\mathrm{d}\tau)(\tau)} > 0. \tag{3}
$$

At the initial instant $t = 0$, we assume that

$$
\rho(\mathbf{x}, t=0) = \rho_0(\mathbf{x}), \qquad \mathbf{u}(\mathbf{x}, t=0) = \mathbf{u}_0(\mathbf{x}), \qquad p(\mathbf{x}, t=0) = p^{\mathrm{EOS}}(1/\rho_0(\mathbf{x})), \tag{4}
$$

where ρ_0 and $\mathbf{u}_0$ are given functions.

The system (1) is strictly hyperbolic and for one-dimensional problems the associated eigenvalues are $u - c$ and $u + c$ [73, 91, 41].

In this section, we present the development of a two-step splitting approach following the work of [15, 17, 19, 79], where the barotropic Euler equations are rewritten to decouple the acoustic and transport terms. Using the chain's rule on the space derivative, for a regular solution, we rewrite system (1) as follows

$$
\begin{aligned}
\partial_t \rho \;&+\; \underbrace{\mathbf{u} \cdot \boldsymbol{\nabla} \rho}_{\text{transport}} \;+\; \underbrace{\rho \boldsymbol{\nabla} \cdot \mathbf{u}}_{\text{acoustic}} = 0, && \text{(5a)}\\
\partial_t (\rho \mathbf{u}) \;&+\; \underbrace{(\mathbf{u} \cdot \boldsymbol{\nabla})(\rho \mathbf{u})}_{\text{transport}} \;+\; \underbrace{(\rho \mathbf{u})\, \boldsymbol{\nabla} \cdot \mathbf{u} + \boldsymbol{\nabla} p}_{\text{acoustic}} = \mathbf{0}. && \text{(5b)}
\end{aligned}
$$

Thus, we split the main system into two subsystems. We refer to the first subsystem as the **barotropic acoustic subsystem**:

$$
\begin{cases}
\partial_t \rho + \rho \boldsymbol{\nabla} \cdot \mathbf{u} = 0, & \text{(6a)}\\
\partial_t (\rho \mathbf{u}) + (\rho \mathbf{u})\, \boldsymbol{\nabla} \cdot \mathbf{u} + \boldsymbol{\nabla} p = \mathbf{0}. & \text{(6b)}
\end{cases}
$$

The second will be called the **barotropic transport subsystem**:

$$\begin{cases} \partial_t \rho + \mathbf{u} \cdot \boldsymbol{\nabla} \rho = 0, & \text{(7a)} \\ \partial_t (\rho \mathbf{u}) + (\mathbf{u} \cdot \boldsymbol{\nabla}) (\rho \mathbf{u}) = \mathbf{0}. & \text{(7b)} \end{cases}$$

Each subsystem will be solved successively in a two-step strategy as detailed in section 3.2. Thanks to this separate treatment, we will be able to implement an implicit update of the acoustic phenomena and an explicit update of the transport phenomena following [25, 15, 19] so that the overall numerical scheme belongs to the category of Implicit-Explicit (IMEX) schemes. This strategy aims to overcome the stability constraints associated with fast wave propagation.

In order to approximate (6), we first remark that it can be recast as follows

$$\begin{cases} \rho \partial_t \tau - \boldsymbol{\nabla} \cdot \mathbf{u} = 0, & \text{(8a)} \\ \rho \partial_t \mathbf{u} + \boldsymbol{\nabla} p = \mathbf{0}. & \text{(8b)} \end{cases}$$

The acoustic subsystem (8a) exhibits a wave structure analogous to the one-dimensional barotropic Lagrangian gas dynamics or p-system [41], featuring two symmetrical nonlinear acoustic waves of characteristic velocities $\pm c$. However, let us once again underline that unlike classical Lagrangian discretizations [94, 23, 32, 28, 41], our approach does not solve the equations in Lagrangian coordinates tied to the fluid motion. Then, we propose to approximate (8a) within the time interval $t \in [t^n, t^{n+1})$ by using Suliciu-type relaxation approximation [87, 17, 65, 19, 18, 50] to disregard the nonlinearities of the pressure $p = p^{\mathrm{EOS}}(\tau)$ in the acoustic sub-system. Thus, for $t \in [t^n, t^{n+1})$, we will consider the following subsystem,

$$\begin{cases} \rho \partial_t \tau - \boldsymbol{\nabla} \cdot \mathbf{u} = 0, & \text{(9a)} \\ \rho \partial_t \mathbf{u} + \boldsymbol{\nabla} \pi = \mathbf{0}, & \text{(9b)} \\ \rho \partial_t \pi + a^2 \boldsymbol{\nabla} \cdot \mathbf{u} = 0, & \text{(9c)} \end{cases}$$

where $a > 0$, a constant parameter, and the extra variable π serve respectively as a surrogate acoustic impedance and a surrogate pressure. For the sake of numerical stability, a must satisfy the so-called Whitham sub-characteristic condition:

$$a > \max(\rho c), \tag{10}$$

where ρc spans the values of the solutions of (1) for $t \in [t^n, t^{n+1})$ (see [7, 6, 14, 16, 24] and lemma C.1 in appendix C.1). Moreover, the consistency of π with the pressure p that verifies the EOS is ensured by re-initializing π at each time step t^n so that $\pi^n = p^{\mathrm{EOS}}(1/\rho^n)$.

3 Discretization strategy

3.1 Staggered discretization

Let $d \in \{1, 2, 3\}$ denote the dimension of the physical space and let $\left(\mathbf{e}^{(i)}\right)_{i=1,\dots,d}$ represent the canonical basis. We adopt the discretization framework proposed in [61]. The computational domain Ω is regular following the criteria of the finite element in the literature [21]. The mesh $\mathcal{M}$

comprises a collection of cells K such that $\Omega = \cup_{K\in\mathcal{M}} K$. We will consider two types of meshes, depending of the shape of Ω.

- If Ω has a general shape, each cell $K \in \mathcal{M}$ will be either a non-degenerate quadrilateral for $d = 2$ (resp. hexahedron for $d = 3$) or a simplex. When $d = 2$, both types of cells may possibly be combined within the same mesh.
- If Ω is a rectangle for $d = 2$ (resp. a rectangular parallelepiped for $d = 3$) whose boundaries are perpendicular to a coordinate axis, each $K \in \mathcal{M}$ will be a rectangle for $d = 2$ (resp. a rectangular parallelepipeds for $d = 3$).

For any $K \in \mathcal{M}$, we note $\mathcal{E}(K)$ the set of all faces of K and $\mathcal{E} = \cup_{K\in\mathcal{M}} \mathcal{E}(K)$ the set of all faces of the mesh. We note $\mathcal{E}_{ext} = \{\sigma \in \mathcal{E} \mid \sigma \subset \partial\Omega\}$ the set of external faces and $\mathcal{E}_{int} = \mathcal{E} \setminus \mathcal{E}_{ext}$ the set of internal faces of the mesh. Consider a face $\sigma \in \mathcal{E}_{int}$ that separates two adjacent cells K and L, this face will be referred to as $\sigma = K|L$. Moreover, we define $\mathbf{n}_{K,\sigma}$ the outward unit normal vector to σ of cell K, $|K|$ the measure of the cell K and $|\sigma|$ the measure of the face σ.

In the special case where Ω is a rectangle for $d = 2$ (resp. a rectangular parallelepiped for $d = 3$) whose boundaries are perpendicular to a coordinate axis, $\mathcal{E}^{(i)}$ (resp. $\mathcal{E}^{(i)}_{ext}$) will denote the subset of faces of $\mathcal{E}$ (resp. $\mathcal{E}_{ext}$) which are orthogonal to $\mathbf{e}^{(i)}$, $1 \le i \le d$.

In our staggered discretization approach, one of the following strategies will be employed depending on the shape of the domain: either a Marker-and-Cell (**MAC**) strategy [53, 51] when the computational domain is a rectangle for $d = 2$ (resp. a rectangular parallelepiped for $d = 3$), or the non-conforming low-order finite element approximations, referred to as the Rannacher-Turek element (**RT**) [80] for quadrilateral or hexahedric meshes, or the lowest degree Crouzeix-Raviart element (**CR**) [27] for simplicial meshes.

For both the MAC and the RT/CR approaches, the scalar quantities are discretized at the center of each cell of $\mathcal{M}$. In the context of the barotropic model (1) this boils down to associate the pressure and the density to the centers of the cells of the mesh $\mathcal{M}$, so that we consider discrete values p_K, ρ_K, for all cell $K \in \mathcal{M}$.

Velocity degrees of freedom are associated with the mesh faces. In the MAC approach, only the normal component of the velocity is retained at each face, whereas the RT/CR discretization use the full velocity vector. In order to cast our numerical scheme within a unified framework, we define a discrete vector variable $\mathbf{u}_\sigma$ that encapsulates the relevant degrees of freedom associated with each mesh face $\sigma \in \mathcal{E}$, namely:

$$\mathbf{u}_\sigma = \begin{cases} u_{\sigma,i}\mathbf{e}^{(i)}, & \text{for the MAC discretization, } \sigma \in \mathcal{E}^{(i)},\ i = 1, 2, 3, \\ (u_{\sigma,1}, \cdots, u_{\sigma,d})^T, & \text{for the RT/CR discretization.} \end{cases} \tag{11}$$

To guide the design of a finite volume method with degrees of freedom located at the faces, we introduce a dual mesh, so that the discrete velocity $\mathbf{u}_\sigma$, is associated with a specific dual cell D_σ. For any internal face $\sigma \in \mathcal{E}_{int}$, where σ separates the neighboring cells K and L, i.e., $\sigma = K|L$, we define the dual cell D_σ by setting

$$D_\sigma = D_{K,\sigma} \cup D_{L,\sigma},$$

where $D_{K,\sigma}$ and $D_{L,\sigma}$ are the so-called half-dual cells associated respectively with cell K and L. Their definitions depend on the type of discretization.

- RT/CR discretization: $D_{K,\sigma}$ is defined as the cone with basis σ and having the mass center of K as the vertex. We thus obtain a partition of K in $\operatorname{card}(\mathcal{E}(K))$ sub-cells (see figure 2). One can then assume, without adding constraining hypotheses, that each subdomain has the same measure $|D_{K,\sigma}| = |K|/\operatorname{card}(\mathcal{E}(K))$,
- MAC discretization: if $\mathbf{x}_K \in \mathbb{R}^d$ is the center of the cell K, we set $D_{K,\sigma} = \{\mathbf{x} \in K \mid 0 \leq (\mathbf{x} - \mathbf{x}_K) \cdot \mathbf{n}_{K,\sigma}\}$ (see figure 1). In other words, $D_{K,\sigma}$ is the rectangle or rectangular parallelepiped of basis σ and of measure $|D_{K,\sigma}| = |K|/2$.

Let $\mathcal{E}(D_\sigma)$ represent the set of faces of the dual cell D_σ, and let $|D_\sigma|$ denote its measure. The common face shared by two neighbouring dual cells D_σ and $D_{\sigma'}$ is noted $\varepsilon = D_\sigma|D_{\sigma'}$. Moreover, in the sequel we will also use the following set of faces $\mathcal{E}\left(D_{K,\sigma}\right)$ and

$$\widetilde{\mathcal{E}}\left(D_{K,\sigma}\right) = \left\{\varepsilon \in \mathcal{E}(D_\sigma) \mid \varepsilon \cap \overline{K} \neq \emptyset\right\}. \tag{12}$$

Let us emphasize that we have $\mathcal{E}(D_\sigma) = \widetilde{\mathcal{E}}\left(D_{K,\sigma}\right) \cup \widetilde{\mathcal{E}}\left(D_{L,\sigma}\right)$. For an external face $\sigma \in \mathcal{E}_{ext} \cap \mathcal{E}(K)$, the associated dual cell is the internal half-dual cell that is $D_\sigma = D_{K,\sigma}$. To simulate impermeability of the boundaries, a no-slip boundary condition $\mathbf{u} \cdot \mathbf{n} = 0$ by imposing

$$\mathbf{u}_\sigma \cdot \mathbf{n}_{K,\sigma} = 0, \quad \text{for all } \sigma \in \mathcal{E}_{ext} \cap \mathcal{E}(K). \tag{13}$$

Let us remark that for the RT/CR discretization, (13) does not constrain the discrete tangential velocity while for the MAC discretization one relation sets all the discrete velocities to zero on the boundary.

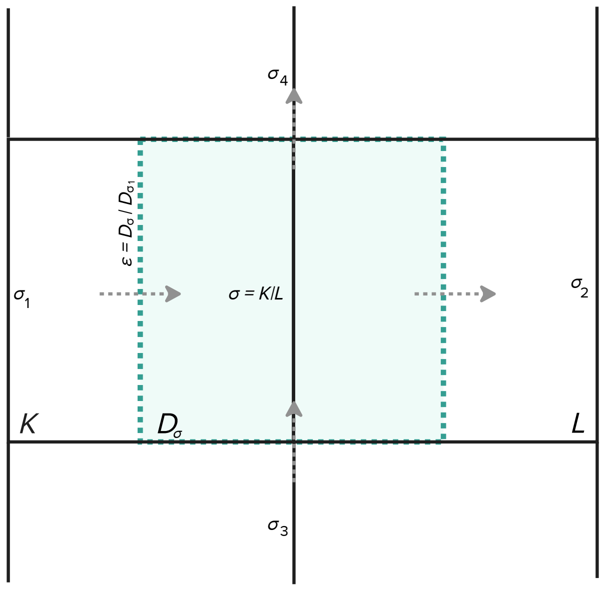

Figure 1: MAC discretization. Primal elements K, L associated face σ and dual cell D_σ with neighboring faces.

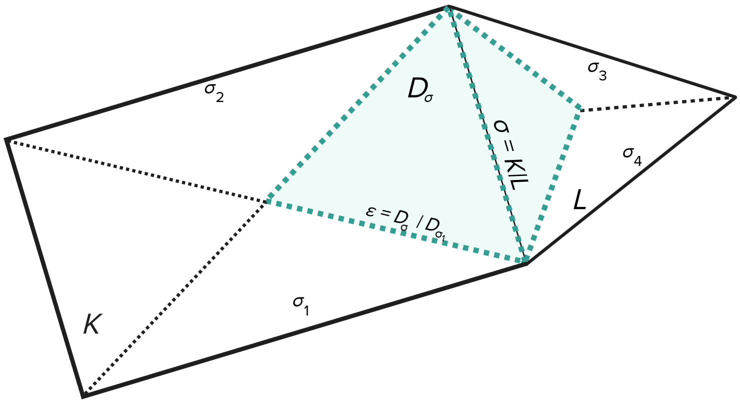

Figure 2: RT/CR discretization. Primal elements K, L associated face σ and dual cell D_σ with neighboring faces.

We conclude this section on notation by further motivating our choice. Some authors adopt the so-called (i, j, k) notation, which is well suited for structured Cartesian meshes and was also used in our previous work [50]. However, when considering more general meshes, such as triangular meshes in 2D or tetrahedral meshes in 3D, a more flexible notation becomes necessary.

Since several of the ideas developed in this work rely on the staggered framework [13, 56, 59, 61], we chose to adopt the same notation. The correspondence between this general notation and the (i, j, k) formalism is summarized in Table 1.

Variables	Unstructured index	(i, j, k)-index
Scalar b, $b \in \{\rho, e, p\}$	$b_K, \ K \in \mathcal{M}$	$b_{i,j,k}$
Vector $\mathbf{u}$	$\mathbf{u}_\sigma, \ \sigma \in \mathcal{E}(K)$	$\mathbf{u}_{i+l/2,j,k}, \mathbf{u}_{i,j+l/2,k}, \mathbf{u}_{i,j,k+l/2}, \ l = -1, +1$

Table 1: Mapping between our unstructured meshes index notation and the standard (i, j, k) Cartesian grid indices.

From an implementation standpoint, this choice allows for a unified code implementation for both MAC and RT/CR discretizations. In both cases, the velocity field is stored as a two-dimensional array of shape card$(\mathcal{E}_{int} \cup \mathcal{E}_{ext}) \times d$.

For the MAC discretization, only the normal component at each internal face $\sigma \in \mathcal{E}_{int}$ is initialized to a non-zero value at time $t = 0$, whereas for the RT/CR discretization the full velocity vector is initialized. For $t > 0$, the contributions of the momentum convection operator, as well as those of the pressure gradient, are limited to the normal direction of the face in the MAC scheme, so that only the normal component of the velocity vector evolves in time. In contrast, for the RT/CR discretization, the momentum convection operator contributes to all components of the velocity vector, while the pressure gradient contributions remain identical to those of the MAC scheme.

In conclusion, both discretizations are handled within a single code implementation, the only difference lying in the function used to compute the momentum convection operator.

3.2 Time update algorithm

We consider a strictly increasing sequence of instants $(t^n)_{n\in\mathbb{N}}$ and note the time step $\delta t = t^{n+1} - t^n$. Our numerical scheme aims at computing the cell-centered values $(\rho_K^n)_{K\in\mathcal{M}}$ and face-centered velocities $(\mathbf{u}_\sigma^n)_{\sigma\in\mathcal{E}_{int}}$ for each instant $n \geq 0$. Given the values $(\rho_K^n)_{K\in\mathcal{M}}$, $(\mathbf{u}_\sigma^n)_{\sigma\in\mathcal{E}_{int}}$ at time t^n, we employ a two-step algorithm to advance the solution to t^{n+1}: the first step, referred to as the acoustic step, involves computing intermediate variables $(\widetilde{\rho}_K)_{K\in\mathcal{M}}$, $(\widetilde{\mathbf{u}}_\sigma)_{\sigma\in\mathcal{E}_{int}}$ by solving the acoustic subsystem (6). The second step called the transport step will update $(\widetilde{\rho}_K)_{K\in\mathcal{M}}$, $(\widetilde{\mathbf{u}}_\sigma)_{\sigma\in\mathcal{E}_{int}}$ by means of an approximation of the subsystem (29) to compute the updated solution $(\rho_K^{n+1})_{K\in\mathcal{M}}$, $(\mathbf{u}_\sigma^{n+1})_{\sigma\in\mathcal{E}_{int}}$. This two-step sequence can be summarized as follows:

$$\begin{bmatrix} (\rho_K^n)_{K\in\mathcal{M}} \\ (\mathbf{u}_\sigma^n)_{\sigma\in\mathcal{E}_{int}} \end{bmatrix} \xrightarrow[\text{approximation of (6)}]{\text{acoustic step}} \begin{bmatrix} (\widetilde{\rho}_K)_{K\in\mathcal{M}} \\ (\widetilde{\mathbf{u}}_\sigma)_{\sigma\in\mathcal{E}_{int}} \end{bmatrix} \xrightarrow[\text{approximation of (29)}]{\text{transport step}} \begin{bmatrix} (\rho_K^{n+1})_{K\in\mathcal{M}} \\ (\mathbf{u}_\sigma^{n+1})_{\sigma\in\mathcal{E}_{int}} \end{bmatrix}. \tag{14}$$

The initial conditions for cell-centered (resp. face-centered) discrete unknowns are defined as the average of the initial conditions over the primal (resp. dual) cells

$$\forall K \in \mathcal{M}, \quad \rho_K^0 = \frac{1}{|K|}\int_K \rho_0(\mathbf{x})\,\mathrm{d}\mathbf{x}, \qquad \forall \sigma \in \mathcal{E}_{int}, \quad \mathbf{u}_\sigma^0 = \frac{1}{|D_\sigma|}\int_{D_\sigma} \mathbf{u}_0(\mathbf{x})\,\mathrm{d}\mathbf{x}. \tag{15}$$

4 A staggered Lagrange-projection like (SLP) scheme for the barotropic system

In this section, we present the staggered Lagrange-projection like scheme, hereafter referred to as SLP for convenience. The scheme consists in discretizing and solving first the acoustic subsystem (6), followed by the transport subsystem (29), and then combining the results to obtain the overall scheme. We begin by introducing the following definitions:

$$u_{K,\sigma} = \mathbf{u}_\sigma \cdot \mathbf{n}_{K,\sigma}, \tag{16a}$$
$$a_K = \rho_K c^{\mathrm{EOS}}(1/\rho_K), \tag{16b}$$

and

$$\varphi_{D_\sigma} = \frac{|D_{K,\sigma}|\,\varphi_K + |D_{L,\sigma}|\,\varphi_L}{|D_\sigma|}, \quad \text{for } \varphi \in \{\rho, a\}. \tag{17}$$

We will also use the positive and negative parts of any real number, namely

$$x = x^+ - x^-, \qquad x^+ = \max(x,0) \geq 0, \qquad x^- = -\min(x,0) \geq 0, \qquad x \in \mathbb{R}. \tag{18}$$

4.1 The acoustic step

For solving the acoustic subsystem (9), we use the following discretization:

$$\forall K \in \mathcal{M}, \qquad \frac{|K|}{\delta t} \rho_K^n \left(\widetilde{\tau}_K - \tau_K^n \right) - |K| \left(\boldsymbol{\nabla} \cdot \widetilde{\mathbf{u}} \right)_K = 0, \tag{19a}$$

$$\forall \sigma \in \mathcal{E}_{int}, \qquad \frac{|D_\sigma|}{\delta t} \rho_{D_\sigma}^n \left(\widetilde{\mathbf{u}}_\sigma - \mathbf{u}_\sigma^n \right) + |D_\sigma| \left(\boldsymbol{\nabla} \widetilde{\pi} \right)_{D_\sigma} = \mathbf{0}, \tag{19b}$$

$$\forall K \in \mathcal{M}, \qquad \frac{|K|}{\delta t} \rho_K^n \left(\widetilde{\pi}_K - \pi_K^n \right) + \left(a_K^n \right)^2 |K| \left(\boldsymbol{\nabla} \cdot \widetilde{\mathbf{u}} \right)_K = 0, \tag{19c}$$

where

$$\left(\boldsymbol{\nabla} \cdot \widetilde{\mathbf{u}} \right)_K = \frac{1}{|K|} \sum_{\sigma \in \mathcal{E}(K)} |\sigma| \widetilde{u}_{K,\sigma}^*, \tag{20a}$$

$$\widetilde{u}_{K,\sigma}^* = \widetilde{u}_{K,\sigma} - \frac{1}{2 a_{D_\sigma}^n} \left(\widetilde{\pi}_L - \widetilde{\pi}_K \right), \tag{20b}$$

$$\left(\boldsymbol{\nabla} \widetilde{\pi} \right)_{D_\sigma} = \frac{1}{|D_\sigma|} \left(\widetilde{\pi}_L - \widetilde{\pi}_K \right) |\sigma| \mathbf{n}_{K,\sigma}. \tag{20c}$$

Let us underline that although the surrogate pressure is initialized at the beginning of the time step thanks to the EOS so that $\pi_K^n = p^{\mathrm{EOS}}(1/\rho_K^n)$, the pressure evaluated at the end of the acoustic step is no longer related to the EOS as a priori $\widetilde{\pi}_K \neq p^{\mathrm{EOS}}(1/\widetilde{\rho}_K)$.

Next, we examine the evolution of the discrete kinetic energy across the acoustic step (19). We have the following lemma.

Lemma 4.1 (Discrete kinetic energy balance for the acoustic step)**.** *A solution to the acoustic subsystem* (19) *satisfies the following equality, for $\sigma \in \mathcal{E}_{int}$,*

$$\frac{|D_\sigma|}{\delta t} \rho_{D_\sigma}^n \left(\frac{|\widetilde{\mathbf{u}}_\sigma|^2}{2} - \frac{|\mathbf{u}_\sigma^n|^2}{2} \right) + \widetilde{u}_{K,\sigma}^* |D_\sigma| \left(\boldsymbol{\nabla} \widetilde{\pi} \right)_{D_\sigma} \cdot \mathbf{n}_{K,\sigma} = -\widetilde{R}_\sigma, \tag{21}$$

with

$$\widetilde{R}_\sigma = \frac{|D_\sigma|}{\delta t} \frac{\rho_{D_\sigma}^n}{2} |\widetilde{\mathbf{u}}_\sigma - \mathbf{u}_\sigma^n|^2 + \frac{|\sigma|}{2 a_{D_\sigma}^n} \left(\widetilde{\pi}_L - \widetilde{\pi}_K \right)^2, \tag{22}$$

which is non-negative for any $\delta t > 0$.

Proof. By taking the scalar product of (19b) with the vector $\widetilde{\mathbf{u}}_\sigma$, then using the identity $|\mathbf{u}|^2 - \mathbf{u} \cdot \mathbf{v} = \frac{1}{2}|\mathbf{u}|^2 - \frac{1}{2}|\mathbf{v}|^2 + \frac{1}{2} \left| \mathbf{u} - \mathbf{v} \right|^2$ and definition (20b), one obtains the expected result. $\square$

Before going any further, we remark that (21) yields a discretization of the equation

$$\rho \partial_t \left(\frac{|\mathbf{u}|^2}{2} \right) + \mathbf{u} \cdot \boldsymbol{\nabla} \pi = 0, \tag{23}$$

which is a consequence of (9b) and that the density update (19a) across the acoustic step also reads

$$\widetilde{\rho}_K = \frac{\rho_K^n}{1 + \delta t \left(\boldsymbol{\nabla} \cdot \widetilde{\mathbf{u}} \right)_K}, \qquad \forall K \in \mathcal{M}. \tag{24}$$

Finally, it is important to note that equations (19b)-(19c) define a linear system with respect to the variables $(\widetilde{u}_\sigma)_{\sigma\in\mathcal{E}_{int}}$, $(\widetilde{\pi}_K)_{K\in\mathcal{M}}$ which can be reduced to a system involving only the relaxation pressure $\widetilde{\pi}_K, K \in \mathcal{M}$. This reduction technique, along with its numerical resolution, is detailed in appendix B. The overall method exhibits similarities to standard projection methods, which require the resolution of a scalar equation for the pressure update [20, 88, 22, 46].

To ensure that our numerical scheme is well-defined, we first verify that the linear system arising in the acoustic step is well-posed. This result relies on the following integral energy inequality associated with the acoustic step.

Proposition 4.2 (Integral form of the relaxation total energy conservation law in the acoustic step)**.** *For the barotropic (resp. full Euler system) the pressure $\widetilde{\pi}_K$ obtained by the acoustic step* (19c) *(resp.* (57d)*) verifies*

$$|K|\frac{\rho_K^n}{\delta t}\left(\frac{(\widetilde{\pi}_K)^2}{2(a_K^n)^2}-\frac{(\pi_K^n)^2}{2(a_K^n)^2}\right)+|K|\widetilde{\pi}_K\left(\boldsymbol{\nabla}\cdot\widetilde{\mathbf{u}}\right)_K=-|K|\frac{\rho_K^n}{\delta t}\frac{(\widetilde{\pi}_K-\pi_K^n)^2}{2(a_K^n)^2}. \tag{25}$$

Consequently we also have

$$\sum_{K\in\mathcal{M}}|K|\frac{\rho_K^n}{\delta t}\left[\frac{(\widetilde{\pi}_K)^2}{2(a_K^n)^2}-\frac{(\pi_K^n)^2}{2(a_K^n)^2}\right]+\sum_{\sigma\in\mathcal{E}_{int}}\frac{|D_\sigma|}{\delta t}\rho_{D_\sigma}^n\left[\frac{|\widetilde{\mathbf{u}}_\sigma|^2}{2}-\frac{|\mathbf{u}_\sigma^n|^2}{2}\right]$$
$$=-\sum_{K\in\mathcal{M}}|K|\frac{\rho_K^n}{\delta t}\frac{(\widetilde{\pi}_K-\pi_K^n)^2}{2(a_K^n)^2}-\sum_{\sigma\in\mathcal{E}_{int}}\widetilde{R}_\sigma. \tag{26}$$

Proof. The proof of this proposition is given in appendix C.1. □

We then have the following proposition concerning the well-posedness of the linear system (19b)-(19c).

Proposition 4.3 (Well-posedness of the linear system in the acoustic step)**.** *For any $\delta t > 0$, the solution $(\widetilde{u}_\sigma)_{\sigma\in\mathcal{E}_{int}}$, $(\widetilde{\pi}_K)_{K\in\mathcal{M}}$ of the linear system with respect to the pressure and velocity formed by equations* (19b)-(19c) *for the barotropic system* (1) *or formed by equations* (57b)-(57d) *for the Euler system* (46) *exists and is unique.*

Proof. The proof of this proposition is given in appendix C.1. □

4.2 The transport step

For the discretization of the transport subsystem (29), we consider the following discrete subsystem:

$$\forall K\in\mathcal{M},\qquad \frac{|K|}{\delta t}\left(\rho_K^{n+1}-\widetilde{\rho}_K\right)+\sum_{\sigma\in\mathcal{E}(K)}\widetilde{F}_{K,\sigma}-\widetilde{\rho}_K|K|\left(\boldsymbol{\nabla}\cdot\widetilde{\mathbf{u}}\right)_K=0, \tag{27a}$$

$$\forall\sigma\in\mathcal{E}_{int},\quad \frac{|D_\sigma|}{\delta t}\left(\rho_{D_\sigma}^{n+1}\mathbf{u}_\sigma^{n+1}-\widetilde{\rho}_{D_\sigma}\widetilde{\mathbf{u}}_\sigma\right)+\sum_{\varepsilon\in\mathcal{E}(D_\sigma)}\widetilde{F}_{\sigma,\varepsilon}\widetilde{\mathbf{u}}_\varepsilon-\widetilde{\rho}_{D_\sigma}\widetilde{\mathbf{u}}_\sigma|D_\sigma|\left(\boldsymbol{\nabla}\cdot\widetilde{\mathbf{u}}\right)_{D_\sigma}=\mathbf{0}, \tag{27b}$$

with

$$\widetilde{F}_{K,\sigma} = |\sigma| \widetilde{\rho}_\sigma \widetilde{u}^*_{K,\sigma}, \tag{28a}$$

$$\widetilde{\rho}_\sigma = \begin{cases} \widetilde{\rho}_K, & \text{if } \widetilde{u}^*_{K,\sigma} > 0, \\ \widetilde{\rho}_L, & \text{otherwise,} \end{cases} \tag{28b}$$

$$\widetilde{\rho}_{D_\sigma} = \frac{\left|D_{K,\sigma}\right| \widetilde{\rho}_K + \left|D_{L,\sigma}\right| \widetilde{\rho}_L}{|D_\sigma|}, \tag{28c}$$

where $(\boldsymbol{\nabla} \cdot \widetilde{\mathbf{u}})_{D_\sigma}$, $\widetilde{F}_{\sigma,\varepsilon}$ and $\widetilde{\mathbf{u}}_\varepsilon$ are yet to be specified.

Let us note that the discretization (27) is consistent with the transport system (7) as for smooth fields (7) can be expressed as

$$\begin{cases} \partial_t \rho + \boldsymbol{\nabla} \cdot (\rho \mathbf{u}) - \rho \boldsymbol{\nabla} \cdot \mathbf{u} = 0, & (29a) \\ \partial_t (\rho \mathbf{u}) + \boldsymbol{\nabla} \cdot (\rho \mathbf{u} \otimes \mathbf{u}) - \rho \mathbf{u} \boldsymbol{\nabla} \cdot \mathbf{u} = \mathbf{0}. & (29b) \end{cases}$$

The dual mass fluxes $\widetilde{F}_{\sigma,\varepsilon}$ and upwind velocities $\widetilde{\mathbf{u}}_\varepsilon$ at the dual faces of the dual cells are defined as in [61] for the MAC discretization and in [13] for the RT/CR discretization. In appendix A, we describe more precisely how $\widetilde{F}_{\sigma,\varepsilon}$ is obtained. As for the velocity vector $\widetilde{\mathbf{u}}_\varepsilon$ at the dual faces, it is defined by the following upwind scheme:

$$\forall \varepsilon = \sigma|\sigma' \in \widetilde{\mathcal{E}}(D_\sigma), \qquad \widetilde{\mathbf{u}}_\varepsilon = \begin{cases} \widetilde{\mathbf{u}}_\sigma, & \text{if } \widetilde{F}_{\sigma,\varepsilon} > 0, \\ \widetilde{\mathbf{u}}_{\sigma'}, & \text{otherwise.} \end{cases} \tag{30}$$

Let us now turn to the choice of $(\boldsymbol{\nabla} \cdot \widetilde{\mathbf{u}})_{D_\sigma}$. Accounting for (29b) and (29a) we have

$$\partial_t \left(\rho \frac{|\mathbf{u}|^2}{2} \right) + \boldsymbol{\nabla} \cdot \left(\rho \frac{|\mathbf{u}|^2}{2} \mathbf{u} \right) - \rho \frac{|\mathbf{u}|^2}{2} \boldsymbol{\nabla} \cdot \mathbf{u} = 0. \tag{31}$$

In order to provide a definition for $(\boldsymbol{\nabla} \cdot \widetilde{\mathbf{u}})_{D_\sigma}$, we now use an argument that relates to the evolution of the kinetic energy across the transport step (29). We have the following lemma.

Lemma 4.4 (Discrete kinetic energy balance for the transport step)**.** *Let $(\boldsymbol{\nabla} \cdot \widetilde{\mathbf{u}})_{D_\sigma}$ be defined by the following relation:*

$$\widetilde{\rho}_{D_\sigma} |D_\sigma| \, (\boldsymbol{\nabla} \cdot \widetilde{\mathbf{u}})_{D_\sigma} = \left|D_{K,\sigma}\right| \widetilde{\rho}_K \, (\boldsymbol{\nabla} \cdot \widetilde{\mathbf{u}})_K + \left|D_{L,\sigma}\right| \widetilde{\rho}_L \, (\boldsymbol{\nabla} \cdot \widetilde{\mathbf{u}})_L \,, \tag{32}$$

with $\widetilde{\rho}_{D_\sigma}$ given by (28c). Then a solution to the discrete transport subsystem (27) satisfies the following equality, for all $\sigma \in \mathcal{E}_{int}$,

$$\frac{|D_\sigma|}{\delta t} \left(\rho^{n+1}_{D_\sigma} \frac{\left|\mathbf{u}^{n+1}_\sigma\right|^2}{2} - \widetilde{\rho}_{D_\sigma} \frac{|\widetilde{\mathbf{u}}_\sigma|^2}{2} \right) + \sum_{\varepsilon \in \mathcal{E}(D_\sigma)} \widetilde{F}_{\sigma,\varepsilon} \frac{|\widetilde{\mathbf{u}}_\varepsilon|^2}{2} - \widetilde{\rho}_{D_\sigma} \frac{|\widetilde{\mathbf{u}}_\sigma|^2}{2} |D_\sigma| \, (\boldsymbol{\nabla} \cdot \widetilde{\mathbf{u}})_{D_\sigma} = -R^{n+1}_\sigma, \tag{33}$$

with

$$R^{n+1}_\sigma = \frac{|D_\sigma|}{\delta t} \frac{\rho^n_{D_\sigma}}{2} \left|\mathbf{u}^{n+1}_\sigma - \widetilde{\mathbf{u}}_\sigma\right|^2 - \sum_{\varepsilon \in \mathcal{E}(D_\sigma)} \frac{\widetilde{F}_{\sigma,\varepsilon}}{2} \left|\mathbf{u}^{n+1}_\sigma - \widetilde{\mathbf{u}}_\varepsilon\right|^2. \tag{34}$$

Proof. The proof of this lemma is given in appendix C.1. □

The non-negativity of R_σ^{n+1} is guaranteed by the CFL condition given hereater by relation (38a). The presence of this source term indicates that the discrete transport operator ensures the decay of kinetic energy within the scheme. At the continuous level, a similar effect could be achieved by introducing viscous dissipation. Therefore, the non-negativity of R_σ^{n+1} can be seen as the manifestation of a numerical dissipation effect that confers a nonlinear stability property to the scheme.

4.3 Overall scheme and properties

In the following, we present properties of our numerical scheme defined by (19) and (27). Many of these are also valid for the numerical scheme detailed in section 5 for the full Euler system of equations. Therefore, references to the discretization of section 5 will also be mentioned hereafter.

Accouting for the acoustic step (19) and the transport step (27) allows to express the update from t^n to t^{n+1}: using (24) and (28c) we obtain the conservative update relation that will be referred to as the **S**taggered **L**agrange-**P**rojection like **IM**plicit-**EX**plicit (**SLP IMEX**) scheme:

$$\forall K \in \mathcal{M}, \qquad \frac{|K|}{\delta t}\left(\rho_K^{n+1} - \rho_K^n\right) + \sum_{\sigma \in \mathcal{E}(K)} \widetilde{F}_{K,\sigma} = 0, \tag{35a}$$

$$\forall \sigma \in \mathcal{E}_{int}, \qquad \frac{|D_\sigma|}{\delta t}\left(\rho_{D_\sigma}^{n+1}\mathbf{u}_\sigma^{n+1} - \rho_{D_\sigma}^n \mathbf{u}_\sigma^n\right) + \sum_{\varepsilon \in \mathcal{E}(D_\sigma)} \widetilde{F}_{\sigma,\varepsilon}\widetilde{\mathbf{u}}_\varepsilon + |D_\sigma| \left(\boldsymbol{\nabla}\widetilde{\pi}\right)_\sigma = \mathbf{0}. \tag{35b}$$

Before going any further, let us introduce the following notation: if b_K, $K \in \mathcal{M}$ is a variable associated with the primal mesh, we set

$$\mathrm{Cvx}(b)_K = \left\{1 - \delta t \sum_{\sigma \in \mathcal{E}(K)} \frac{|\sigma|}{|K|}(\widetilde{u}^*_{K,\sigma})^- \right\} b_K + \delta t \sum_{\substack{\sigma \in \mathcal{E}(K) \\ \sigma = K|L}} \frac{|\sigma|}{|K|}(\widetilde{u}^*_{K,\sigma})^- b_L. \tag{36}$$

The operator Cvx will help to exhibit stability properties of the scheme. Indeed, one can see that under a suitable CFL condition given in (38b), $\mathrm{Cvx}(b)_K$ is a convex combination of b_K and its neighboring values b_L, $\sigma = K|L \in \mathcal{E}(K)$.

Let us now focus on the update of the density across the transport step (27a). Let $\sigma = K|L \in \mathcal{E}(K)$, the mass flux defined by (28a) can be expressed as

$$\widetilde{F}_{K,\sigma} = |\sigma|\widetilde{\rho}_K(\widetilde{u}^*_{K,\sigma})^+ - |\sigma|\widetilde{\rho}_L(\widetilde{u}^*_{K,\sigma})^-.$$

By injecting this expression into (27a) and using (20a), we get

$$\begin{aligned}
\rho_K^{n+1} &= \widetilde{\rho}_K - \delta t \sum_{\substack{\sigma \in \mathcal{E}(K) \\ \sigma = K|L}} \frac{|\sigma|}{|K|}\left\{\widetilde{\rho}_K(\widetilde{u}^*_{K,\sigma})^+ - \widetilde{\rho}_L(\widetilde{u}^*_{K,\sigma})^- - \widetilde{\rho}_K\widetilde{u}^*_{K,\sigma}\right\} \\
&= \widetilde{\rho}_K \left\{ 1 - \delta t \sum_{\sigma \in \mathcal{E}(K)} \frac{|\sigma|}{|K|}\left((\widetilde{u}^*_{K,\sigma})^+ - \widetilde{u}^*_{K,\sigma}\right) \right\} + \delta t \sum_{\substack{\sigma \in \mathcal{E}(K) \\ \sigma = K|L}} \frac{|\sigma|}{|K|}\widetilde{\rho}_L(\widetilde{u}^*_{K,\sigma})^-,
\end{aligned}$$

hence the transport step for the density reads

$$\rho_K^{n+1} = \mathrm{Cvx}(\widetilde{\rho})_K. \tag{37}$$

Relation (37) under suitable CFL conditions ensures that the transport step (27a) for the density is obtained thanks to a convex combination.

We now sum up useful CFL conditions that can be applied to the scheme (35).

$$\delta t \leq \frac{|D_\sigma|\rho^n_{D_\sigma}}{\sum\limits_{\varepsilon\in\mathcal{E}(D_\sigma)} \widetilde{F}^+_{\sigma,\varepsilon}}, \quad \forall \sigma \in \mathcal{E}_{int} \qquad \text{ensures that } R^{n+1}_\sigma \geq 0 \text{ as defined in (34)}, \tag{38a}$$

$$\delta t \leq \frac{|K|}{\sum\limits_{\sigma\in\mathcal{E}(K)} |\sigma| \left(\widetilde{u}^*_{K,\sigma}\right)^-}, \quad \forall K \in \mathcal{M} \qquad \text{ensures that } \widetilde{\rho}_K/\rho^n_K > 0 \text{ by (24), it also guarantees that (36) and hence (37) are convex combinations.} \tag{38b}$$

The following proposition gathers stability properties of the scheme regarding the barotropic, kinetic and total energies.

Proposition 4.5. *We suppose that the CFL conditions (38) are satisfied and that a^n_K verifies the subcharacteristic condition (10). We have the following results.*

1. *The update of the pressure and the specific volume in the acoustic step verifies*

$$0 \leq \widetilde{\tau}_K, \quad \pi^n_K + (a^n_K)^2\tau^n_K = \widetilde{\pi}_K + (a^n_K)^2\widetilde{\tau}_K, \quad e^{\mathrm{EOS}}(\widetilde{\tau}_K) \leq e^{\mathrm{EOS}}(\tau^n_K) + \frac{\widetilde{\pi}^2_K - (\pi^n_K)^2}{2(a^n_K)^2}. \tag{39}$$

2. *The variables updated by the acoustic step (19) verify the following inequality*

$$\frac{|K|\rho^n_k}{\delta t}\left(e^{\mathrm{EOS}}(\widetilde{\tau}_K) - e^{\mathrm{EOS}}(\tau^n_K)\right) + |K|\widetilde{\pi}_K\left(\boldsymbol{\nabla}\cdot\widetilde{\mathbf{u}}\right)_K \leq 0. \tag{40}$$

3. *We have the following barotropic energy inequality for the overall scheme (35)*

$$\frac{|K|}{\delta t}\left(\rho^{n+1}_K e^{\mathrm{EOS}}(\tau^{n+1}_K) - \rho^n_K e^{\mathrm{EOS}}(\tau^n_K)\right) + \sum_{\sigma\in\mathcal{E}(K)} F_{K,\sigma} e^{\mathrm{EOS}}(\widetilde{\tau}_\sigma) + |K|\widetilde{\pi}_K\left(\boldsymbol{\nabla}\cdot\widetilde{\mathbf{u}}\right)_K \leq 0. \tag{41}$$

4. *We have the following kinetic energy inequality for the overall scheme (35)*

$$\frac{|D_\sigma|}{\delta t}\left(\rho^{n+1}_{D_\sigma}\frac{\left|\mathbf{u}^{n+1}_\sigma\right|^2}{2} - \rho^n_{D_\sigma}\frac{\left|\mathbf{u}^n_\sigma\right|^2}{2}\right) + \sum_{\varepsilon\in\mathcal{E}(D_\sigma)} \widetilde{F}_{\sigma,\varepsilon}\frac{\left|\widetilde{\mathbf{u}}_\varepsilon\right|^2}{2} + \widetilde{u}^*_{K,\sigma}|D_\sigma|\left(\boldsymbol{\nabla}\widetilde{\pi}\right)_\sigma\cdot\mathbf{n}_{K,\sigma} = -R_\sigma. \tag{42}$$

   with

$$R_\sigma = \widetilde{R}_\sigma + R^{n+1}_\sigma. \tag{43}$$

5. *For any integer $N \geq 0$, the overall scheme (35) satisfies the mathematical entropy inequality*

$$\sum_{K\in\mathcal{M}}|K|\rho^N_K e^{\mathrm{EOS}}(\tau^N_K) + \sum_{\sigma\in\mathcal{E}_{int}}|D_\sigma|\rho^N_{D_\sigma}\frac{\left|\mathbf{u}^N_\sigma\right|^2}{2} \leq \sum_{K\in\mathcal{M}}|K|\rho^0_K e^{\mathrm{EOS}}(\tau^0_K) + \sum_{\sigma\in\mathcal{E}_{int}}|D_\sigma|\rho^0_{D_\sigma}\frac{\left|\mathbf{u}^0_\sigma\right|^2}{2}. \tag{44}$$

Proof. The proof of this proposition is given in appendix C.2. ∎

We finally sum up the properties of the SLP scheme (35) in the following theorem.

Theorem 4.6 (Properties of the overall SLP IMEX scheme for the barotropic Euler system)**.** *Under CFL conditions (38) and the subcharacteristic conditions (10), the overall SLP IMEX scheme (35) satisfies the following properties:*

1. *the scheme is well-defined for any $\delta t > 0$ in the sense that the linear system involved in the acoustic step is well-posed,*
2. *the scheme is conservative with respect to ρ and $\rho\mathbf{u}$,*
3. *the scheme preserves the positivity of the density ρ_K^n for all $K \in \mathcal{M}$ and $n > 0$,*
4. *the scheme is endowed with a local discrete kinetic energy inequality,*
5. *the scheme is endowed with a local discrete barotropic energy inequality,*
6. *the scheme is endowed with an integral total energy inequality.*

Proof. Point 1 is a result of proposition 4.3. Point 2 follows from (35). The combination of the CFL conditions (38b), the first inequality of (39) and (37) provides point 3. Points 4, 5, and 6 are respectively consequences of (42), (41) and (44). □

Let us note that the CFL conditions (38) involve only the material velocity of the flow, as expected in an IMEX time integration framework. However these relations do not yield an explicit time step definition procedure. Indeed, the velocity $\widetilde{u}_{K,\sigma}$ appearing in these relations is itself determined by integrating the acoustic subsystem (19), which requires a time step to be specified beforehand. Moreover, Proposition 4.3 alone does not guarantee that ρ remains positive. In this sense, relations (38) can rather be used as a validation criterion for the chosen time step in a trial-and-error procedure. Let us consider the following CFL conditions

$$\delta t^{\text{pred}} \leq \frac{|D_\sigma|\rho^n_{D_\sigma}}{\displaystyle\sum_{\varepsilon\in\mathcal{E}(D_\sigma)} \left(F^n_{\sigma,\varepsilon}\right)^+}, \quad \forall \sigma \in \mathcal{E}_{int}, \qquad \delta t^{\text{pred}} \leq \frac{|K|}{\displaystyle\sum_{\sigma\in\mathcal{E}(K)} |\sigma| \left(u^n_{K,\sigma}\right)^-}, \quad \forall K \in \mathcal{M} \tag{45}$$

where $F^n_{\sigma,\varepsilon}$ is defined as specified in appendix A with $\widetilde{F}_{K,\sigma}$ replaced by $F^n_{K,\sigma} = |\sigma|\rho^n_K(u^n_{K,\sigma})^+ - |\sigma|\rho^n_L(u^n_{K,\sigma})^-$. In practice, we proceed as follows at each time iteration:

Step 1. Define a predicted time step δt^{pred} in agreement with the CFL condition (45) that only involve $u^n_{K,\sigma}$:

Step 2: Solve the acoustic subsystem (19) in order to determine $\widetilde{u}_{K,\sigma}$ with δt^{pred}.

Step 3: If the CFL conditions (38) are not verified return to Step 2 with a halved value $\delta t^{\text{pred}} \leftarrow \delta t^{\text{pred}}/2$, otherwise set $\delta t = \delta t^{\text{pred}}$ and proceed to the transport step.

Let us emphasize that, for all test cases presented in this work, the predicted time step δt^{pred} obtained from conditions (45) consistently satisfied the CFL conditions (38), so that the halving procedure was never triggered.

Algorithm 1 Time step selection and acoustic solve at each iteration

1: Compute δt^{pred} from the CFL condition (45) involving $u^n_{K,\sigma}$.
2: **repeat**
3: Solve the acoustic subsystem (19) with δt^{pred} to obtain $\widetilde{u}_{K,\sigma}$
4: **if** CFL conditions (38) are not satisfied **then**
5: $\delta t^{\text{pred}} \leftarrow \delta t^{\text{pred}}/2$
6: **end if**
7: **until** CFL conditions (38) are satisfied
8: Set $\delta t \leftarrow \delta t^{\text{pred}}$ and proceed to the transport step

5 The full Euler equations

In this section, we present an extension of the scheme for the Full Euler equations

$$\begin{cases} \partial_t \rho + \boldsymbol{\nabla} \cdot (\rho \mathbf{u}) = 0, & (46a) \\ \partial_t (\rho \mathbf{u}) + \boldsymbol{\nabla} \cdot (\rho \mathbf{u} \otimes \mathbf{u}) + \boldsymbol{\nabla} p = \mathbf{0}, & (46b) \\ \partial_t (\rho E) + \boldsymbol{\nabla} \cdot (\rho E \mathbf{u} + p \mathbf{u}) = 0, & (46c) \end{cases}$$

where E and $e = E - |\mathbf{u}^2|/2$ are respectively the total energy and the internal energy. We suppose that the fluid is governed by an EOS in the form of the mapping

$$(\tau, s) \in (0, +\infty) \times \mathbb{R} \mapsto e^{\text{EOS}}(\tau, s) > 0, \tag{47}$$

that verifies the Weyl assumptions [96]:

$$(\partial e^{\text{EOS}}/\partial \tau) < 0, \qquad (\partial e^{\text{EOS}}/\partial s) > 0, \qquad (\partial^2 e^{\text{EOS}}/\partial \tau^2) > 0, \tag{48a}$$
$$(\partial^2 e^{\text{EOS}}/\partial s^2) > 0, \quad \left(\partial^2 e^{\text{EOS}}/\partial s^2\right)\left(\partial^2 e^{\text{EOS}}/\partial \tau^2\right) > (\partial^2 e^{\text{EOS}}/\partial \tau \partial s), \quad (\partial^3 e^{\text{EOS}}/\partial \tau^3) > 0. \tag{48b}$$

The pressure p and and the temperature T of the material are then defined by $p = p^{\text{EOS}}(\tau, s) = -(\partial e^{\text{EOS}}/\partial \tau)$ and $T = T^{\text{EOS}}(\tau, s) = (\partial e^{\text{EOS}}/\partial s)$, so that the Gibbs relation reads

$$\mathrm{d}e = T \mathrm{d}s - p \mathrm{d}\tau. \tag{49}$$

By relations (48), one can define a mapping $(\tau, e) \mapsto s^{\text{EOS}}(\tau, e)$ such that $e = e^{\text{EOS}}(\tau, s)$ when $s = s^{\text{EOS}}(\tau, e)$. Moreover, (48) implies that both $(\tau, s) \mapsto e^{\text{EOS}}(\tau, s)$ and $(\tau, e) \mapsto -s^{\text{EOS}}(\tau, e)$ are strictly convex functions. At last, (48) guarantees that the sound velocity defined by $c = \tau\sqrt{-(\partial p^{\text{EOS}}/\partial \tau)_s}$ is real-valued.

5.1 Acoustic-transport splitting approach

Similar to the procedure followed with the barotropic system, for a regular solution, the divergence term of system (46) can be further developed using the chain's rule,

$$\partial_t \rho + \underbrace{\mathbf{u} \cdot \boldsymbol{\nabla} \rho}_{\text{transport}} + \underbrace{\rho \boldsymbol{\nabla} \cdot \mathbf{u}}_{\text{acoustic}} = 0, \tag{50a}$$

$$\partial_t (\rho \mathbf{u}) + \underbrace{(\mathbf{u} \cdot \boldsymbol{\nabla})(\rho \mathbf{u})}_{\text{transport}} + \underbrace{(\rho \mathbf{u}) \boldsymbol{\nabla} \cdot \mathbf{u} + \boldsymbol{\nabla} p}_{\text{acoustic}} = \mathbf{0}, \tag{50b}$$

$$\partial_t (\rho E) + \underbrace{(\mathbf{u} \cdot \boldsymbol{\nabla})(\rho E)}_{\text{transport}} + \underbrace{(\rho E) \boldsymbol{\nabla} \cdot \mathbf{u} + \boldsymbol{\nabla} \cdot (p \mathbf{u})}_{\text{acoustic}} = 0. \tag{50c}$$

Thus, we can divide the full Euler system to obtain two subsystems, the acoustic subsystem,

$$\begin{cases} \partial_t \rho + \rho \boldsymbol{\nabla} \cdot \mathbf{u} = 0, & (51a) \\ \partial_t (\rho \mathbf{u}) + (\rho \mathbf{u}) \boldsymbol{\nabla} \cdot \mathbf{u} + \boldsymbol{\nabla} p = \mathbf{0}, & (51b) \\ \partial_t (\rho E) + (\rho E) \boldsymbol{\nabla} \cdot \mathbf{u} + \boldsymbol{\nabla} \cdot (p \mathbf{u}) = 0, & (51c) \end{cases}$$

and using once again that for any smooth function $(\mathbf{x}, t) \mapsto \varphi$ we have $\mathbf{u} \cdot \boldsymbol{\nabla} \varphi = \boldsymbol{\nabla} \cdot (\varphi \mathbf{u}) - \varphi \boldsymbol{\nabla} \cdot \mathbf{u}$, the transport subsystem reads

$$\begin{cases} \partial_t \rho + \boldsymbol{\nabla} \cdot (\rho \mathbf{u}) - \rho \boldsymbol{\nabla} \cdot \mathbf{u} = 0, & (52a) \\ \partial_t (\rho \mathbf{u}) + \boldsymbol{\nabla} \cdot (\rho \mathbf{u} \otimes \mathbf{u}) - \rho \mathbf{u} \boldsymbol{\nabla} \cdot \mathbf{u} = \mathbf{0}, & (52b) \\ \partial_t (\rho E) + \boldsymbol{\nabla} \cdot (\rho E \mathbf{u}) - \rho E \boldsymbol{\nabla} \cdot \mathbf{u} = 0. & (52c) \end{cases}$$

Using both subsystems (51) and (52), we adop the two-step strategy described in section3.2: first, we solve the acoustic subsystem, then the transport subsystem. Both steps provide a discretization for (46). As detailed in the next section, both systems will not be expressed using the total energy E as the total energy involves degrees of freedom located at both the center and the faces of the primal cells. Following [56, 58, 61, 55], we will instead use a formulation of the system based on the internal energy. The use of this formulation requires adding corrective terms in the discretization of the internal energy in order to remain consistent with a global conservation of the total energy. These terms will be introduced in section 5.3.1 and section 5.3.2.

5.2 Acoustic and transport subsystems for the Euler equations

Considering regular solutions, the acoustic system (51) can be expressed using the variable τ, $\mathbf{u}$ and e as follows

$$\begin{cases} \rho \partial_t \tau - \boldsymbol{\nabla} \cdot \mathbf{u} = 0, & (53a) \\ \rho \partial_t \mathbf{u} + \boldsymbol{\nabla} p = \mathbf{0}, & (53b) \\ \rho \partial_t e + p \boldsymbol{\nabla} \cdot \mathbf{u} = 0. & (53c) \end{cases}$$

Similarly to (8a), the acoustic subsystem (53) retains a structure similar to one-dimensional Lagrangian gas dynamics, with two symmetrical nonlinear waves of velocity $\pm c$ separated by a stationary contact discontinuity. As for the barotropic system, we once again consider a Suliciu relaxation approximation of (53) that reads

$$\begin{cases} \rho\partial_t\tau - \boldsymbol{\nabla}\cdot\mathbf{u} = 0, & (54a)\\ \rho\partial_t\mathbf{u} + \boldsymbol{\nabla}\pi = \mathbf{0}, & (54b)\\ \rho\partial_t e + \pi\boldsymbol{\nabla}\cdot\mathbf{u} = 0, & (54c)\\ \rho\partial_t\pi + a^2\boldsymbol{\nabla}\cdot\mathbf{u} = 0. & (54d)\end{cases}$$

where $a > 0$ is again a constant approximation of the acoustic impedance that complies with the subcharacteristic condition (10). For the surrogate pressure π re-initialization at time step t^n, we impose that $\pi^n = p^{\mathrm{EOS}}(1/\rho^n, s^{\mathrm{EOS}}(1/\rho^n, e^n))$.

Let us now turn to the transport subsystem (52c): as for the acoustic step, we consider here the internal energy e instead of the total energy E. System (52c) (again for smooth solutions) is equivalent to

$$\begin{cases} \partial_t\rho + \boldsymbol{\nabla}\cdot(\rho\mathbf{u}) - \rho\boldsymbol{\nabla}\cdot\mathbf{u} = 0, & (55a)\\ \partial_t(\rho\mathbf{u}) + \boldsymbol{\nabla}\cdot(\rho\mathbf{u}\otimes\mathbf{u}) - \rho\mathbf{u}\boldsymbol{\nabla}\cdot\mathbf{u} = \mathbf{0}, & (55b)\\ \partial_t(\rho e) + \boldsymbol{\nabla}\cdot(\rho e\mathbf{u}) - \rho e\boldsymbol{\nabla}\cdot\mathbf{u} = 0. & (55c)\end{cases}$$

5.3 A staggered Lagrange-projection like (SLP) scheme for the full Euler system

In this section, we present the SLP scheme for the full Euler system of equations, where we discretize and resolve the full Euler acoustic (54) and the full Euler transport (55) subsystems, then, similar to the approach used for the barotropic system, we merge the solutions to construct the complete scheme.

The initial conditions for ρ and $\mathbf{u}$ are defined by (15), whereas that of the internal energy e is defined by

$$\forall\ K \in \mathcal{M}, \quad e_K^0 = \frac{1}{|K|}\int_K e_0(\mathbf{x})\mathrm{d}\mathbf{x}, \tag{56}$$

where we suppose $e_0 > 0$.

5.3.1 Discretization of the acoustic step

For solving the acoustic subsystem (51), we discretize the corresponding relaxation acoustic subsystem (54) as follow:

$$\forall K \in \mathcal{M}, \qquad \frac{|K|}{\delta t}\rho_K^n\left(\widetilde{\tau}_K - \tau_K^n\right) - |K|\left(\boldsymbol{\nabla}\cdot\widetilde{\mathbf{u}}\right)_K = 0, \tag{57a}$$

$$\forall \sigma \in \mathcal{E}_{int}, \qquad \frac{|D_\sigma|}{\delta t}\rho_{D_\sigma}^n\left(\widetilde{\mathbf{u}}_\sigma - \mathbf{u}_\sigma^n\right) + |D_\sigma|\left(\boldsymbol{\nabla}\widetilde{\pi}\right)_\sigma = \mathbf{0}, \tag{57b}$$

$$\forall K \in \mathcal{M}, \qquad \frac{|K|}{\delta t}\rho_K^n\left(\widetilde{e}_K - e_K^n\right) + \widetilde{\pi}_K|K|(\boldsymbol{\nabla}\cdot\widetilde{\mathbf{u}})_K = \widetilde{S}_K, \tag{57c}$$

$$\forall K \in \mathcal{M}, \qquad \frac{|K|}{\delta t}\rho_K^n\left(\widetilde{\pi}_K - \pi_K^n\right) + \left(a_K^n\right)^2|K|\left(\boldsymbol{\nabla}\cdot\widetilde{\mathbf{u}}\right)_K = 0, \tag{57d}$$

where equations (57a), (57b) and (57d) are the same mass, momentum and pressure equations respectively numbered (19a), (19b) and (19c) described in the barotropic section 4. The remaining equation (57c) is the approximation of the internal energy over the primal cell K. The discrete divergence of the velocity $(\boldsymbol{\nabla} \cdot \tilde{\mathbf{u}})_K$ and the discrete gradient of the pressure $(\boldsymbol{\nabla}\widetilde{\pi})_\sigma$ are respectively defined by (20a) and (20c), where a_K is defined by

$$a_K = \rho_K^n c^{\mathrm{EOS}}(1/\rho_K^n, e_K^n), \tag{58}$$

and a_{D_σ} is still given by (17). Lemma 4.1 can also be applied here, so that a kinetic energy balance holds with residual terms on the right-hand side. Following the strategy developed in [56, 58, 61, 55, 61], these residual terms are compensated for by a corrective term $\widetilde{S}_K$ in the discretization of the internal energy equation to guarantee the consistency of the scheme for weak solutions.

The corrective term $\widetilde{S}_K$ is designed with the objective of ensuring that the overall discretization provides a global conservation of the total energy. The term $\widetilde{S}_K$ is defined in a manner to compensate for the term $\widetilde{R}_\sigma$ in the discrete kinetic energy equation (21):

$$\forall K \in \mathcal{M}, \qquad \widetilde{S}_K = \sum_{\sigma \in \mathcal{E}(K)} \widetilde{S}_{K,\sigma}. \tag{59}$$

The terms $\widetilde{S}_{K,\sigma}$ and $\widetilde{S}_{L,\sigma}$ must be defined such that:

$$\widetilde{R}_\sigma = \widetilde{S}_{K,\sigma} + \widetilde{S}_{L,\sigma}, \quad \sigma = K|L. \tag{60}$$

This term arises from the definition of the density over the dual cells (28c), and from distributing the residual term between the two adjacent cells. Let $\sigma = K|L$, from (22), we perform the following decomposition:

$$\begin{aligned}
\widetilde{R}_\sigma = \frac{|D_\sigma|}{\delta t}\frac{\rho_{D_\sigma}^n}{2}|\tilde{\mathbf{u}}_\sigma - \mathbf{u}_\sigma^n|^2 + \frac{1}{2a_\sigma^n}|\sigma|\left(\widetilde{\pi}_L - \widetilde{\pi}_K\right)^2 \\
= \underbrace{\frac{|D_{K,\sigma}|}{\delta t}\frac{\rho_K^n}{2}|\tilde{\mathbf{u}}_\sigma - \mathbf{u}_\sigma^n|^2}_{\text{affected to K}} + \underbrace{\frac{|D_{L,\sigma}|}{\delta t}\frac{\rho_L^n}{2}|\tilde{\mathbf{u}}_\sigma - \mathbf{u}_\sigma^n|^2}_{\text{affected to L}} \\
+ \underbrace{\frac{|D_{K,\sigma}|}{|D_\sigma|}\frac{1}{2a_{D_\sigma}^n}|\sigma|\left(\widetilde{\pi}_L - \widetilde{\pi}_K\right)^2}_{\text{affected to K}} + \underbrace{\frac{|D_{L,\sigma}|}{|D_\sigma|}\frac{1}{2a_{D_\sigma}^n}|\sigma|\left(\widetilde{\pi}_L - \widetilde{\pi}_K\right)^2}_{\text{affected to L}}.
\end{aligned}$$

This suggests to set

$$\widetilde{S}_{K,\sigma} = \frac{|D_{K,\sigma}|}{\delta t}\frac{\rho_K^n}{2}|\tilde{\mathbf{u}}_\sigma - \mathbf{u}_\sigma^n|^2 + \frac{|D_{K,\sigma}|}{|D_\sigma|}\frac{1}{2a_{D_\sigma}^n}|\sigma|\left(\widetilde{\pi}_L - \widetilde{\pi}_K\right)^2, \quad \sigma = K|L. \tag{61}$$

Let us underline that with such definition, $\widetilde{S}_{K,\sigma} \geq 0$ for any $\delta t > 0$.

5.3.2 Discretization of the transport step

We first define the upwind scalar variable at each face:

$$\widetilde{\varphi}_\sigma = \begin{cases} \widetilde{\varphi}_K, & \text{if } \widetilde{u}_{K,\sigma}^* > 0, \\ \widetilde{\varphi}_L, & \text{otherwise,} \end{cases} \quad , \quad \text{for } \varphi \in \{\rho, e\}\,. \tag{62}$$

The transport subsystem (55) is discretized as follows:

$$\forall K \in \mathcal{M}, \qquad \frac{|K|}{\delta t}\left(\rho_K^{n+1} - \widetilde{\rho}_K\right) + \sum_{\sigma \in \mathcal{E}(K)} \widetilde{F}_{K,\sigma} - \widetilde{\rho}_K |K| \left(\boldsymbol{\nabla} \cdot \widetilde{\mathbf{u}}\right)_K = 0, \tag{63a}$$

$$\forall \sigma \in \mathcal{E}_{int}, \quad \frac{|D_\sigma|}{\delta t}\left(\rho_{D_\sigma}^{n+1} \mathbf{u}_\sigma^{n+1} - \widetilde{\rho}_{D_\sigma} \widetilde{\mathbf{u}}_\sigma\right) + \sum_{\varepsilon \in \mathcal{E}(D_\sigma)} \widetilde{F}_{\sigma,\varepsilon} \widetilde{\mathbf{u}}_\varepsilon - \widetilde{\rho}_{D_\sigma} \widetilde{\mathbf{u}}_\sigma |D_\sigma| \left(\boldsymbol{\nabla} \cdot \widetilde{\mathbf{u}}\right)_{D_\sigma} = \mathbf{0}, \tag{63b}$$

$$\forall K \in \mathcal{M}, \qquad \frac{|K|}{\delta t}\left(\rho_K^{n+1} e_K^{n+1} - \widetilde{\rho}_K \widetilde{e}_K\right) + \sum_{\sigma \in \mathcal{E}(K)} \widetilde{F}_{K,\sigma} \widetilde{e}_\sigma - \widetilde{\rho}_K \widetilde{e}_K |K| \left(\boldsymbol{\nabla} \cdot \widetilde{\mathbf{u}}\right)_K = S_K^{n+1}, \tag{63c}$$

where equations (63a) and (63b) are the same mass and momentum equations of system (27), described in the barotropic section (4), respectively, with the discrete divergence of the velocity $\left(\boldsymbol{\nabla} \cdot \widetilde{\mathbf{u}}\right)_{D_\sigma}$ is defined by (32) from Lemma 4.4. The remaining equation (63c) is the discrete internal energy balance. Moreover, a kinetic energy balance with residual terms on the right-hand-side holds according to Lemma 4.4, and in order to preserve the consistency of the scheme, these residual terms are compensated in the internal energy balance discretization, similarly to the acoustic subsystem. Accordingly, the term S_K^{n+1} needs to be defined in a way to compensate for the term R_σ^{n+1} in the discrete kinetic energy equation (33):

$$S_K^{n+1} = \sum_{\sigma \in \mathcal{E}(K)} S_{K,\sigma}^{n+1}, \tag{64}$$

with

$$R_\sigma^{n+1} = S_{K,\sigma}^{n+1} + S_{L,\sigma}^{n+1}, \quad \sigma = K|L. \tag{65}$$

As with the acoustic subsystem, the term comes from using the definition of $\rho_{D_\sigma}^n$ and dispatching the residual term over the two adjacent cells. Let $\sigma = K|L$, from (34), on can write

$$\begin{aligned} R_\sigma^{n+1} &= \frac{|D_\sigma|}{\delta t} \frac{\rho_{D_\sigma}^n}{2} \left|\mathbf{u}_\sigma^{n+1} - \widetilde{\mathbf{u}}_\sigma\right|^2 - \sum_{\varepsilon \in \mathcal{E}(D_\sigma)} \frac{\widetilde{F}_{\sigma,\varepsilon}}{2} \left|\mathbf{u}_\sigma^{n+1} - \widetilde{\mathbf{u}}_\varepsilon\right|^2 \\ &= \underbrace{\frac{|D_{K,\sigma}|}{\delta t} \frac{\rho_K^n}{2} \left|\mathbf{u}_\sigma^{n+1} - \widetilde{\mathbf{u}}_\sigma\right|^2}_{\text{affected to K}} + \underbrace{\frac{|D_{L,\sigma}|}{\delta t} \frac{\rho_L^n}{2} \left|\mathbf{u}_\sigma^{n+1} - \widetilde{\mathbf{u}}_\sigma\right|^2}_{\text{affected to L}} \\ &\quad - \underbrace{\sum_{\varepsilon \in \widetilde{\mathcal{E}}(D_{K,\sigma})} \alpha_{K,\varepsilon} \frac{\widetilde{F}_{\sigma,\varepsilon}}{2} \left|\mathbf{u}_\sigma^{n+1} - \widetilde{\mathbf{u}}_\varepsilon\right|^2}_{\text{affected to K}} - \underbrace{\sum_{\varepsilon \in \widetilde{\mathcal{E}}(D_{L,\sigma})} \alpha_{L,\varepsilon} \frac{\widetilde{F}_{\sigma,\varepsilon}}{2} \left|\mathbf{u}_\sigma^{n+1} - \widetilde{\mathbf{u}}_\varepsilon\right|^2}_{\text{affected to L}} \end{aligned}$$

Therefore, we define the term $S_{K,\sigma}^{n+1}$ as follows:

$$S_{K,\sigma}^{n+1} = \frac{|D_{K,\sigma}|}{\delta t} \frac{\rho_K^n}{2} \left|\mathbf{u}_\sigma^{n+1} - \widetilde{\mathbf{u}}_\sigma\right|^2 - \sum_{\varepsilon \in \widetilde{\mathcal{E}}(D_{K,\sigma})} \alpha_{K,\varepsilon} \frac{\widetilde{F}_{\sigma,\varepsilon}}{2} \left|\mathbf{u}_\sigma^{n+1} - \widetilde{\mathbf{u}}_\varepsilon\right|^2, \tag{66}$$

where $\widetilde{\mathcal{E}}\left(D_{K,\sigma}\right)$ is defined in equation (12) and $\alpha_{K,\varepsilon}$ is a coefficient used to distribute the dual flux over the neighboring primal cells. For the RT/CR discretization, the dual face ε is always included in the primal cell. For the MAC discretization, only some dual faces are included in the primal cell and in this case, $\alpha_{K,\varepsilon} = 1$. Consequently, the residual term R_σ^{n+1} is entirely attributed to the cell

K. In the MAC discretization, if the dual face lies on the boundary of the primal cell, we have:

$$\alpha_{K,\varepsilon} = \begin{cases} 1, & \text{if } \varepsilon \subset K, \\ \dfrac{|D_{K,\sigma}|}{|D_\sigma|}, & \text{if } \varepsilon \cap \partial K \neq \emptyset, \end{cases} \quad \text{for } \varepsilon \in \widetilde{\mathcal{E}}\,(D_{K,\sigma})\,. \tag{67}$$

For a uniform grid, this simplifies to $\alpha_{K,\varepsilon} = 1/2$. The non-negativity of $S^{n+1}_{K,\sigma}$ is ensured by the CFL condition (70c) given hereafter. In the following, we will show that this discretization enables the discrete unknowns to comply with an integral conservation law for the total energy.

5.3.3 Overall scheme and properties

As for the barotropic case, the overall **SLP** scheme for the full Euler system of equations is obtained by injecting the update of the acoustic step (57) into the transport step (63), which gives

$$\forall K \in \mathcal{M}, \qquad \frac{|K|}{\delta t}\left(\rho_K^{n+1} - \rho_K^n\right) + \sum_{\sigma \in \mathcal{E}(K)} \widetilde{F}_{K,\sigma} = 0, \tag{68a}$$

$$\forall \sigma \in \mathcal{E}_{int}, \qquad \frac{|D_\sigma|}{\delta t}\left(\rho_{D_\sigma}^{n+1}\mathbf{u}_\sigma^{n+1} - \rho_{D_\sigma}^n \mathbf{u}_\sigma^n\right) + \sum_{\varepsilon \in \mathcal{E}(D_\sigma)} \widetilde{F}_{\sigma,\varepsilon}\widetilde{\mathbf{u}}_\varepsilon + |D_\sigma|\left(\boldsymbol{\nabla}\widetilde{\pi}\right)_\sigma = \mathbf{0}, \tag{68b}$$

$$\forall K \in \mathcal{M}, \qquad \frac{|K|}{\delta t}\left(\rho_K^{n+1}e_K^{n+1} - \rho_K^n e_K^n\right) + \sum_{\sigma \in \mathcal{E}(K)} \widetilde{F}_{K,\sigma}\widetilde{e}_\sigma + |K|\widetilde{\pi}_K\left(\boldsymbol{\nabla}\cdot\widetilde{\mathbf{u}}\right)_K = S_K, \tag{68c}$$

with

$$S_K = \widetilde{S}_K + S_K^{n+1}. \tag{69}$$

As for the barotropic case, CFL conditions will ensure stability properties for the scheme. These conditions are gathered below.

$$\delta t \leq \frac{|D_\sigma|\rho^n_{D_\sigma}}{\displaystyle\sum_{\varepsilon \in \mathcal{E}(D_\sigma)} \widetilde{F}^+_{\sigma,\varepsilon}}, \quad \forall \sigma \in \mathcal{E}_{int} \qquad \text{ensures that } R^{n+1}_\sigma \geq 0 \text{ as defined in (34)}, \tag{70a}$$

$$\delta t \leq \frac{|K|}{\displaystyle\sum_{\sigma \in \mathcal{E}(K)} |\sigma|\left(\widetilde{u}^*_{K,\sigma}\right)^-}, \quad \forall K \in \mathcal{M} \qquad \text{ensures that } \widetilde{\rho}_K/\rho^n_K > 0 \text{ by (24), it also guarantees that (36) and hence (37) are convex combinations.} \tag{70b}$$

$$\delta t \leq \frac{|D_{K,\sigma}|\rho^n_K}{\displaystyle\sum_{\varepsilon \in \mathcal{E}(D_{K,\sigma})} \alpha_{K,\varepsilon}\widetilde{F}^+_{\sigma,\varepsilon}}, \quad \forall K \in \mathcal{M}, \qquad \text{ensures that } S^{n+1}_K \geq 0 \text{ as defined by (64) and (66).} \tag{70c}$$

Let us underline that (70a)-(70b) are the same CFL conditions as the CFL conditions (38a)-(38b) of the barotropic case. In the sequel, we will note $\widetilde{s}_K = s^{\mathrm{EOS}}(\widetilde{\tau}_K, \widetilde{e}_K)$, $s^n_K = s^{\mathrm{EOS}}(\tau^n_K, e^n_K)$ and $\widetilde{s}_\sigma = s^{\mathrm{EOS}}(\widetilde{\tau}_\sigma, \widetilde{e}_\sigma)$. The following proposition gathers stability properties of the scheme regarding the barotropic, kinetic and total energies. Its proof is given in appendix C.3.

Proposition 5.1. *We suppose that the CFL conditions (70) are satisfied and that a^n_K verifies the subcharacteristic condition (10). We have the following results.*

1. *The update of the pressure and the specific volume in the acoustic step verify*

$$0 \le \widetilde{\tau}_K, \qquad \pi_K^n + (a_K^n)^2 \tau_K^n = \widetilde{\pi}_K + (a_K^n)^2 \widetilde{\tau}_K, \qquad e^{\mathrm{EOS}}(\widetilde{\tau}_K, s_K^n) \le e_K^n + \frac{\widetilde{\pi}_K^2 - (\pi_K^n)^2}{2(a_K^n)^2}. \tag{71}$$

2. *The update of the entropy and the internal energy in the acoustic step verify*

$$s_K^n \le \widetilde{s}_K, \qquad\qquad \widetilde{e}_K \ge 0. \tag{72}$$

3. *The update of the density* (63a) *and the internal energy* (63c) *in the transport step read*

$$\rho_K^{n+1} = \mathrm{Cvx}(\widetilde{\rho})_K, \qquad\qquad \rho_K^{n+1} e_K^{n+1} = \mathrm{Cvx}(\widetilde{\rho e})_K + \frac{\delta t}{|K|} S_K^{n+1}. \tag{73}$$

4. *The corrective term S_K^{n+1} associated with the transport step* (63) *for the internal energy is non-negative*

$$S_K^{n+1} \ge 0. \tag{74}$$

5. *The variables updated by the transport step* (63) *verify the following inequality*

$$-|K| \frac{\rho_K^{n+1} s_K^{n+1} - \widetilde{\rho}_K \widetilde{s}_K}{\delta t} + \sum_{\sigma \in \mathcal{E}(K)} \widetilde{F}_{K,\sigma} (-\tilde{s})_\sigma + |K| \widetilde{\rho}_K \widetilde{s}_K \left(\boldsymbol{\nabla} \cdot \widetilde{\mathbf{u}} \right)_K \le 0. \tag{75}$$

6. *The overall scheme* (68) *satisfies the discrete entropy inequality*

$$-|K| \frac{\rho_K^{n+1} s_K^{n+1} - \rho_K^n s_K^n}{\delta t} + \sum_{\sigma \in \mathcal{E}(K)} \widetilde{F}_{K,\sigma} (-\tilde{s})_\sigma \le 0. \tag{76}$$

7. *For any integer $N \ge 0$, the overall scheme* (68) *satisfies the integral total energy conservation relation*

$$\sum_{K \in \mathcal{M}} |K| \rho_K^N e_K^N + \sum_{\sigma \in \mathcal{E}_{int}} |D_\sigma| \rho_{D_\sigma}^N \frac{\left| \mathbf{u}_\sigma^N \right|^2}{2} = \sum_{K \in \mathcal{M}} |K| \rho_K^0 e_K^0 + \sum_{\sigma \in \mathcal{E}_{int}} |D_\sigma| \rho_{D_\sigma}^0 \frac{\left| \mathbf{u}_\sigma^0 \right|^2}{2}. \tag{77}$$

Theorem 5.2 (Properties of the overall SLP IMEX scheme for the full Euler system)**.** *Under the CFL conditions* (70) *and the subcharacteristic conditions* (10)*, the overall SLP scheme* (68) *satisfies the following properties:*

1. *the scheme is well-defined for any $\delta t > 0$ in the sense that the linear system involved in the acoustic step is well-posed,*
2. *the scheme is conservative with respect to ρ and $\rho\mathbf{u}$,*
3. *the scheme is globally conservative with respect to the total energy ρE,*
4. *the scheme preserves the positivity of the density ρ_K^n for all $K \in \mathcal{M}$ and $n > 0$,*
5. *the scheme preserves the positivity of the internal energy e_K^n for all $K \in \mathcal{M}$ and $n > 0$,*
6. *the scheme is endowed with a local discrete kinetic energy inequality,*
7. *the scheme is endowed with a local discrete entropy inequality,*
8. *the scheme verifies a discrete local conservation property for total energy (on the dual mesh).*

Proof. Point 1 is a result of proposition 4.3, as the pressure-velocity system issued from acoustic step (57) is the same as the system (57) of the barotropic case. Point 2 and point 3 are respectively consequences of (68) and (77). Point 4 is obtained by combining (70b), the first inequality of (71) and the first relation of (73). Using (71), (73) and (74) yields the proof of point 5. Lemmas 4.1 and 4.4 that were derived for the barotropic system are still in this case. Therefore, the discrete update of the kinetic energy is also given by (42), which proves point 6. Point 7 is a straightforward consequence of (76). The proof of point 8 is provided later in section 6.

□

6 Full Euler system: local conservation of the total energy over the dual mesh

In this section, taking inspiration from the work of [42], we will show that it is possible to define discrete values of the internal energy associated with the dual cells of the mesh along with its update process. We will proceed by considering internal energies densities $(\rho e)^n_{K,\sigma}$ defined on the half dual cells $D_{K,\sigma}$, $K \in \mathcal{M}$, $\sigma \in \mathcal{E}(K)$ such that their evolution is consistent with the internal energy update on the primal mesh. This will enable the definition of a discrete total energy $(\rho E)^n_{D_\sigma}$ associated with the dual cells $\sigma \in \mathcal{E}$ which satisfies a local conservative update. For the sake of brevity, we only detail the RT/CR discretization. Let us mention that the MAC discretization differs slightly, as it admits a dual mesh associated with each spatial direction. Nevertheless, for each such dual mesh, the derivation outlined hereafter can be easily adapted to yield a discrete total energy conservation update.

For any $K \in \mathcal{M}$ and $\sigma \in \mathcal{E}(K)$ we can define the density of internal energy $(\rho e)^n_{K,\sigma}$ associated with the half dual cells $D_{K,\sigma}$ so that

$$|K|\rho^n_K e^n_K = \sum_{\sigma\in\mathcal{E}(K)} |D_{K,\sigma}|(\rho e)^n_{K,\sigma}. \tag{78}$$

We define the update value $(\rho e)^{n+1}_{K,\sigma}$ by setting

$$\frac{|D_{K,\sigma}|}{\delta t}\Big((\rho e)^{n+1}_{K,\sigma} - (\rho e)^n_{K,\sigma}\Big) + \sum_{\varepsilon\in\mathcal{E}(D_{K,\sigma})} \widetilde{F}_{K,\sigma,\varepsilon}\widetilde{e}_\varepsilon + |D_{K,\sigma}|\widetilde{\pi}_K\,(\boldsymbol{\nabla}\cdot\widetilde{\mathbf{u}})_{K,\sigma} = S_{K,\sigma}, \tag{79}$$

where

$$S_{K,\sigma} = \widetilde{S}_{K,\sigma} + S^{n+1}_{K,\sigma} \tag{80a}$$

$$|D_{K,\sigma}|\,(\boldsymbol{\nabla}\cdot\widetilde{\mathbf{u}})_{K,\sigma} = \sum_{\varepsilon\in\mathcal{E}(D_{K,\sigma})} |\varepsilon|\widetilde{u}_{K,\sigma,\varepsilon}, \tag{80b}$$

$$(\widetilde{F}_{K,\sigma,\varepsilon}, \widetilde{u}_{K,\sigma,\varepsilon}, \widetilde{e}_\varepsilon) = \begin{cases} \Big(\widetilde{F}_{\sigma,\varepsilon}, (\widetilde{\mathbf{u}}_\varepsilon\cdot\mathbf{n}_{K,\sigma,\varepsilon}), \widetilde{e}_K\Big), & \text{if } \varepsilon\in\widetilde{\mathcal{E}}(D_{K,\sigma}),\\ (\widetilde{F}_{K,\sigma}, \widetilde{u}^*_{K,\sigma}, \widetilde{e}_\sigma), & \text{if } \varepsilon=\sigma. \end{cases} \tag{80c}$$

Let us now define the total energy $(\rho E)^n_{D_\sigma}$ associated with the dual cell D_σ by

$$|D_\sigma|(\rho E)^n_{D_\sigma} = |D_\sigma|\rho^n_{D_\sigma}\frac{|\mathbf{u}^n_\sigma|^2}{2} + |D_{K,\sigma}|(\rho e)^n_{K,\sigma} + |D_{L,\sigma}|(\rho e)^n_{L,\sigma}, \quad \text{for } \sigma = K|L, \tag{81}$$

and set for any $\varepsilon \in \mathcal{E}(D_\sigma)$

$$\widetilde{\pi}_\varepsilon = \begin{cases} \widetilde{\pi}_K, & \text{if } \varepsilon \subset \overline{K} \\ \widetilde{\pi}_L, & \text{if } \varepsilon \subset \overline{L} \end{cases} \tag{82}$$

Proposition 6.1. *Let us consider $\sigma \in \mathcal{E}$, $\sigma = K|L$, the SLP scheme for the full Euler system verifies the following properties.*

1. *The update of the half dual cell internal energy is consistent with the update of the internal energy over the primal mesh as*

$$|K|\rho_K^{n+1} e_K^{n+1} = \sum_{\sigma \in \mathcal{E}(K)} |D_{K,\sigma}|(\rho e)_{K,\sigma}^{n+1}. \tag{83}$$

2. *The update of the internal energy in the dual cell D_σ is*

$$\begin{aligned} \frac{|D_{K,\sigma}|}{\delta t}(\rho e)_{K,\sigma}^{n+1} + \frac{|D_{L,\sigma}|}{\delta t}(\rho e)_{L,\sigma}^{n+1} &= \frac{|D_{K,\sigma}|}{\delta t}(\rho e)_{K,\sigma}^{n} + \frac{|D_{L,\sigma}|}{\delta t}(\rho e)_{L,\sigma}^{n} \\ &- \sum_{\varepsilon \in \mathcal{E}(D_\sigma)} \widetilde{F}_{\sigma,\varepsilon} \widetilde{e}_\varepsilon - |\sigma|(\widetilde{\pi}_K - \widetilde{\pi}_L)\widetilde{u}_{K,\sigma}^* - \sum_{\varepsilon \in \mathcal{E}(D_\sigma)} |\varepsilon| \widetilde{\pi}_\varepsilon u_\varepsilon + R_\sigma. \end{aligned} \tag{84}$$

3. *The discrete total energy defined over the dual mesh verifies the following conservative update relation*

$$\frac{|D_\sigma|}{\delta t}\Big((\rho E)_{D_\sigma}^{n+1} - (\rho E)_{D_\sigma}^{n}\Big) + \sum_{\varepsilon \in \mathcal{E}(D_\sigma)} \widetilde{F}_{\sigma,\varepsilon}\left[\frac{|\widetilde{\mathbf{u}}_\varepsilon|^2}{2} + \widetilde{e}_\varepsilon\right] + \sum_{\varepsilon \in \mathcal{E}(D_\sigma)} |\varepsilon| \widetilde{\pi}_\varepsilon \widetilde{u}_\varepsilon = 0. \tag{85}$$

Proof. Let us proove point 1: by (79), we have

$$\begin{aligned} \sum_{\sigma \in \mathcal{E}(K)} |D_{K,\sigma}|(\rho e)_{K,\sigma}^{n+1} &= \sum_{\sigma \in \mathcal{E}(K)} |D_{K,\sigma}|(\rho e)_{K,\sigma}^{n} - \delta t \sum_{\sigma \in \mathcal{E}(K)} \left[\widetilde{F}_{K,\sigma}\widetilde{e}_\sigma + \sum_{\varepsilon \in \widetilde{\mathcal{E}}(D_{K,\sigma})} \widetilde{F}_{\sigma,\varepsilon}\widetilde{e}_K\right] \\ &- \delta t\, \widetilde{\pi}_K \sum_{\sigma \in \mathcal{E}(K)} |D_{K,\sigma}|\,(\boldsymbol{\nabla} \cdot \widetilde{\mathbf{u}})_{K,\sigma} + \sum_{\sigma \in \mathcal{E}(K)} S_{K,\sigma}. \end{aligned} \tag{86}$$

Granted that

$$\sum_{\sigma \in \mathcal{E}(K)} \sum_{\varepsilon \in \widetilde{\mathcal{E}}(D_{K,\sigma})} \widetilde{F}_{\sigma,\varepsilon} = 0, \tag{87}$$

by (78), (80a), (66) and (61), we get

$$\sum_{\sigma \in \mathcal{E}(K)} |D_{K,\sigma}|(\rho e)_{K,\sigma}^{n+1} = |K|(\rho e)_{K,\sigma}^{n} - \delta t \sum_{\sigma \in \mathcal{E}(K)} \widetilde{F}_{K,\sigma}\widetilde{e}_\sigma - \delta t\, \widetilde{\pi}_K \sum_{\sigma \in \mathcal{E}(K)} |D_{K,\sigma}|\,(\boldsymbol{\nabla} \cdot \widetilde{\mathbf{u}})_{K,\sigma} + S_K. \tag{88}$$

However, accounting for

$$\sum_{\sigma \in \mathcal{E}(K)} \sum_{\varepsilon \in \widetilde{\mathcal{E}}(D_{K,\sigma})} |\varepsilon|(\widetilde{\mathbf{u}}_\varepsilon \cdot \mathbf{n}_{K,\sigma,\varepsilon}) = 0, \tag{89}$$

we obtain that

$$\sum_{\sigma\in\mathcal{E}(K)} |D_{K,\sigma}|\,(\boldsymbol{\nabla}\cdot\widetilde{\mathbf{u}})_{K,\sigma} = \sum_{\sigma\in\mathcal{E}(K)} \left[|\sigma|\widetilde{u}^*_{K,\sigma} + \sum_{\varepsilon\in\widetilde{\mathcal{E}}(D_{K,\sigma})} |\varepsilon|(\widetilde{\mathbf{u}}_\varepsilon\cdot\mathbf{n}_{K,\sigma,\varepsilon})\right]$$
$$= \sum_{\sigma\in\mathcal{E}(K)} |\sigma|\widetilde{u}^*_{K,\sigma} = |K|\,(\boldsymbol{\nabla}\cdot\widetilde{\mathbf{u}})_K \tag{90}$$

so that (88) becomes

$$\sum_{\sigma\in\mathcal{E}(K)} |D_{K,\sigma}|(\rho e)^{n+1}_{K,\sigma} = |K|(\rho e)^n_{K,\sigma} - \delta t \sum_{\sigma\in\mathcal{E}(K)} \widetilde{F}_{K,\sigma}\widetilde{e}_\sigma - \delta t\,\widetilde{\pi}_K|K|\,(\boldsymbol{\nabla}\cdot\widetilde{\mathbf{u}})_{K,\sigma} + S_K. \tag{91}$$

By comparing (91) with the update of internal energy over the primal mesh (68c), we get (83).

Let us now consider point 2: for $\sigma = K|L$, granted that $\widetilde{\mathcal{E}}(D_{K,\sigma})\cup\widetilde{\mathcal{E}}(D_{L,\sigma}) = \mathcal{E}(D_\sigma)$ we first observe that

$$\begin{aligned}|D_{K,\sigma}|\widetilde{\pi}_K\,(\boldsymbol{\nabla}\cdot\widetilde{\mathbf{u}})_{K,\sigma} &+ |D_{L,\sigma}|\widetilde{\pi}_L\,(\boldsymbol{\nabla}\cdot\widetilde{\mathbf{u}})_{L,\sigma}\\
&= |\sigma|(\widetilde{\pi}_K\widetilde{u}^*_{K,\sigma} + \widetilde{\pi}_L\widetilde{u}^*_{L,\sigma}) + \sum_{\varepsilon\in\widetilde{\mathcal{E}}(D_{K,\sigma})} |\varepsilon|\widetilde{\pi}_K u_\varepsilon + \sum_{\varepsilon\in\widetilde{\mathcal{E}}(D_{L,\sigma})} |\varepsilon|\widetilde{\pi}_L u_\varepsilon\\
&= |\sigma|(\widetilde{\pi}_K - \widetilde{\pi}_L)\widetilde{u}^*_{K,\sigma} + \sum_{\varepsilon\in\mathcal{E}(D_\sigma)} |\varepsilon|\widetilde{\pi}_\varepsilon u_\varepsilon\end{aligned} \tag{92}$$

Accounting for $\widetilde{F}_{K,\sigma}\widetilde{e}_\sigma = -\widetilde{F}_{L,\sigma}\widetilde{e}_\sigma$ we also remark that

$$\begin{aligned}\sum_{\varepsilon\in\mathcal{E}(D_{K,\sigma})} \widetilde{F}_{\sigma,\varepsilon}\widetilde{e}_\varepsilon + \sum_{\varepsilon\in\mathcal{E}(D_{L,\sigma})} \widetilde{F}_{L,\sigma,\varepsilon}\widetilde{e}_\varepsilon &= \widetilde{F}_{K,\sigma}\widetilde{e}_\sigma + \sum_{\varepsilon\in\widetilde{\mathcal{E}}(D_{K,\sigma})} \widetilde{F}_{\sigma,\varepsilon}\widetilde{e}_\varepsilon + \widetilde{F}_{L,\sigma}\widetilde{e}_\sigma + \sum_{\varepsilon\in\widetilde{\mathcal{E}}(D_{L,\sigma})} \widetilde{F}_{L,\sigma,\varepsilon}\widetilde{e}_\varepsilon\\
&= \sum_{\varepsilon\in\mathcal{E}(D_\sigma)} \widetilde{F}_{\sigma,\varepsilon}\widetilde{e}_\varepsilon.\end{aligned} \tag{93}$$

Then, using (65) and summing (79) over all both dual cells $D_{K,\sigma}$ and $D_{L,\sigma}$ of $\mathcal{D}_\sigma$, we obtain (84).

Finally, for point 3: the total energy update (85) in D_σ is obtained by taking the sum of (84) and (42). □

It is worth making the following two remarks concerning the reconstruction of the internal energy in the dual half-cells $D_{K,\sigma}$ and dual cells D_σ. First, at $t = 0$ (i.e., for $n = 0$), a natural initialization consists in setting $(\rho e)^0_{K,\sigma} = (\rho e)^0_K$ for all $K \in \mathcal{M}$ and $\sigma\in\mathcal{E}(K)$, which immediately allows one to verify (78). Nevertheless, it should be noted that, *a priori*, the updates defined by (79) do not ensure that $(\rho e)^n_{K,\sigma} = (\rho e)^n_K$ at later times t^n, for $n > 0$. Second, the update relation (79) does not *a priori* ensure that $(\rho e)^n_{K,\sigma} > 0$ nor that $|D_{K,\sigma}|(\rho e)^n_{K,\sigma} + |D_{L,\sigma}|(\rho e)^n_{L,\sigma} > 0$ for $n > 0$ and $\sigma = K|L$, although $(\rho e)^n_K > 0$ is guaranteed by theorem 5.2 under the CFL conditions (70) and the subcharacteristic conditions (10).

7 Low Mach behavior of the SLP scheme

This section offers a short examination of the SLP scheme under low Mach conditions. Our objective is not to provide an exhaustive analysis but to analyze the behavior of key stability and well-posedness properties in this regime. More precisely, we will assess the CFL conditions (38) and (70) as well as the linear system (19b)-(19c) associated with the acoustic steps (19) and (57) in this regime. As a first step, we outline the standard description of the low Mach regime based on the classical non-dimensional form of the equations of the flow. Let us define the following dimensionless variables

$$t' = t/t_0, \qquad \mathbf{x}' = \mathbf{x}/x_0, \qquad \mathbf{u}' = \mathbf{u}/u_0, \qquad e' = e/e_0, \qquad p' = p/p_0, \qquad c' = c/c_0, \tag{94}$$

where the quantities with subscript 0 denote the characteristic magnitudes of time (t_0), length (x_0), velocity (u_0), internal energy (e_0), pressure (p_0), and sound speed (c_0). Here $p_0 = \rho_0 c_0^2$, $e_0 = p_0/\rho_0$, $u_0 = x_0/t_0$, and $M = u_0/c_0$ denotes the Mach number. For the sake of readibilty we will make a slight abuse of notation and drop the prime while mentioning non-dimensional quantities.

The non-dimensional Euler equations can be written as

$$\partial_t \rho + \boldsymbol{\nabla} \cdot (\rho \mathbf{u}) = 0, \tag{95a}$$

$$\partial_t (\rho \mathbf{u}) + \boldsymbol{\nabla} \cdot (\rho \mathbf{u} \otimes \mathbf{u}) + \frac{1}{M^2} \boldsymbol{\nabla} p = 0, \tag{95b}$$

$$\partial_t \left(\rho \frac{|\mathbf{u}|^2}{2} + \frac{\rho e}{M^2} \right) + \boldsymbol{\nabla} \cdot \left[\left(\rho \frac{|\mathbf{u}|^2}{2} + \frac{\rho e}{M^2} \right) \mathbf{u} + \frac{p \mathbf{u}}{M^2} \right] = 0. \tag{95c}$$

When $M \ll 1$, the factor $1/M^2$ in the momentum equation implies that $\nabla p = \mathcal{O}(M^2)$. As for the discretized variables, this assumption translates into

$$\pi_K - \pi_L = \mathcal{O}(M^2), \tag{96}$$

for any neighbouring cells K and L. Using (96), the definition (20b) yields

$$\widetilde{u}^*_{K,\sigma} = \mathbf{u}_\sigma \cdot \mathbf{n}_{K,\sigma} - \frac{1}{2 a^n_{D_\sigma}} \frac{\widetilde{\pi}_L - \widetilde{\pi}_K}{M} = \mathbf{u}_\sigma \cdot \mathbf{n}_{K,\sigma} + \mathcal{O}(M), \quad K \in \mathcal{M}, \sigma \in \mathcal{E}(K). \tag{97}$$

By (28a) the mass flux in adimensional form across $\sigma = K|L$ reads

$$\widetilde{F}_{K,\sigma} = |\sigma| \widetilde{\rho}_\sigma \mathbf{u}_\sigma \cdot \mathbf{n}_{K,\sigma} + \mathcal{O}(M) = \mathcal{O}(M^0) + \mathcal{O}(M). \tag{98}$$

Now let $\sigma \in \mathcal{E}_{\text{int}}$ and $\varepsilon \in \mathcal{E}(D_\sigma)$, as detailed in Appendix A, $\widetilde{F}_{\sigma,\varepsilon}$ can be expressed as a fixed linear combination of $\widetilde{F}_{K,\sigma'}$ whose coefficients are of magnitude $\mathcal{O}(M^0)$ for $K \in \mathcal{M}$ and $\sigma' \in \mathcal{E}(K)$ in the neighbourhood of σ. Therefore, we get

$$\widetilde{F}_{\sigma,\varepsilon} = \mathcal{O}(M^0) + \mathcal{O}(M). \tag{99}$$

Relations (98) and (99) imply that the dimensional fluxes $\widetilde{F}_{K,\sigma}$ and $\widetilde{F}_{\sigma,\varepsilon}$ are respectively of magnitude $|\sigma| \rho_0 u_0 \big(\mathcal{O}(M^0) + \mathcal{O}(M)\big)$ and $|\varepsilon| \rho_0 u_0 \big(\mathcal{O}(M^0) + \mathcal{O}(M)\big)$. Consequently, in the regime $M \ll 1$ the CFL conditions (38) and (70) yield constraints on δt of the form (using dimensional expressions)

$$\delta t \sum_{\sigma\in\mathcal{E}(K)} \frac{|\sigma|}{|K|} u_0 \left(\mathcal{O}(M^0) + \mathcal{O}(M)\right) \leq 1, \qquad \forall K \in \mathcal{M}, \tag{100a}$$

$$\delta t \sum_{\varepsilon\in\mathcal{E}(D_\sigma)} \frac{|\varepsilon|}{|D_\sigma|} u_0 \left(\mathcal{O}(M^0) + \mathcal{O}(M)\right) \leq 1, \qquad \forall \sigma \in \mathcal{E}_{\text{int}}. \tag{100b}$$

Relations (100) indicate that, in the low Mach regime, the CFL constraints are primarily governed by the material velocity.

Let us now focus on the behavior of the linear system (19b)-(19c) associated with the acoustic steps (19) and (57) respectively for the barotropic system and the full Euler system in the regime $M \ll 1$ when it is reduced to the system (128) in the sole pressure variable. Using non-dimensional quantities, we have

$$\sum_{\sigma\in\mathcal{E}(K)} |\sigma| \left(\frac{\lambda_\sigma^n}{\rho_{D_\sigma}^n} + \mathcal{O}(M)\right) \widetilde{\pi}_K - \sum_{\substack{\sigma\in\mathcal{E}(K)\\ \sigma=K|L}} |\sigma| \left(\frac{\lambda_\sigma^n}{\rho_{D_\sigma}^n} + \mathcal{O}(M)\right) \widetilde{\pi}_L = \mathcal{O}(M^2), \tag{101}$$

so that the coefficient associated with the system do not become singular in the limit $M \to 0$. Finally, let us examine the well-posedness of the linear system (19b)-(19c) in the low Mach number regime. Supposing that $(\widetilde{\pi}_K)_{K\in\mathcal{M}}$ and $(\widetilde{\mathbf{u}}_\sigma)_{\sigma\in\mathcal{E}_{int}}$ lie in the kernel of the matrix associated with (19b)-(19c), they verify the non-dimensional expression of (142), that is to say

$$\frac{1}{M^2} \sum_{K\in\mathcal{M}} |K| \frac{\rho_K^n}{\delta t} \frac{(\widetilde{\pi}_K)^2}{2(a_K^n)^2} + \sum_{\sigma\in\mathcal{E}_{int}} \frac{|D_\sigma|}{\delta t} \rho_{D_\sigma}^n \frac{|\widetilde{\mathbf{u}}_\sigma|^2}{2} \leq 0. \tag{102}$$

Therefore $\widetilde{\pi}_K = 0$ for all $K \in \mathcal{M}$ and $\widetilde{\mathbf{u}}_\sigma = \mathbf{0}$ for all $\sigma \in \mathcal{E}_{int}$, so that the system remains well-posed in the limite $M \to 0$.

8 Full Euler system: preservation of constant pressure-velocity profiles

The following analysis is carried out for a specific equation of state (EOS). This choice is not merely a convenience: for a general EOS, the property in question does not appear to follow from the available estimates, and we suspect that it may not hold without additional structure. Whether the result can be extended to arbitrary EOS remains an open question; the present contribution thus focuses on a class of EOS for which the proof is non trivial but tractable. In this section we make the hypotheses that the fluid is governed by the Full Euler equations (46) and that the equation of state is a Stiffened Gas so that the pressure law is

$$(\tau, e) \mapsto p^{\text{EOS}}(\tau, e) = (\gamma - 1)e/\tau - \gamma p^\infty, \tag{103}$$

where $\gamma > 1$ and $p^\infty > 0$ are constant. Let us mention that the stiffened gas equation of state is a natural and widely adopted choice in the literature: its simplicity facilitates comparisons with existing works, while its versatility allows it to model both gaseous and liquid phases (see *e.g.* [3, 54, 70, 34]).

We consider a problem where the pressure and the velocity are uniform at instant t^n:

$$\mathbf{u}_\sigma^n = \overline{\mathbf{u}} \quad \text{for all } \sigma \in \mathcal{E}_{int}, \qquad\qquad p_K^n = \overline{p} \quad \text{for all } K \in \mathcal{M}. \tag{104}$$

Let us first consider the update of the discrete variables by the acoustic step (53): (16a) reads here $u_{K,\sigma}^n = \overline{\mathbf{u}}_\sigma \cdot \mathbf{n}_{K,\sigma}$ and thus $\sum_{\mathcal{E}(K)} u_{K,\sigma}^n = 0$. Then, it is straightfoward to see that $\widetilde{\pi}_K = \overline{p}$ is a solution of (128). Relation (20c) yields $(\boldsymbol{\nabla}\widetilde{\pi})_{D_\sigma} = \mathbf{0}$ which implies by (57b) that $\widetilde{\mathbf{u}}_\sigma = \overline{\mathbf{u}}_\sigma$, for $\sigma \in \mathcal{E}_{int}$. Definition (20b) gives $\widetilde{u}_{K,\sigma}^* = \overline{\mathbf{u}}_\sigma \cdot \mathbf{n}_{K,\sigma}$ so that by (20a), (32), (22) and (60) we get

$$(\boldsymbol{\nabla}\cdot\widetilde{\mathbf{u}})_K = 0, \quad \widetilde{S}_K = 0 \quad \text{for all } K \in \mathcal{M}, \quad (\boldsymbol{\nabla}\cdot\widetilde{\mathbf{u}})_{D_\sigma} = 0, \quad \widetilde{R}_\sigma = 0 \quad \text{for all } \sigma \in \mathcal{E}_{int}. \tag{105}$$

Using (57a), (28c) and (57c) we obtain

$$\widetilde{\rho}_K = \rho_K^n, \qquad\qquad \widetilde{\rho}_{D_\sigma} = \rho_{D_\sigma}^n, \qquad\qquad \widetilde{e}_K = e_K^n. \tag{106}$$

We now turn to the transport step (63), thanks to (106) we have

$$\forall K \in \mathcal{M}, \qquad |K| \left(\rho_K^{n+1} - \rho_K^n\right) + \delta t \sum_{\sigma\in\mathcal{E}(K)} \widetilde{F}_{K,\sigma} = 0, \tag{107a}$$

$$\forall \sigma \in \mathcal{E}_{int}, \qquad |D_\sigma| \left(\rho_{D_\sigma}^{n+1}\mathbf{u}_\sigma^{n+1} - \rho_{D_\sigma}^n\overline{\mathbf{u}}_\sigma\right) + \delta t \sum_{\varepsilon\in\mathcal{E}(D_\sigma)} \widetilde{F}_{\sigma,\varepsilon}\overline{\mathbf{u}}_\sigma = \mathbf{0}, \tag{107b}$$

$$\forall K \in \mathcal{M}, \qquad |K| \left(\rho_K^{n+1}e_K^{n+1} - \rho_K^n e_K^n\right) + \delta t \sum_{\sigma\in\mathcal{E}(K)} \widetilde{F}_{K,\sigma}\widetilde{e}_\sigma = S_K^{n+1}, \tag{107c}$$

Using (107a) together with the definition of $\widetilde{F}_{\sigma,\varepsilon}$ in appendix A, we get that

$$\forall \sigma \in \mathcal{E}_{int}, \quad |D_\sigma| \left(\rho_{D_\sigma}^{n+1} - \rho_{D_\sigma}^n\right) + \delta t \sum_{\varepsilon\in\mathcal{E}(D_\sigma)} \widetilde{F}_{\sigma,\varepsilon} = 0. \tag{108}$$

Thanks to (107b) and (30), this yields that

$$\forall \sigma \in \mathcal{E}_{int}, \quad \mathbf{u}_\sigma^{n+1} = \overline{\mathbf{u}}_\sigma, \qquad\qquad \forall \sigma \in \mathcal{E}(D_\sigma), \quad \mathbf{u}_\varepsilon = \overline{\mathbf{u}}_\sigma. \tag{109}$$

Accouting for (64) this leads to

$$\forall K \in \mathcal{M}, \quad S_K^{n+1} = 0. \tag{110}$$

For all $K \in \mathcal{M}$, we have $\widetilde{\rho}_K\widetilde{e}_K = \rho_K^n e_K^n = (\overline{p} + \gamma p^\infty)/(\gamma - 1)$, so that applying (28a), (28c) and (62) gives here $\widetilde{F}_{K,\sigma}\widetilde{e}_\sigma = |\sigma|(\overline{p} + \gamma p^\infty)(\overline{\mathbf{u}}_\sigma \cdot \mathbf{n}_{K,\sigma})/(\gamma - 1)$. Consequently, the energy update (107c) now reads

$$|K|\frac{p_K^{n+1} + \gamma p^\infty}{\gamma - 1} - |K|\frac{\overline{p} + \gamma p^\infty}{\gamma - 1} + \delta t \sum_{\sigma\in\mathcal{E}(K)} \frac{\overline{p} + \gamma p^\infty}{\gamma - 1}|\sigma| \left(\overline{\mathbf{u}}_\sigma \cdot \mathbf{n}_{K,\sigma}\right) = 0, \tag{111}$$

which implies that $p_K^{n+1} = \overline{p}$ for all $K \in \mathcal{M}$. Finally, we can conclude that the scheme numerically preserves constant pressure and velocity profiles.

9 Numerical tests and results

In this section, we present a series of numerical tests and corresponding results for both the barotropic and full Euler systems. The objective is to compare the performance of the SLP IMEX scheme with the Staggered Reference (SRE) explicit scheme presented in [61], and further summarized in Appendix A. Two-dimensional simulations are carried out using both the MAC and RT discretizations, while one-dimensional tests are primarily performed using MAC. This choice is motivated by the fact that the RT discretization reduces to the MAC scheme in one space dimension.

9.1 Results for the barotropic Euler equations

For the barotropic tests, we choose the following perfect gas equation of state:

$$p^{\mathrm{EOS}}(\tau) \overset{\mathrm{def}}{=} K\tau^{-\gamma}, \tag{112}$$

which gives, according to (3), for the barotropic potential and the sound velocity, respectively:

$$e^{\mathrm{EOS}}(\tau) = \frac{K}{\gamma - 1}\tau^{-(\gamma-1)}, \quad c^{\mathrm{EOS}}(\tau) = \sqrt{\gamma\tau p^{\mathrm{EOS}}(\tau)}.$$

9.1.1 Shock tube test 1

We first consider a one-dimensional shock-tube test given in [16] with initial data corresponding to the test 1 (shock-shock). More precisely, we set intial conditions (15) as follow

$$\left(\rho_K^0(x), u_\sigma^0(x)\right)^T = \begin{cases} (\rho_L, u_L)^T & \text{if} \quad x < 0, \\ (\rho_R, u_R)^T & \text{if} \quad x > 0, \end{cases} \tag{113}$$

with left and right values given in Table 2.

Test 1: Shock - Shock		
Left state	$\rho_L = 1$	$u_L = 1$
Right state	$\rho_R = 2$	$u_R = 0.5$

Table 2: left and right values for the first shock tube test

The constants in the pressure law (112), are chosen as follow

$$\gamma = 1.6 \quad \text{and} \quad K = \frac{(\gamma-1)^2}{4\gamma}. \tag{114}$$

The computational domain is $x \in [-0.2, 0.8]$ and the final time is $t_f = 0.5$. The density and velocity profiles are shown in Figure 3, for both the **SLP IMEX** scheme (in red) and the **SRE EXPL** (in blue) with 300 cells and CFL $= 0.5$. The exact solution, plotted in black, consists of two shocks propagating to the right. Both schemes successfully reproduce the reference solution. However, the SLP IMEX scheme appears slightly more diffusive than the SRE Explicit scheme.

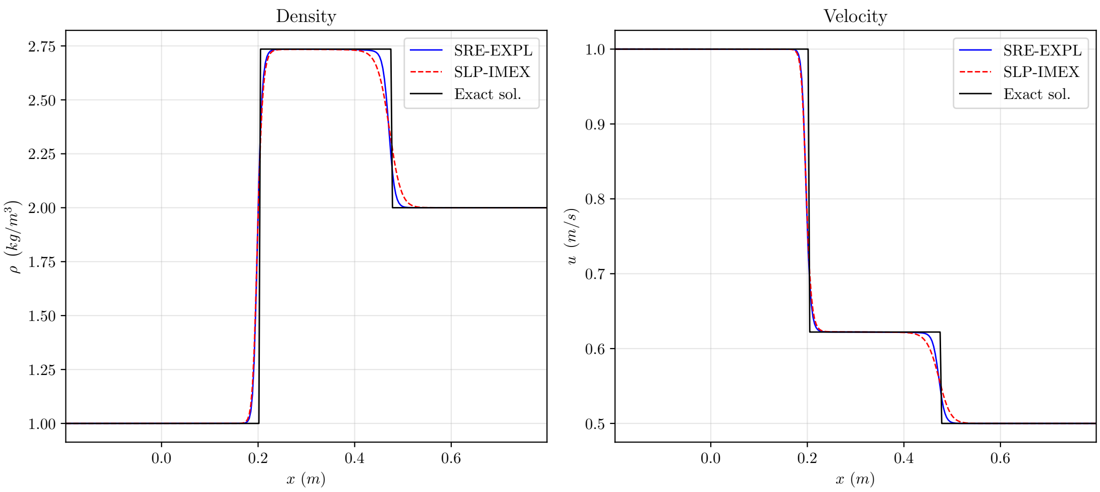

Figure 3: Shock tube test 1: comparison between the reference scheme and the SLP IMEX scheme

Figure 4 shows the L_1 norm of the error obtained with the SLP IMEX scheme. As expected when using a first-order upwind approach in the transport step, the results confirm that the overall scheme exhibits first-order accuracy.

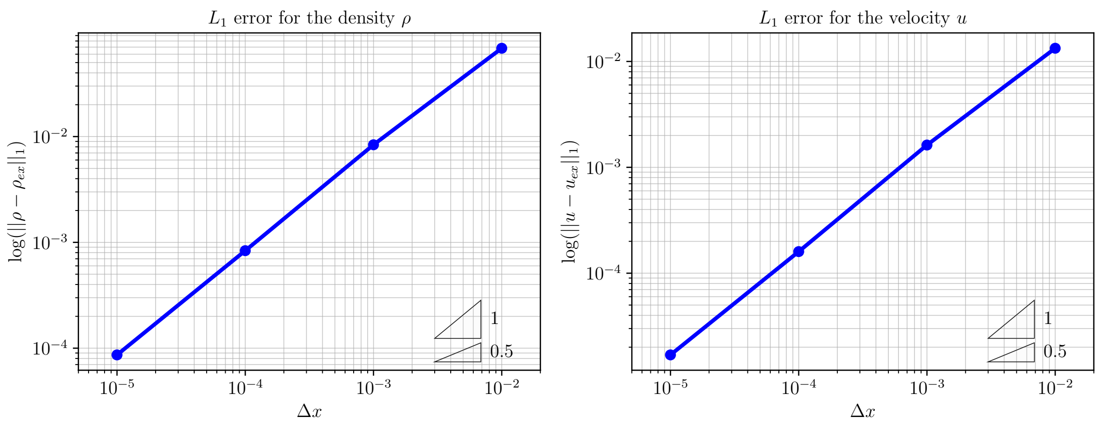

Figure 4: Shock tube test 1: L_1 norm of the error of the SLP-IMEX scheme with respect to the exact solution for density and velocity

9.1.2 Shock tube test 2

Following a procedure similar to that of [61], we repeat the previous shock tube test by subtracting a constant real value from both the left and right velocities. This constant is chosen such that the velocity in the intermediate state vanishes. The resulting values for the left and right states are given in Table 3.

Test 2: Shock - Shock		
Left state	$\rho_L = 1$	$u_L = 0.37785$
Right state	$\rho_R = 2$	$u_R = -0.12215$

Table 3: left and right values for the second shock tube test

As noted in [61], this test may be challenging for numerical schemes as it could lead to spurious oscillations resulting from a lack of numerical diffusion in the momentum equation. We observe that the SLP IMEX scheme successfully produces results free of numerical oscillations near the zero-velocity region, highlighting the effectiveness of the numerical diffusion inherent to the scheme. Let us mention that other strategies proposed in the literature in the framework of kinetic schemes [5, 42] are not affected by such oscillations. This robustness is mainly due to the second term on the right-hand side of the definition (20b) of $\widetilde{u}^{*}_{K,\sigma}$ which stabilizes the overall scheme when the velocity vanishes. It is worth noting that removing this term would also lead to the appearance of oscillations in the numerical solution.

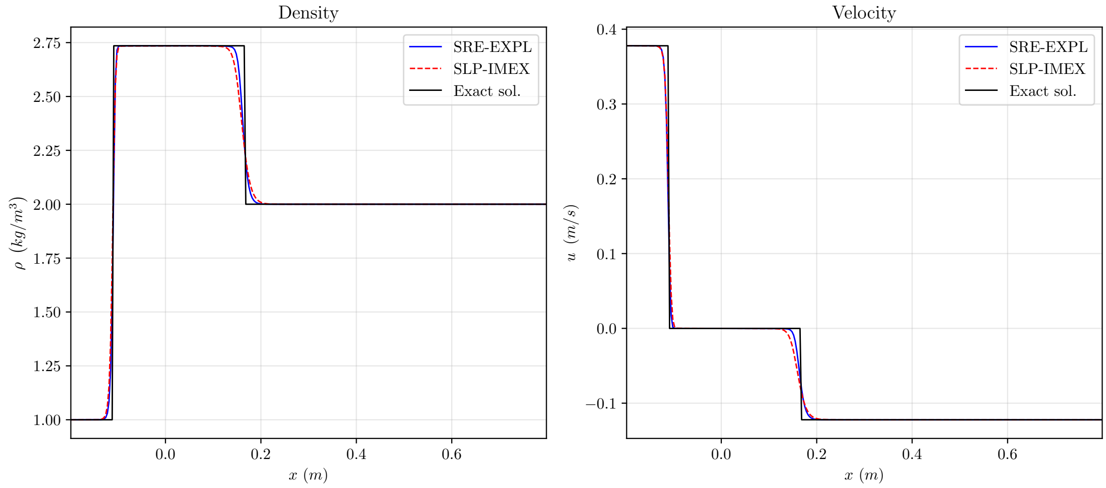

Figure 5: Shock tube test 2: comparison between the SRE explicit scheme with artificial viscosity in the momentum equation and the SLP IMEX scheme.

9.1.3 Low mach cylinder flow

This two-dimensional test was originally presented in [10]. The main objective is to assess the effectiveness and accuracy of the SLP IMEX scheme in the low-Mach-number regime. In this configuration, a low-Mach-number flow interacts with a cylinder of radius r_0. The domain Ω is an annulus defined by $(r, \theta) \in [r_0, r_1] \times [0, 2\pi[$, where (r, θ) are the polar coordinates and with $r_0 = 0.5$ and $r_1 = 5.5$. The initial data are uniform and set to,

$$\rho^0_K(\mathbf{x}) = \rho_0, \quad \mathbf{u}^0_\sigma(\mathbf{x}) = (u_0, 0)^T, \tag{115}$$

with $\rho_0 = 1$, $u_0 = c_0 M_\infty$ and $c_0 = c^{\mathrm{EOS}}(1/\rho_0)$. The term M_∞ denotes the Mach number at infinity. The exact solution at infinity is uniform and given by

$$\rho_\infty = 1, \quad \mathbf{u}_\infty = (u_0, 0)^T.$$

As in [10], wall boundary conditions are considered on the internal cylinder, whereas inlet or outlet conditions are considered on the external cylinder. For the equation of state (112), we set $K = 1$ and $\gamma = 2$. Both triangular and quadratic discretizations are tested and compared to a stationary reference solution. This solution, developed in power of the Mach number is provided in [10]. Accordingly, pressure fluctuations are expected to be of order M^2.

For the quadratic mesh, the discretization is performed using $n_r = 50$ in the radial direction and $n_\theta = 160$ in the orthoradial direction for a total of 8000 cells. The computation is stopped when the stationnary state is reached. In our simulation, the corresponding final time is $t_f = 500$. Isolines showing the pressure fluctations for the stationary solution at $M_\infty = 10^{-3}$ are illustrated in Figure 6.

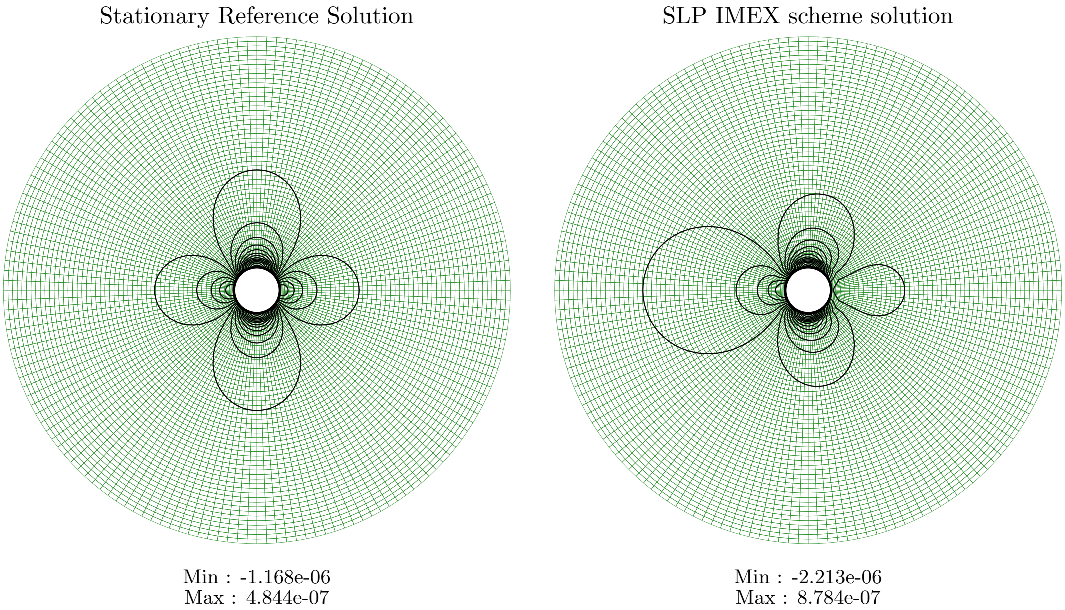

Figure 6: Low Mach Cylinder Flow using the SLP IMEX Euler scheme with RT discretization and a quadratic mesh. 20 isolines were plotted, representing the pressure fluctations $p - p_\infty$ at $M_\infty = 10^{-3}$.

The triangular discretization is performed using a mesh refinement near the center, resulting in a total of 6544 cells. Figure 7 shows the isolines for the pressure fluctations for the stationary solution at $M_\infty = 10^{-3}$ over this mesh.

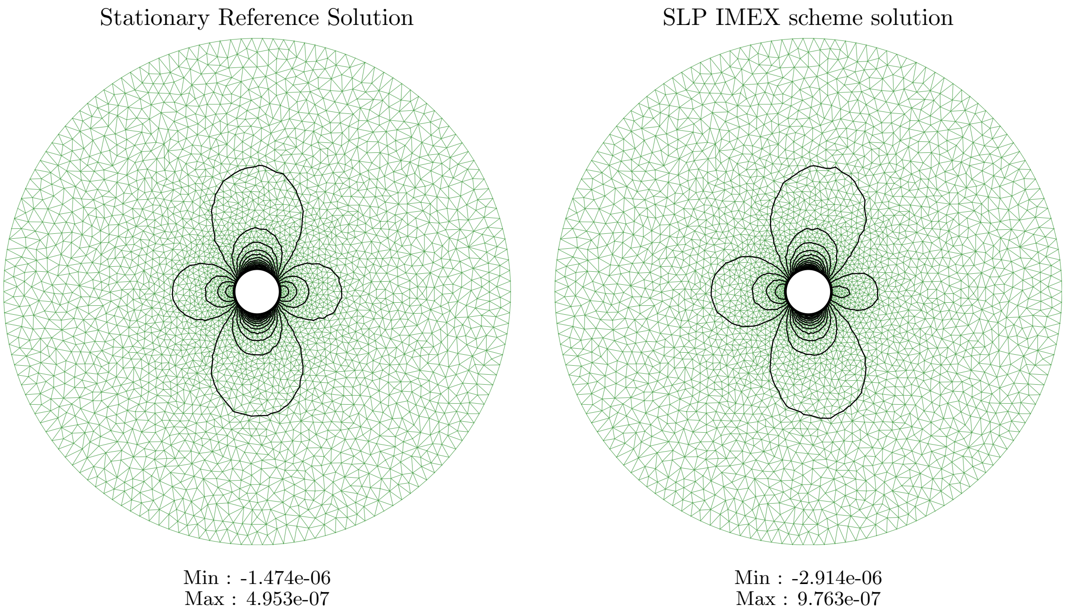

Figure 7: Low Mach Cylinder Flow using the SLP IMEX Euler scheme with RT discretization and a triangular mesh. 20 isolines were plotted, representing the pressure fluctations $p - p_\infty$ at $M_\infty = 10^{-3}$.

By examining the minimum and maximum values of the pressure fluctuations on both meshes, we observe that the SLP IMEX scheme successfully captures the low-Mach-number stationary flow, maintaining pressure variations consistent with the expected order of M_∞^2.

Furthermore, Figure 8 illustrates the variation of the density norm $\|\rho_h - \rho_\infty\|$ as a function of the Mach number $M_\infty \in \left[10^{-1}, 10^{-2}, 10^{-3}, 10^{-4}\right]$, where ρ_h refers to the stationary discrete density field. As expected for this type of staggered discretization scheme, the behavior of the discrete solution scales consistently with M_∞^2 both for quadrilateral and triangular meshes.

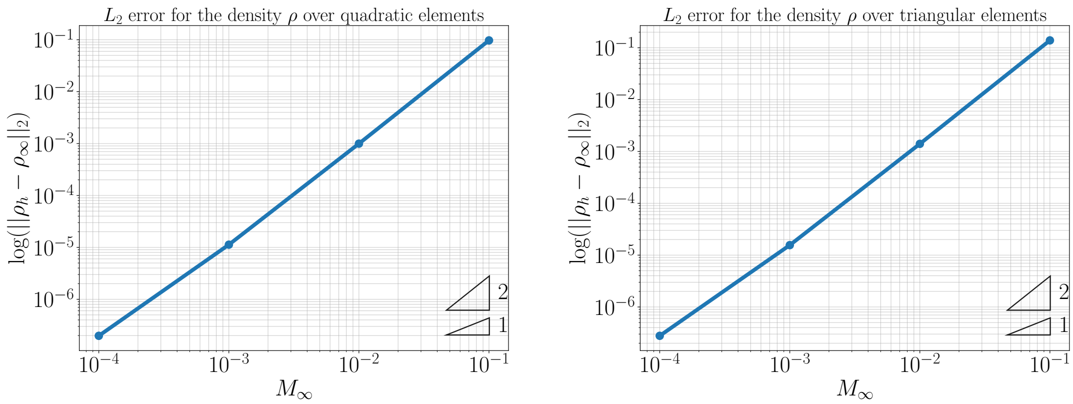

Figure 8: Low Mach Cylinder Flow: L_2 norm of the density error vs. Mach number $M_\infty \in \left[10^{-1}, 10^{-2}, 10^{-3}, 10^{-4}\right]$ for SLP-IMEX scheme for the quadrilateral (left) and the triangular (right) meshes.

9.2 Results for the full Euler equations

For the full Euler system, we choose the following ideal gas law

$$p^{\text{EOS}}(\tau, s) \stackrel{\text{def}}{=} (\gamma - 1)\frac{e^{\text{EOS}}(\tau, s)}{\tau}, \qquad e^{\text{EOS}}(\tau, s) \stackrel{\text{def}}{=} \tau^{1-\gamma}\exp(s) \tag{116}$$

which implies that the sound velocity writes:

$$c^{\text{EOS}}(\tau, s) = \sqrt{(\gamma - 1)\left(e - \tau\frac{\partial e}{\partial \tau}\right)}, \quad e = e^{\text{EOS}}(\tau, s).$$

In the following tests, we set $\gamma = 1.4$.

9.2.1 Toro test 5

This test corresponds to test number 5 in the Toro's book [91] and consists of a left rarefaction wave, a contact discontinuity and a strong right shock. The initial conditions are given according Table 4.

Toro test 5: Rarefaction - Contact - Shock

Left state	$\rho_L = 1$	$u_L = -19.5975$	$p_L = 1000$
Right state	$\rho_R = 1$	$u_R = -19.5975$	$p_R = 0.01$

Table 4: left and right values for the Toro test 5

In Figure 9, the density and velocity profiles are shown for both the **SLP IMEX** scheme (in red) and the **SRE EXPL** (in blue) with 1000 cells and $CFL = 0.5$. Both schemes successfully reproduce the reference solution, although the **SLP IMEX** scheme appears slightly more diffusive. Such behavior is expected, as the implicit treatment of acoustic waves in the IMEX scheme stabilizes the solution and permits larger time steps, at the cost of increased numerical diffusion. It is also worth noting that the internal energy exhibits an overshoot in the vicinity of the contact discontinuity. This behavior is reminiscent of the wall-heating phenomenon [78, 81], in which kinetic energy is not fully and consistently converted into internal energy at stagnation points, leading to a localized spurious heating.

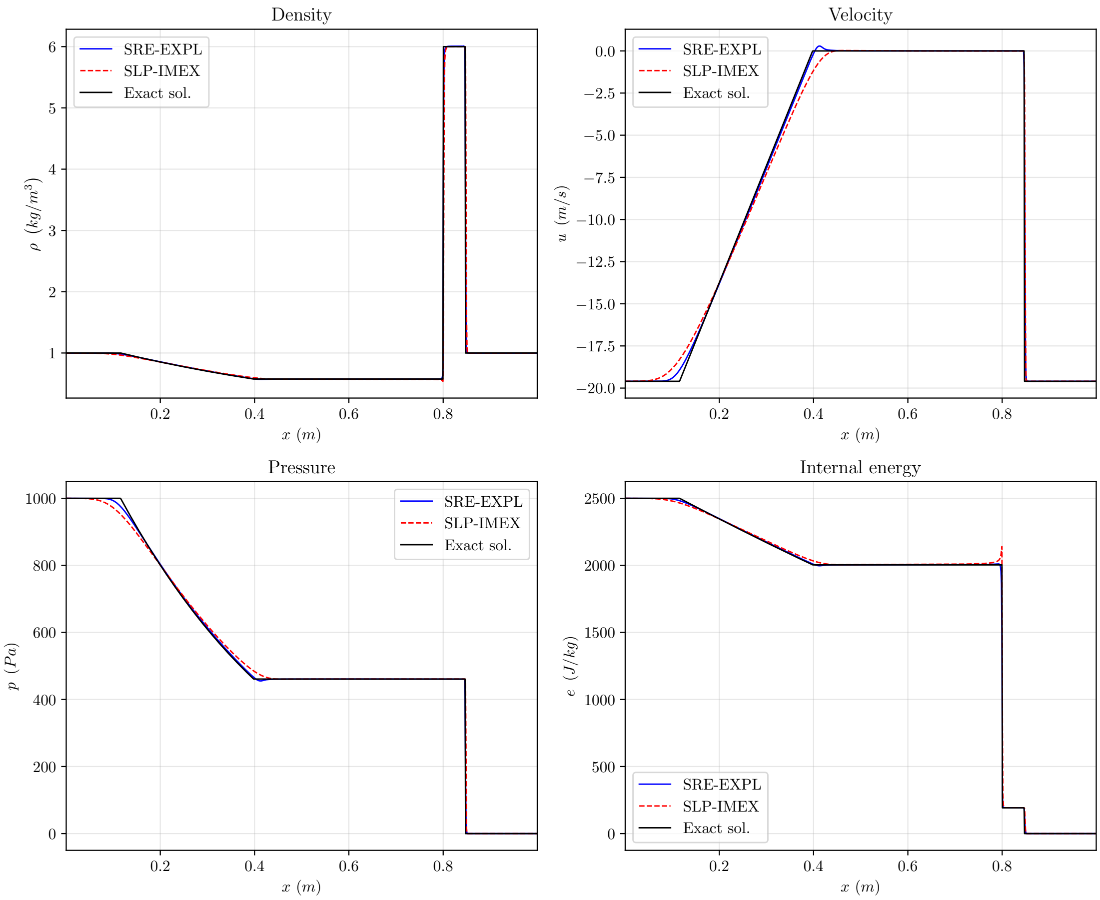

Figure 9: Toro Tests 5: comparison between the SRE explicit scheme and the SLP IMEX scheme for 1000 cells and CFL = 0.5

Figure 10 shows the L_1 norm of the error obtained with the SLP IMEX scheme. As for the first shock tube test, we obtain the first order accuracy for the overall scheme.

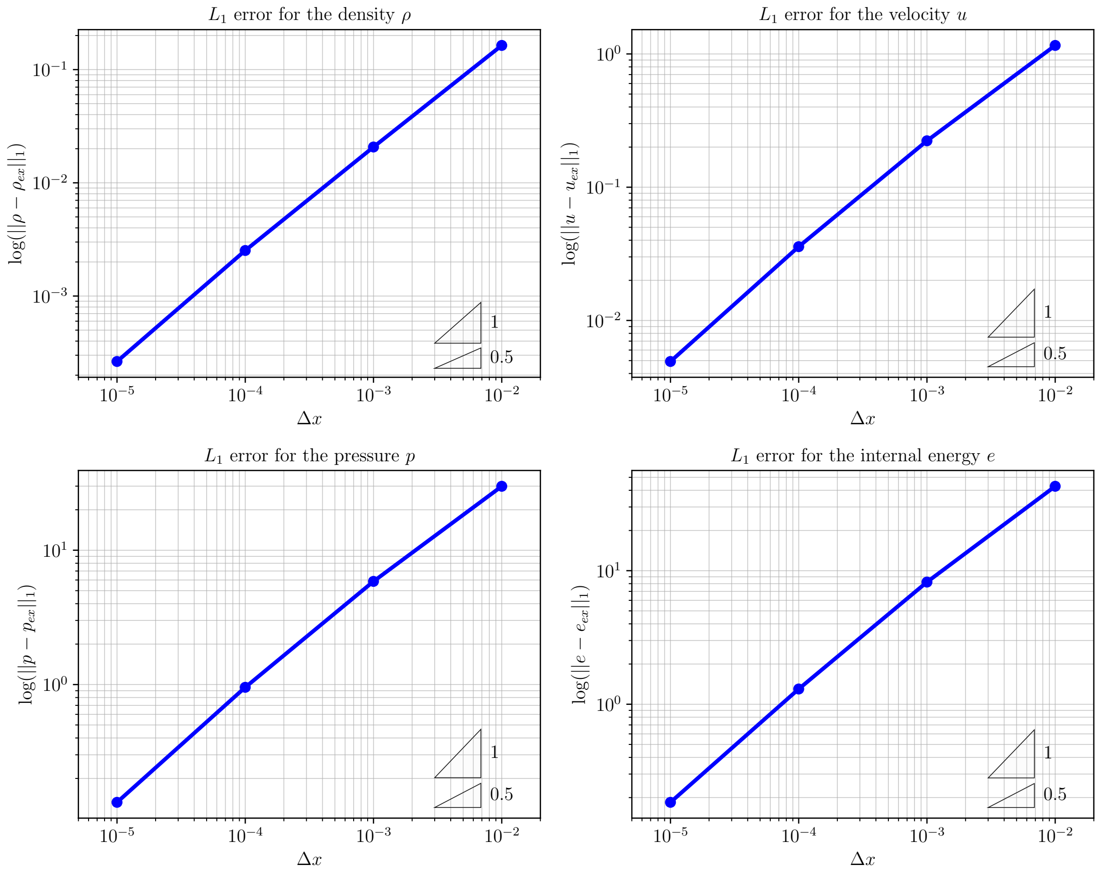

Figure 10: Toro Tests 5: L_1 norm of the error with respect to the exact solution for density, velocity, pressure and internal energy.

9.2.2 Gresho vortex

The Gresho vortex problem, as studied in [75], describes a steady rotating vortex with a time-independent velocity field. The angular velocity $u^0_{\sigma,\phi}(r)$ depends solely on the radial coordinate, with the centrifugal force balanced by the pressure gradient. Let (r, θ) denote the polar coordinates; the initial conditions are defined as follows:

$$u^0_{\sigma,\phi}(r) = \begin{cases} 5r, & \text{if } 0 \leq r < 0.2, \\ 2 - 5r, & \text{if } 0.2 \leq r < 0.4, \\ 0, & \text{if } 0.4 \leq r, \end{cases} \tag{117a}$$

$$p^0(r) = \begin{cases} 5 + \frac{25}{5} r^2, & \text{if } 0 \leq r < 0.2, \\ 9 - 4\ln 0.2 + \frac{25}{5} r^2 - 20r + 4\ln r, & \text{if } 0.2 \leq r < 0.4, \\ 3 + 4\ln 2, & \text{if } 0.4 \leq r, \end{cases} \tag{117b}$$

as for the radial velocity and the density, they are 0 and 1, respectively.

A regular mesh consisting of 200×200 cells was used that discretizes the computational domain $\Omega = [-0.5, 0.5]^2$. The simulation was performed using periodic boundary conditions. This test assesses the accuracy of the numerical scheme in the low Mach number regime. In the present case, the Mach number is set to $M = 10^{-2}$. The final time is $t_f = 0.5$, $CFL = 0.5$ and we use the MAC discretization Figure 11 presents the spatial distribution of scaled density and pressure fluctuations, as well as the velocity magnitude and the Mach number. As expected in this regime, scaled pressure fluctuations are of order M^{-2}. Moreover, the vortex remains stationary, as showed by the velocity magnitude and Mach number. Moreover, for the sake of comparing the resulting admissible time steps, we also performed the simulation using the SRE scheme: the SRE scheme, which is constrained by the sound speed, used an average time step of 6.25×10^{-6} s, while the SLP-IMEX scheme, limited only by the material velocity, allowed for a larger average time step of 9.3×10^{-4} s.

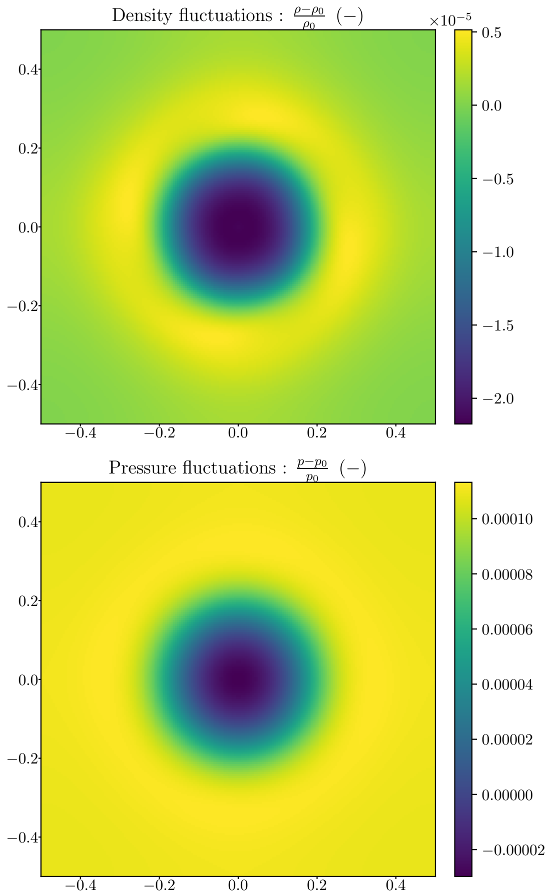

Figure 11: Gresho vortex: results for SLP IMEX scheme at $t_f = 0.5$ and Mach $= 10^{-2}$. The mesh resolution is 200×200 cells and CFL $= 0.5$. The test was performed using the MAC discretization.

9.2.3 A 2D Riemann problem test

We consider the two-dimensional Riemann problem of case 3 studied in [75] and performed using a 400×400-cell regular mesh. We use the homogeneous Neumann boundary conditions for the whole boundary of the domain. Results for both the SLP IMEX and the SRE schemes are displayed in Figure 13 and consists of four shocks that separates the four regions associated to the initial conditions. The MAC discretization was used for this test and a diffusive term is added to the momentum equation in the SRE scheme to enhance numerical stability, as already discussed in the second test (see section 9.1.2).

Both schemes are in good agreement with the results of [75], accurately capturing the four shocks that separate the four regions.

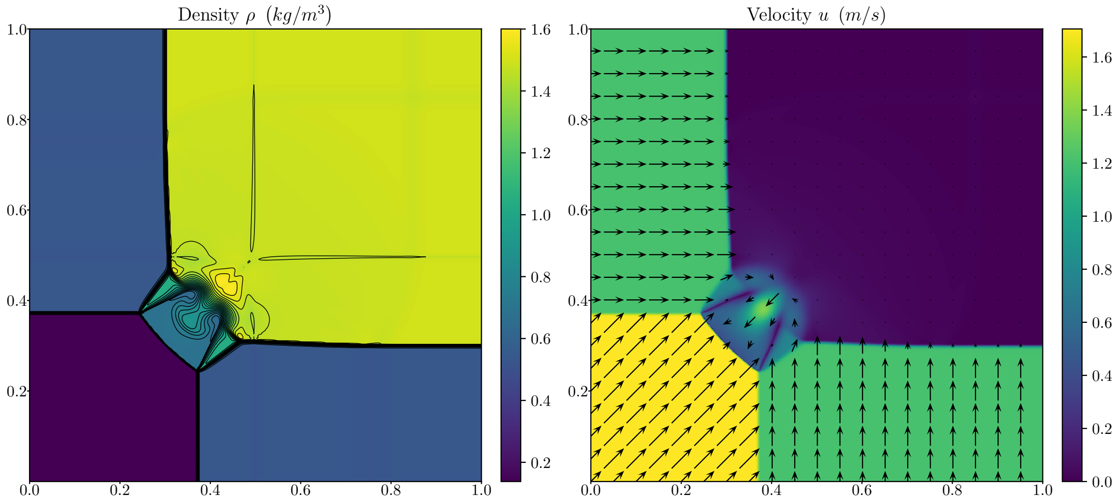

Figure 12: Riemann 2D Test 3 using the SRE scheme for a mesh resolution of 400 × 400 and CFL = 0.5

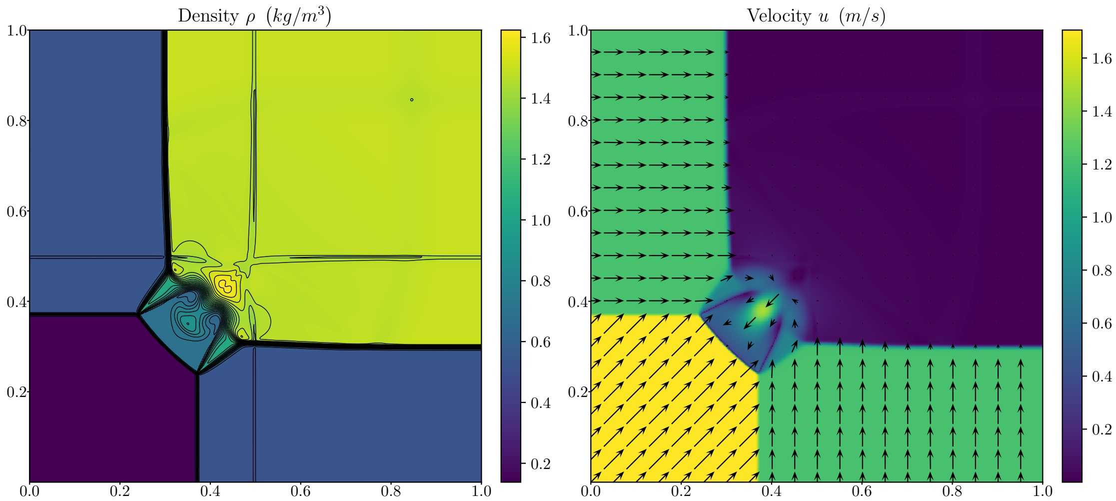

Figure 13: Riemann 2D Test 3 using the SLP IMEX Full Euler scheme for a mesh resolution of 400 × 400 and CFL = 0.5. The test was performed using the MAC discretization.

9.2.4 Kelvin-Helmholtz instability

The Kelvin-Helmholtz (KH) instability test is a fundamental hydrodynamic simulation used to study shear-driven turbulence and mixing in stratified fluids. This test is particularly relevant in astrophysical and engineering contexts, where shear layers arise naturally in a variety of systems, such as protoplanetary disks, stellar atmospheres, and interstellar gas clouds. The KH instability occurs when two parallel layers of fluid move with different velocities, creating velocity shear at their interface. The instability is driven by the kinetic energy of the shearing motion, with steeper shear velocity gradients generally enhancing the tendency for instabilities to emerge. If a perturbation is introduced, it amplifies due to vorticity generation, leading to the characteristic roll-up of the shear interface, forming billow-like structures. We refer the reader to [71, 84] for an extensive analysis of this test.

A square domain $-0.5 \leq x \leq 0.5, -0.5 \leq y \leq 0.5$ is considered with periodic boundary conditions [86]. Each layer moves with a different velocity and the density contrast between the layers can vary depending on the test setup, influencing the growth rate and morphology of the instability. We set, with $U_0 = 0.5$,

$$u^0_{\sigma,x}(x, y) = \begin{cases} -U_0, & |y| > 0.25, \\ +U_0, & |y| \leq 0.25, \end{cases} \qquad \rho^0_K = \begin{cases} 1, & |y| > 0.25, \\ 2, & |y| \leq 0.25. \end{cases} \tag{118}$$

The pressure is equal to 2.5 over the entire domain. Following the approach in [84], and adapting it to our computational domain, we introduce a sinusoidal perturbation in the y-component of the velocity to initiate the instability at each interface:

$$u^0_{\sigma,y}(x, y) = \begin{cases} \omega_0 \sin(n\pi x) \exp\left(-\dfrac{(y + 0.25)^2}{2\eta^2}\right), & \text{if } y < 0, \\ \\ \omega_0 \sin(n\pi x) \exp\left(-\dfrac{(y - 0.25)^2}{2\eta^2}\right), & \text{if } y > 0. \end{cases} \tag{119}$$

The parameters n, ω_0 and η are chosen accordingly [84]:

$$n = 4, \quad \omega_0 = 0.1, \quad \eta = 0.05.$$

Figure 14 shows the resulting initial condition for the velocity associated with (118) and (119).

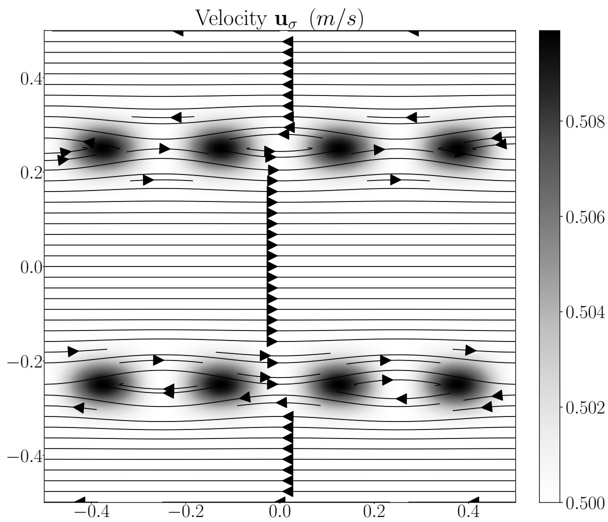

Figure 14: Velocity at initial time for the Kelvin-Helmholtz test.

To evaluate the impact of mesh geometry and discretization methods, we employed two distinct computational grids: a regular Cartesian grid of 1280×1280 cells and an unstructured triangular mesh. The latter was generated by subdividing a 640×640 quadrangle grid into $1,638,400$ triangles, where each quadrangle was split into four equal triangles by connecting its vertices to its center.

This construction ensures a perfectly consistent initialization across both meshes and the exact same number of cells, enabling a direct comparison of the different discretizations. Consequently, three distinct simulations were conducted with the following discretizations and meshes:

- **MAC** discretization on the 1280×1280 Cartesian grid;
- **RT/CR** discretization on a 1280×1280 Cartesian grid;
- **RT/CR** discretization on the $1,638,400$ $(= 640 \times 640 \times 4)$ triangular mesh.

The density profile evolution at $t = \{0.5\,\mathrm{s}, 1\,\mathrm{s}, 1.5\,\mathrm{s}, 2\,\mathrm{s}\}$ is represented in Figure 15.

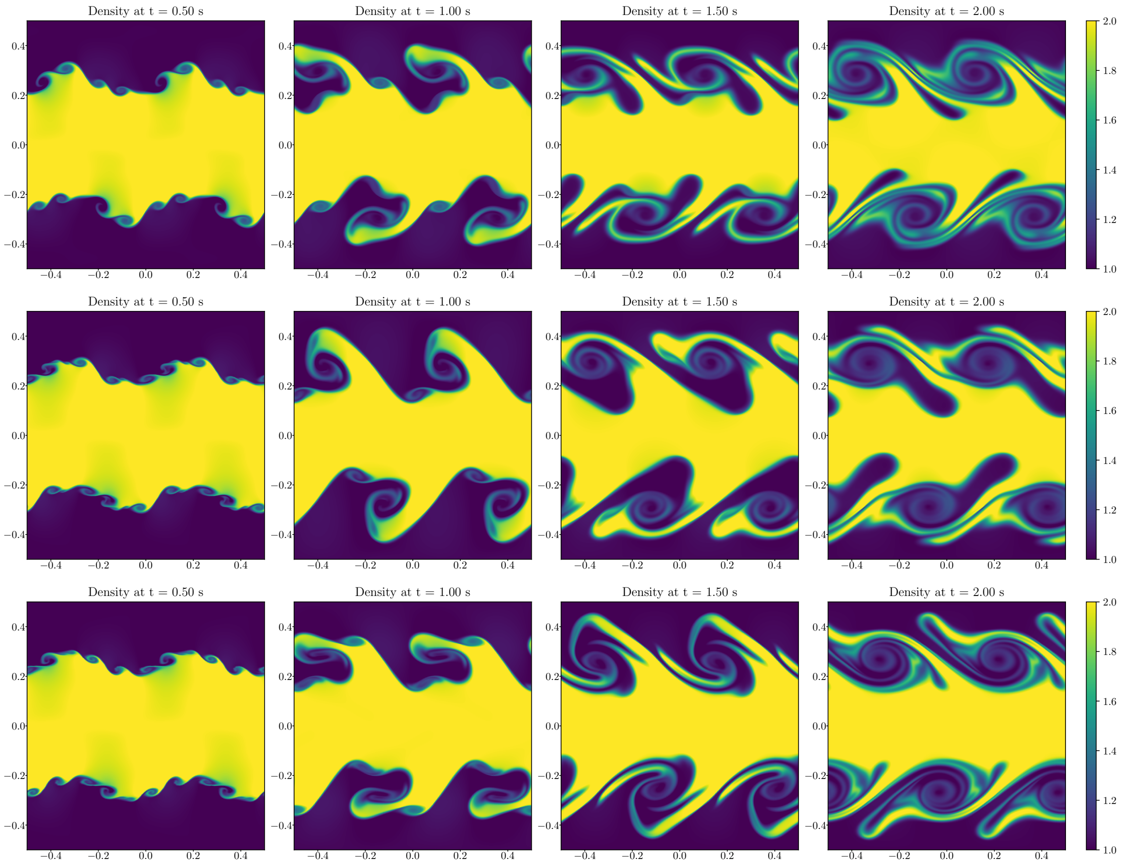

Figure 15: Density profile evolution for a Kelvin-Helmholtz test using the SLP IMEX scheme with periodic boundary conditions and velocity perturbations for the $y-$component around the interface. The mesh resolution is 1280×1280 **quadrangles** (first row) using **MAC** discretization, 1280×1280 **quadrangles** (second row) using **RT/CR** discretization, 640×640 quadrangles divided in 4 **triangles** (third row) using **RT/CR** discretization and a CFL $= 0.5$.

As the simulation progresses, small perturbations at the velocity shear layer grow due to the differential motion of the fluid layers. Nonlinear effects enhance the development of vortices, which roll up into coherent structures, forming a series of Kelvin-Helmholtz billows. These billows eventually interact, merging into larger turbulent structures. The vortices obtained with the RT/CR discretization (second and third rows) are noticeably wider and more diffused than those produced by the MAC discretization (first row), for which the vortical structures remain sharper and better developed. Furthermore, as shown in the last row, the RT/CR discretization on the triangular mesh appears to capture vorticity effects more accurately than on the quadrilateral mesh shown in the second row, even though the three simulations use exactly the same number of cells. While the results demonstrate good agreement with [84], our SLP IMEX scheme exhibits slightly higher numerical diffusion. This is attributed to the upwind approach used in its transport step, a method inherently limited to at best first-order accuracy. Investigating a higher-order approach, such as a MUSCL-type reconstruction for the transport step, could greatly reduce the numerical dissipation. This type of approach for a staggered finite volume scheme has been proposed in [39] within a framework similar to ours as well as in [76] in the framework of the kinetic schemes of [5].

9.2.5 Rayleigh-Taylor instability

The Rayleigh-Taylor instability is a physical phenomenon that occurs when a denser fluid is placed on top of a lighter one in a gravitational field [68, 75]. This test assesses the ability of a numerical method to resolve the development of an instability at the interface of two fluid layers with different densities, driven by gravity. In order to evaluate the performance of the proposed scheme in the low-Mach-number regime in the presence of a source term, as well as its robustness when physical diffusion is introduced through the Navier–Stokes viscous stress tensor, we consider the same configuration as in the last section of [28]. The computational domain is a rectangle defined by $-0.25 \leq x \leq 0.25$ and $-0.75 \leq y \leq 0.75$, with periodic boundary conditions imposed at $|x| = 0.25$ and reflecting (slip) wall boundary conditions at $|y| = 0.75$. The initial conditions are defined as follows:

$$\begin{cases} \rho_K^0(x,y) = 2\chi_{\{y>0\}} + 1\chi_{\{y<0\}}, \\ u_{\sigma,x}^0(x,y) = 0, \\ u_{\sigma,y}^0(x,y) = 0.25a\,(1+\cos(4\pi x))\,(1+\cos(3\pi y))\,\chi_{\{y<1/6\}}, \\ p_K^0(x,y) = p_0 + \rho_K^0(x,y) g y, \quad p_0 = 2.5, \end{cases}$$

with $g = -0.1$, $p_0 = 2.5$ and $a = 0.01$. Gravity is introduced as a source term in the momentum equation. The implementation of the gravity source term follows the approach proposed in [11]: considering an external force $\mathbf{f} = \rho \mathbf{g}$ in the momentum balance equation, we write, for any internal face $\sigma \in \mathcal{E}_{\text{int}}$,

$$\frac{|D_\sigma|}{\delta t}\left(\rho_{D_\sigma}^{n+1}\mathbf{u}_\sigma^{n+1} - \rho_{D_\sigma}^{n}\mathbf{u}_\sigma^{n}\right) + \sum_{\varepsilon\in\mathcal{E}(D_\sigma)} \widetilde{F}_{\sigma,\varepsilon}\,\widetilde{\mathbf{u}}_\varepsilon + |D_\sigma|\left(\boldsymbol{\nabla}\widetilde{\pi}\right)_\sigma = |D_\sigma|\mathbf{f}_{D_\sigma}^{n+1},$$

where $\mathbf{f}_{D_\sigma}^{n+1}$ denotes the discrete gravitational force. Within the SLP–IMEX scheme, it is approximated as

$$\mathbf{f}_{D_\sigma}^{n+1} = \frac{|\sigma|}{|D_\sigma|}\left[\rho_{D_\sigma}^{n+1}\,\mathbf{g}\cdot(\mathbf{x}_K - \mathbf{x}_L)\right]\mathbf{n}_{K,\sigma},$$

where $\mathbf{x}_K,\ \mathbf{x}_L$ denote respectively the center of mass of the neighboring cells K and L.

For the Navier–Stokes viscous stress tensor τ, we adopt the same parameters as in [28], namely a constant dynamic viscosity $\mu = 10^{-4}$ and a bulk viscosity $\lambda = -\frac{2}{3}\mu$. For constant viscosity coefficients, the divergence of the viscous stress tensor reduces to

$$\boldsymbol{\nabla}\cdot\tau = \mu\left(\nabla^2\mathbf{u} + \frac{1}{3}\boldsymbol{\nabla}\left(\boldsymbol{\nabla}\cdot\mathbf{u}\right)\right).$$

As we used for this test the MAC discretization, both differential operators are discretized following the approach described in [44]. The Rayleigh–Taylor instability is triggered by the initial velocity perturbation $u_{\sigma,y}^0(x,y)$.

The test was performed on three regular Cartesian grids using the MAC discretization with CFL $= 0.5$: 300×900, 600×1800 and 900×2700 quadrilateral cells.

In order to verify that the instability develops in the low-Mach-number regime, we first examine the velocity field and the corresponding Mach number at time $T = 10\,\mathrm{s}$ for the simulation including the viscous stress tensor, as shown in Figure 16. As illustrated in the right panel, the Mach number remains bounded between 0 and 0.15 at this time, thereby confirming that the flow evolves in the low-Mach-number regime.

The time evolution of the density field at $t = \{3\,\mathrm{s}, 6\,\mathrm{s}, 8\,\mathrm{s}, 10\,\mathrm{s}, 12\,\mathrm{s}, 13\,\mathrm{s}\}$ is shown for the compressible Euler system without physical diffusion in Figure 17, and with the Navier–Stokes viscous stress tensor in Figure 18. The evolution of the Rayleigh–Taylor instability proceeds through three characteristic stages. It first exhibits a linear growth phase, during which small perturbations at the interface grow exponentially. This is followed by a nonlinear regime, where the interface deforms and develops the characteristic mushroom-shaped structures as the heavier fluid penetrates the lighter one, while the lighter fluid rises in buoyant plumes.

When physical diffusion is included through the Navier–Stokes viscous stress tensor, the numerical solution recovers the classical Rayleigh–Taylor instability structure, in close agreement with the reference results reported in [28]. In contrast, in the inviscid Euler case, the solution exhibits a stronger dependence on the numerical discretization, as the absence of physical diffusion allows numerical dissipation and dispersion to play a dominant role in the instability development. Indeed, without the stabilizing effect of the viscosity, the modes that can be excited by the instability are no longer controlled by the physical setting but by discretization parameters like the choice of the mesh or the numerical scheme. Indeed, in the absence of any stabilizing effect, the solution behavior becomes highly sensitive to the discretization choices like the numerical scheme or the mesh, as demonstrated by the significant discrepancy between our results and those reported in [28].

These results demonstrate that the proposed scheme remains robust and accurate in the low-Mach-number regime, while consistently handling the combined effects of gravitational source terms and Navier–Stokes viscous stresses in the simulation of buoyancy-driven instabilities.

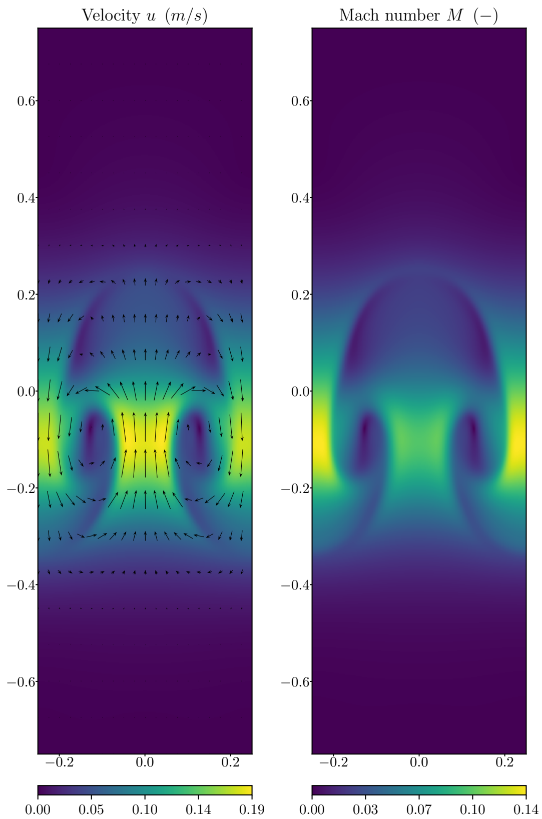

Figure 16: Velocity and Mach number for the Rayleigh–Taylor instability with Navier–Stokes viscosity on a 300×900 Cartesian grid at $T = 10\,\mathrm{s}$.

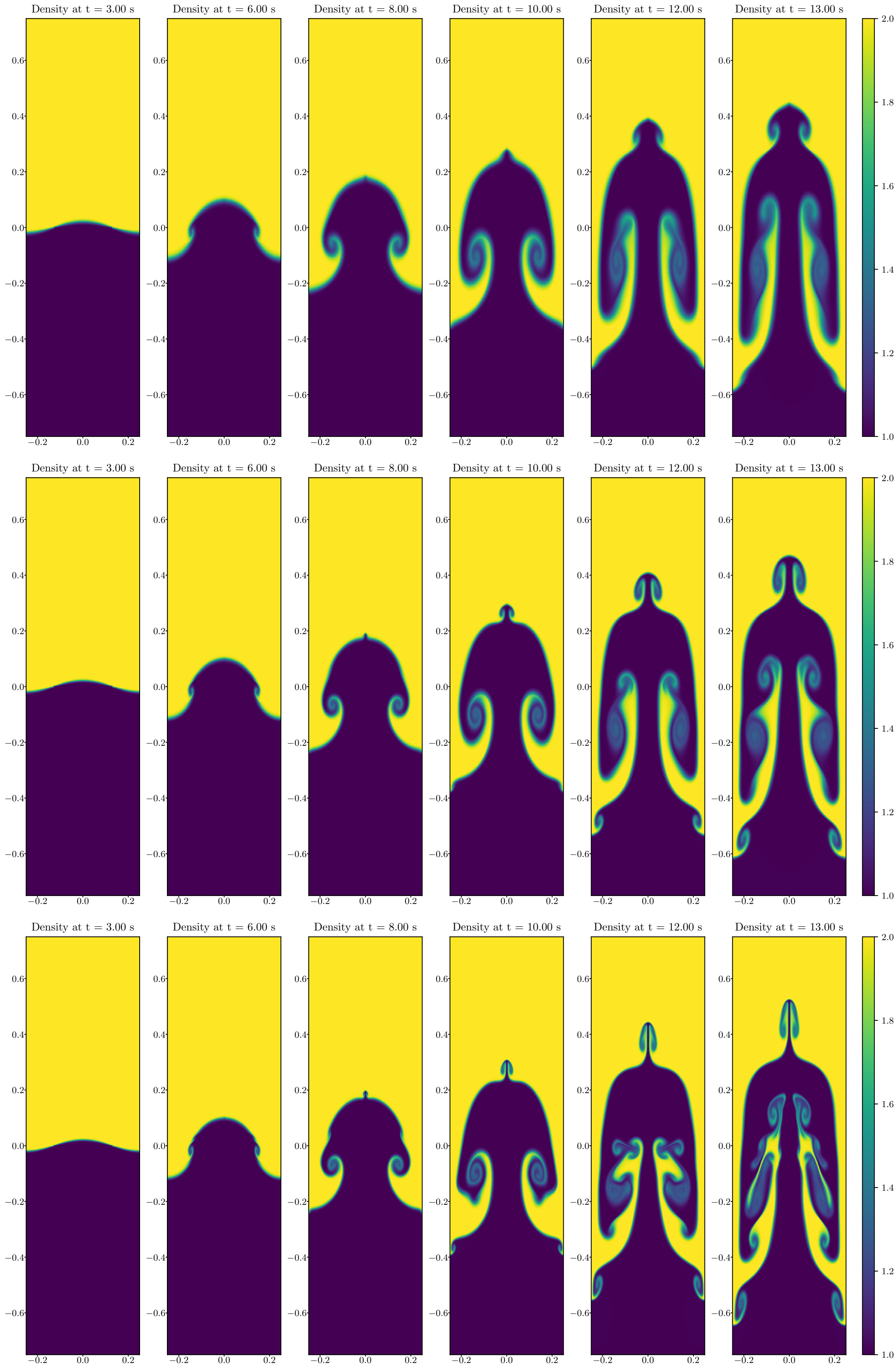

Figure 17: Density profile evolution for a Rayleigh Taylor test for Euler system using the SLP IMEX Full Euler scheme with periodic and wall boundary conditions and velocity perturbations using the **MAC** discretization for a mesh resolution of 300×900 (first row), 600×1800 (second row), 900×2700 (third row), and a CFL $= 0.5$.

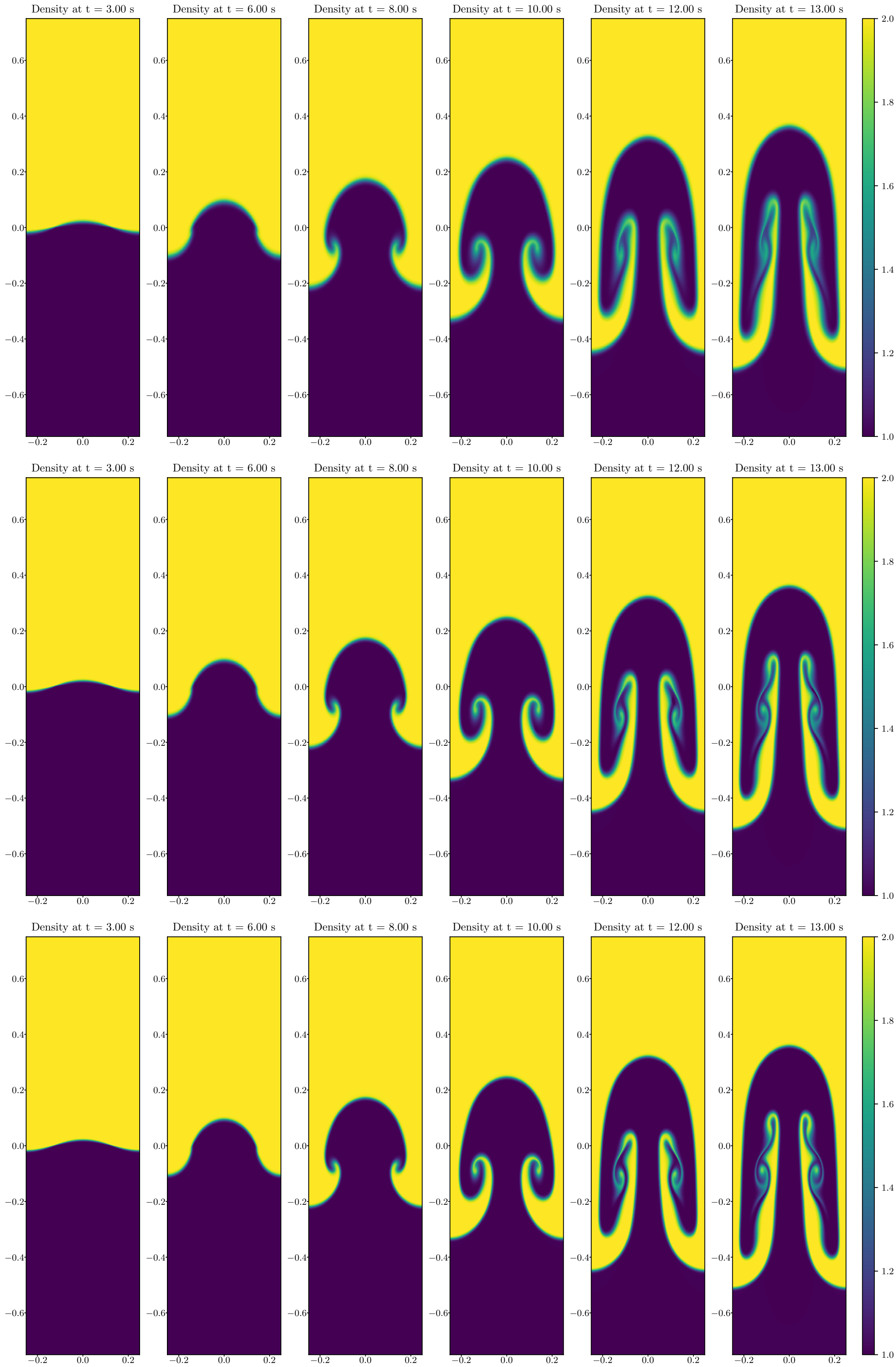

Figure 18: Density profile evolution for a Rayleigh Taylor test with NS viscous stress tensor using the SLP IMEX Full Euler scheme with periodic and wall boundary conditions and velocity perturbations using the **MAC** discretization for a mesh resolution of 300×900 (first row), 600×1800 (second row), 900×2700 (third row), and a CFL $= 0.5$.

9.2.6 Sedov blast wave problem

We consider the same benchmark as in [43], namely the simulation of the classical Sedov blast wave on the quarter plane. As a consequence, the total energy typically prescribed for the Sedov test, $E_0 = 1$, is divided by four in the present setting. The initial conditions are given by

$$\begin{cases} \rho_K^0(x, y) = 1, \\ \mathbf{u}_\sigma^0(x, y) = \mathbf{0}, \\ p_K^0(x, y) = (\gamma - 1)\, \dfrac{E_0}{4\,|V_\varepsilon|}\, \chi_{\left\{\sqrt{x^2+y^2}<r_\varepsilon\right\}} + 10^{-14}, \end{cases}$$

where

$$|V_\varepsilon| = \sum_{K\in\mathcal{M}_\varepsilon} |K|, \qquad \mathcal{M}_\varepsilon = \left\{ K \in \mathcal{M} \mid \mathbf{x}_K = (x_K, y_K)^T,\ \sqrt{x_K^2 + y_K^2} < r_\varepsilon \right\},$$

and $r_\varepsilon = 3/\sqrt{N_K}$ is a small distance which defines the region where the total energy is initially concentrated (N_K being the total number of cells of the mesh). The three computational meshes, composed respectively of 164 954, 295 052 and 661 536 triangular cells, were generated using Gmsh [40].

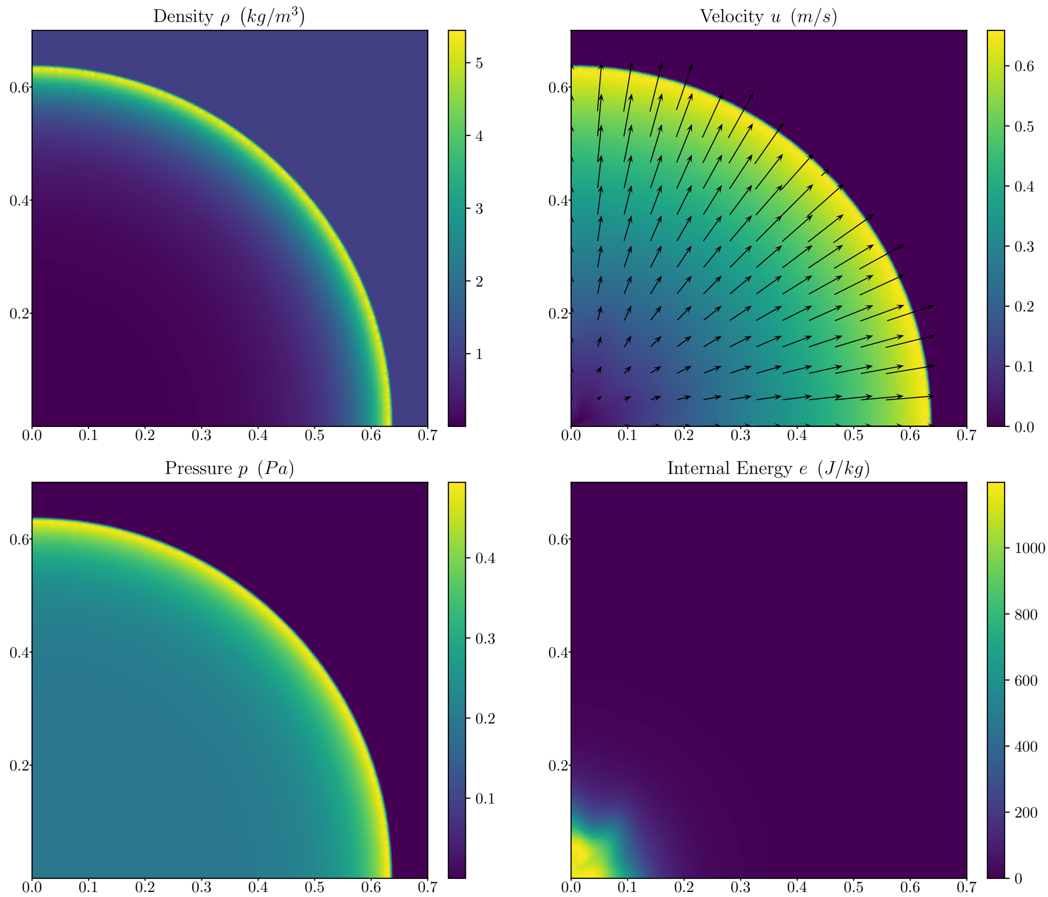

Figure 19: Results at time $T_{max} = 0.4$ for the 2D Sedov blast wave problem on the finest triangular grid (661536 cells) using the SLP IMEX Full Euler scheme and a CFL = 0.5.

The results at time $T_{max} = 0.4$ are shown on Figure 19 respectively for the density ρ, velocity $\mathbf{u}$, pressure p and the internal energy e on the finest mesh of 661 536 triangles. The RT/CR discretization is used with a CFL number of 0.5. The numerical solution is in good agreement with the reference results reported in [43], and correctly reproduces the self-similar radial expansion of the blast wave while preserving the symmetry of the solution. Finally, the same simulation was repeated with the SRE scheme to compare the time steps for this unsteady test. The average time step for SRE (constrained by the sound speed) was 3.410×10^{-6} s, whereas the SLP-IMEX scheme (limited only by the material velocity) admitted a significantly larger average time step of 1.771×10^{-4} s.

Figure 20 presents radial cutlines of the numerical solution at times $T_{\max} = 0.2$ and $T_{\max} = 0.4$ for the three considered meshes, together with the exact solution, following the procedure of [43]. The shock location and the overall profiles are accurately captured, with a clear improvement as the mesh is refined, and the propagation speed of the blast wave is correctly predicted.

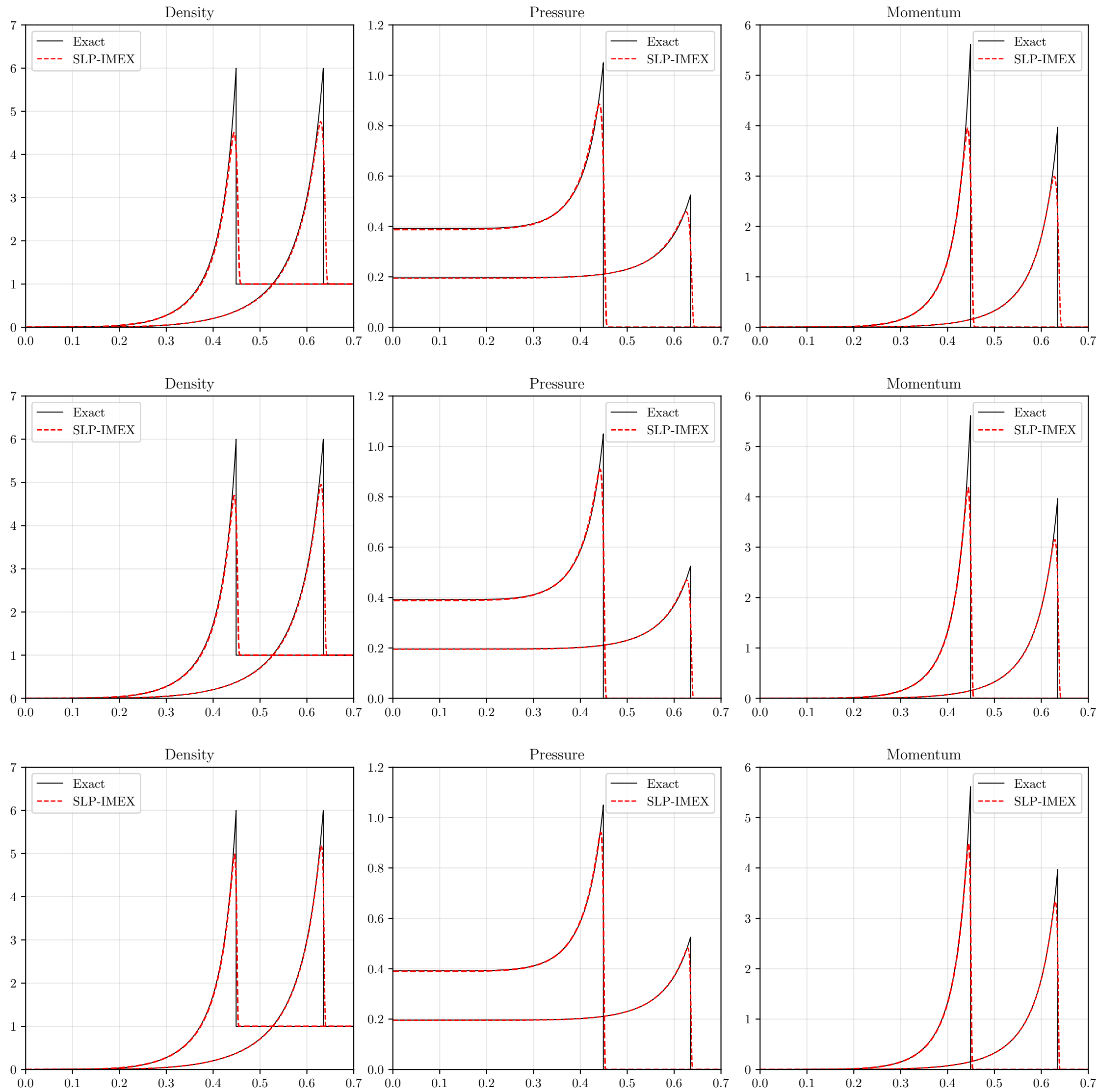

Figure 20: Sedov blast wave problem : comparison of the the SLP IMEX discrete radial profiles with the exact solution at times $T_{max} = 0.2$ and $T_{max} = 0.4$ for the different meshes and CFL = 0.5. From top to bottom : 164954, 295052 and 661536 triangular cells.

10 Conclusion

In this work we introduced a staggered finite volume scheme for the discretization of compressible fluid flows on unstructured meshes, addressing both barotropic and full Euler systems with general equations of state. The methodology combines a Lagrange-Projection like operator splitting technique, which decouples acoustic and transport effects, with a relaxation approach. The acoustic subsystem is treated implicitly via a well-posed linear system for the pressure, while transport is handled explicitly. This yields an IMEX scheme independent of the sound velocity constraint. For the full Euler system, the internal energy is used as main variable and its update features a corrective term that ensures consistency with weak solutions.

The scheme demonstrates stability for large time steps, with CFL conditions dependent only on material velocity. It guarantees conservation of mass and momentum, as well as positivity of mass and internal energy for the full Euler system under the CFL condition. For the stiffened gas equation of state, constant pressure and velocity profiles are preserved. Entropy properties include a global mathematical inequality for the barotropic system and a local inequality for the full Euler system. The scheme satisfies a global total energy conservation for the full Euler system and is also consistent with a local total energy conservation on the dual mesh. Numerical experiments, performed on 1D and 2D meshes, span a broad range of Mach numbers. Convergence is verified on refined 1D meshes, confirming the scheme's accuracy and robustness across diverse flow regimes.

Sequel developments include high-order extensions and approximations for other multi-material flows.

References

[1] G. Ansanay-Alex, F. Babik, J. C. Latché, and D. Vola. An L2-stable approximation of the Navier–Stokes convection operator for low-order non-conforming finite elements. In: *International Journal for Numerical Methods in Fluids* 66.5 (2011), pp. 555–580. DOI: 10.1002/fld.2270.

[2] R. Baraille, G. Bourdin, F. Dubois, and A.-Y. Le Roux. Une version à pas fractionnaires du schéma de Godunov pour l'hydrodynamique. (A splitted version of the Godunov scheme for hydrodynamic models). French. In: *C. R. Acad. Sci., Paris, Sér. I* 314.2 (1992), pp. 147–152.

[3] T. Barberon and P. Helluy. Finite volume simulation of cavitating flows. In: *Computers & Fluids* 34.7 (Aug. 2005), pp. 832–858. DOI: 10.1016/j.compfluid.2004.06.004.

[4] W. Barsukow. Truly Multi-Dimensional All-Speed Schemes for the Euler Equations on Cartesian Grids. In: *Journal of Computational Physics* 435 (June 2021), p. 110216. DOI: 10.1016/j.jcp.2021.110216.

[5] F. Berthelin, T. Goudon, and S. Minjeaud. Kinetic schemes on staggered grids for barotropic Euler models: entropy-stability analysis. In: *Mathematics of Computation* 84.295 (2015), pp. 2221–2262. DOI: 10.1090/S0025-5718-2015-02957-3.

[6] C. Berthon. Inégalités d'entropie pour un schéma de relaxation. In: *Comptes Rendus Mathematique* 340.1 (2005), pp. 63–68. DOI: 10.1016/j.crma.2004.10.008.

[7] F. Bouchut. *Nonlinear stability of finite volume methods for hyperbolic conservation laws.* Birkhäuser Basel, 2004. DOI: 10.1007/b93802.

[8] F. Bouchut, C. Chalons, and S. Guisset. An entropy satisfying two-speed relaxation system for the barotropic Euler equations: application to the numerical approximation of low Mach number flows. In: *Numerische Mathematik* 145.1 (Mar. 2020), pp. 35–76. DOI: 10.1007/s00211-020-01111-5.

[9] F. Bouchut, E. Franck, and L. Navoret. A Low Cost Semi-implicit Low-Mach Relaxation Scheme for the Full Euler Equations. In: *Journal of Scientific Computing* 83.1 (Apr. 2020), p. 24. DOI: 10.1007/s10915-020-01206-z.

[10] P. Bruel, S. Delmas, J. Jung, and V. Perrier. A low Mach correction able to deal with low Mach acoustics. In: *Journal of Computational Physics* 378 (Feb. 2019), pp. 723–759. DOI: 10.1016/j.jcp.2018.11.020.

[11] A. Brunel. Schémas à mailles décalées sur maillages généraux pour les écoulements incompressibles et compressibles. PhD thesis. Aix-Marseille Université, 2022. URL: http://www.theses.fr/2022AIXM0632/document.

[12] A. Brunel, R. Herbin, and J.-C. Latché. A MUSCL-like finite volumes approximation of the momentum convection operator for low-order nonconforming face-centred discretizations. In: *ArXiv* abs/2301.02087 (2023).

[13] A. Brunel, R. Herbin, and J.-C. Latché. A staggered scheme for the compressible Euler equations on general 3D meshes. In: *Journal of Scientific Computing* 100.30 (2024). DOI: 10.1007/s10915-024-02560-y.

[14] C. Chalons and F. Coquel. Navier-Stokes equations with several independent pressure laws and explicit predictor-corrector schemes. In: *Numerische Mathematik* 101.3 (Sept. 2005), pp. 451–478. DOI: 10.1007/s00211-005-0612-7.

[15] C. Chalons, M. Girardin, and S. Kokh. An all-regime Lagrange-Projection like scheme for the gas dynamics equations on unstructured meshes. In: *Communications in Computational Physics* 20.1 (2016), pp. 188–233. DOI: 10.4208/cicp.260614.061115a.

[16] C. Chalons and J.-F. Coulombel. Relaxation approximation of the Euler equations. In: *Journal of Mathematical Analysis and Applications* 348.2 (Dec. 2008), pp. 872–893. DOI: 10.1016/j.jmaa.2008.07.034.

[17] C. Chalons, M. Girardin, and S. Kokh. An all-regime Lagrange-Projection like scheme for 2D homogeneous models for two-phase flows on unstructured meshes. In: *Journal of Computational Physics* 335 (2017), pp. 885–904. DOI: 10.1016/j.jcp.2017.01.017.

[18] C. Chalons, M. Girardin, and S. Kokh. Large Time Step and Asymptotic Preserving Numerical Schemes for the Gas Dynamics Equations with Source Terms. In: *SIAM Journal on Scientific Computing* 35.6 (2013), pp. A2874–A2902. DOI: 10.1137/130908671.

[19] C. Chalons, P. Kestener, S. Kokh, and M. Stauffert. A large time-step and well-balanced Lagrange-Projection type scheme for the shallow-water equations. In: *Communications in Mathematical Sciences* 15.3 (Apr. 2017), pp. 765–788. DOI: 10.4310/CMS.2017.v15.n3.a9.

[20] A. J. Chorin. Numerical solution of the Navier-Stokes equations. In: *Mathematics of Computation* 22.104 (1968), pp. 745–762. DOI: 10.1090/s0025-5718-1968-0242392-2.

[21] P. G. Ciarlet. Basic error estimates for elliptic problems. In: *Handbook of Numerical Analysis, Volume II* 2 (1991), pp. 17–351. DOI: 10.1016/S1570-8659(05)80039-0.

[22] P. Colella and K. Pao. A projection method for low speed flows. In: *Journal of Computational Physics* 149.2 (Mar. 1999), pp. 245–269. DOI: 10.1006/jcph.1998.6152.

[23] P. Colella and P. R. Woodward. The Piecewise Parabolic Method (PPM) for Gas-Dynamical Simulations. In: *Journal of Computational Physics* 54.1 (Apr. 1984), pp. 174–201. DOI: 10.1016/0021-9991(84)90143-8.

[24] F. Coquel, E. Godlewski, and N. Seguin. Relaxation of Fluid Systems. In: *Mathematical Models and Methods in Applied Sciences* 22.08 (May 2012), p. 1250014. DOI: 10.1142/s0218202512500145.

[25] F. Coquel, Q. L. Nguyen, M. Postel, and Q. H. Tran. Entropy-satisfying relaxation method with large time-steps for Euler IBVPs. In: *Mathematics of Computation* 79.271 (Feb. 2010), pp. 1493–1533. DOI: 10.1090/S0025-5718-10-02339-2.

[26] F. Cordier, P. Degond, and A. Kumbaro. An Asymptotic-Preserving All-Speed Scheme for the Euler and Navier–Stokes Equations. In: *Journal of Computational Physics* 231.17 (July 2012), pp. 5685–5704. DOI: 10.1016/j.jcp.2012.04.025.

[27] M. Crouzeix and P.-A. Raviart. Conforming and nonconforming finite element methods for solving the stationary Stokes equations I. In: *R.A.I.R.O.* 7.R3 (1973), pp. 33–75. DOI: 10.1051/m2an/197307R300331.

[28] G. Dakin, B. Després, and S. Jaouen. High-order staggered schemes for compressible hydrodynamics. Weak consistency and numerical validation. In: *Journal of Computational Physics* 376 (Jan. 2019), pp. 339–364. DOI: 10.1016/j.jcp.2018.09.046.

[29] G. Dakin and H. Jourdren. High-order accurate Lagrange-remap hydrodynamic schemes on staggered Cartesian grids. In: *Comptes Rendus Mathématique* 354.2 (Feb. 2016), pp. 211–217. DOI: 10.1016/j.crma.2015.11.008.

[30] S. Dellacherie. Analysis of Godunov type schemes applied to the compressible Euler system at low Mach number. In: *Journal of Computational Physics* 229.4 (2010), pp. 978–1016. DOI: 10.1016/j.jcp.2009.09.044.

[31] S. Dellacherie, J. Jung, P. Omnes, and P.-A. Raviart. Construction of modified Godunov-type schemes accurate at any Mach number for the compressible Euler system. In: *Mathematical Models and Methods in Applied Sciences* 26.13 (Dec. 2016), pp. 2525–2615. DOI: 10.1142/s0218202516500603.

[32] B. Després. *Numerical Methods for Eulerian and Lagrangian Conservation Laws*. Frontiers in Mathematics. Cham: Springer International Publishing, 2017. DOI: 10.1007/978-3-319-50355-4.

[33] G. Dimarco, R. Loubère, and M.-H. Vignal. Study of a new asymptotic preserving scheme for the Euler system in the low mach number limit. In: *SIAM Journal on Scientific Computing* 39.5 (2017), pp. A2099–A2128.

[34] G. Faccanoni, B. Grec, and Y. Penel. A homogeneous relaxation low mach number model. In: *ESAIM: Mathematical Modelling and Numerical Analysis* 55.4 (2021), pp. 1569–1598. DOI: 10.1051/m2an/2021032.

[35] G. Gallice, A. Chan, R. Loubère, and P.-H. Maire. Entropy Stable and Positivity Preserving Godunov-type Schemes for Multidimensional Hyperbolic Systems on Unstructured Grid. In: *Journal of Computational Physics* 468 (Nov. 2022), p. 111493. DOI: 10.1016/j.jcp.2022.111493.

[36] T. Gallouët, L. Gastaldo, R. Herbin, and J.-C. Latché. An unconditionally stable pressure correction scheme for the compressible barotropic Navier-Stokes equations. In: *ESAIM: Mathematical Modelling and Numerical Analysis* 42.2 (Mar. 2008), pp. 303–331. DOI: 10.1051/m2an:2008005.

[37] L. Gastaldo, R. Herbin, W. Kheriji, C. Lapuerta, and J.-C. Latché. Staggered discretizations, pressure correction schemes and all speed barotropic flows. In: *Finite Volumes for Complex Applications VI Problems & Perspectives*. Berlin, Heidelberg: Springer Berlin Heidelberg, 2011, pp. 839–855. DOI: 10.1007/978-3-642-20671-9_86.

[38] L. Gastaldo, R. Herbin, and J.-C. Latché. An unconditionally stable finite element-finite volume pressure correction scheme for the drift-flux model. In: *ESAIM: Mathematical Modelling and Numerical Analysis* 44.2 (Jan. 2010), pp. 251–287. DOI: 10.1051/m2an/2010002.

[39] L. Gastaldo, R. Herbin, J.-C. Latché, and N. Therme. A MUSCL-type segregated – explicit staggered scheme for the Euler equations. In: *Computers & Fluids* 175 (Oct. 2018), pp. 91–110. DOI: 10.1016/j.compfluid.2018.06.013.

[40] C. Geuzaine and J.-F. Remacle. Gmsh: a three-dimensional finite element mesh generator with built-in pre- and post-processing facilities. In: *International Journal for Numerical Methods in Engineering* 79.11 (2009), pp. 1309–1331. DOI: https://doi.org/10.1002/nme.2579.

[41] E. Godlewski and P.-A. Raviart. *Numerical approximation of hyperbolic systems of conservation laws*. Springer New York, 2021. DOI: 10.1007/978-1-0716-1344-3.

[42] T. Goudon, J. Llobell, and S. Minjeaud. A staggered scheme for the Euler equations. In: *Springer Proceedings in Mathematics & Statistics*. Springer International Publishing, 2017, pp. 91–99. DOI: 10.1007/978-3-319-57394-6_10.

[43] T. Goudon, J. Llobell, and S. Minjeaud. An explicit finite volume scheme on staggered grids for the Euler equations: Unstructured meshes, stability analysis, and energy conservation. In: *International Journal for Numerical Methods in Fluids* 94.1 (2022), pp. 76–119. DOI: https://doi.org/10.1002/fld.5048.

[44] D. Grapsas, R. Herbin, W. Kheriji, and J.-C. Latché. An unconditionally stable staggered pressure correction scheme for the compressible Navier-Stokes equations. en. In: *The SMAI Journal of computational mathematics* 2 (2016), pp. 51–97. DOI: 10.5802/smai-jcm.9.

[45] G. Guennebaud, B. Jacob, et al. *Eigen: C++ template library for linear algebra*. Accessed: 2025-05-28. Eigen Project. URL: http://eigen.tuxfamily.org.

[46] J. Guermond, P. Minev, and J. Shen. An overview of projection methods for incompressible flows. In: *Computer Methods in Applied Mechanics and Engineering* 195.44–47 (Sept. 2006), pp. 6011–6045. DOI: 10.1016/j.cma.2005.10.010.

[47] H. Guillard and A. Murrone. On the behavior of upwind schemes in the low Mach number limit: II. Godunov type schemes. In: *Computers & Fluids* 33.4 (May 2004), pp. 655–675. DOI: 10.1016/j.compfluid.2003.07.001.

[48] H. Guillard and C. Viozat. On the behaviour of upwind schemes in the low Mach number limit. en. In: *Computers & Fluids* 28.1 (Jan. 1999), pp. 63–86. DOI: 10.1016/S0045-7930(98)00017-6.

[49] J. Haack, S. Jin, and J.-G. Liu. An All-Speed Asymptotic-Preserving Method for the Isentropic Euler and Navier-Stokes Equations. In: *Communications in Computational Physics* 12.4 (Oct. 2012), pp. 955–980. DOI: 10.4208/cicp.250910.131011a.

[50] A. E. Halabi, P. Fernier, T. Galie, S. Kokh, and K. Saleh. Study of a numerical scheme with transport-acoustic operator splitting on a staggered mesh. In: *Finite Volumes for Complex Applications X—Volume 2, Hyperbolic and Related Problems*. Ed. by E. Franck, J. Fuhrmann, V. Michel-Dansac, and L. Navoret. Springer Nature Switzerland, 2023, pp. 121–129. DOI: 10.1007/978-3-031-40860-1_13.

[51] F. H. Harlow and A. A. Amsden. A numerical fluid dynamics calculation method for all flow speeds. In: *Journal of Computational Physics* 8.2 (1971), pp. 197–213. DOI: 10.1016/0021-9991(71)90002-7.

[52] F. H. Harlow and A. A. Amsden. Numerical Calculation of Almost Incompressible Flow. In: *Journal of Computational Physics* 3.1 (Aug. 1968), pp. 80–93. DOI: 10.1016/0021-9991(68)90007-7.

[53] F. H. Harlow and J. E. Welch. Numerical calculation of time-dependent viscous incompressible flow of fluid with free surface. In: *The Physics of Fluids* 8.12 (Dec. 1965), pp. 2182–2189. DOI: 10.1063/1.1761178.

[54] P. Helluy and N. Seguin. Relaxation models of phase transition flows. In: *ESAIM: Mathematical Modelling and Numerical Analysis* 40.2 (Mar. 2006), pp. 331–352. DOI: 10.1051/m2an:2006015.

[55] R. Herbin, W. Kheriji, and J.-C. Latché. On some implicit and semi-implicit staggered schemes for the shallow water and Euler equations. In: *ESAIM: Mathematical Modelling and Numerical Analysis* 48.6 (Oct. 2014), pp. 1807–1857. DOI: 10.1051/m2an/2014021.

[56] R. Herbin, W. Kheriji, and J.-C. Latché. Staggered schemes for all speed flows. In: *ESAIM: Proceedings* 35 (Mar. 2012), pp. 122–150. DOI: 10.1051/proc/201235008.

[57] R. Herbin, J.-C. Latché, S. Minjeaud, and N. Therme. Conservativity and weak consistency of a class of staggered finite volume methods for the Euler equations. In: *Mathematics of Computation* 90.329 (Dec. 2020), pp. 1155–1177. DOI: 10.1090/mcom/3575.

[58] R. Herbin, J.-C. Latché, and T. Nguyen. Explicit staggered schemes for the compressible Euler equations. In: *ESAIM: Proc.* 40 (2013), pp. 83–102. DOI: 10.1051/proc/201340006.

[59] R. Herbin, W. Kheriji, and J.-C. Latché. Staggered schemes for all speed flows. In: *ESAIM: Proceedings*. Congrès National de Mathématiques Appliquées et Industrielles 35 (2011), pp. 122–150. DOI: 10.1051/proc/201235008.

[60] R. Herbin, J.-C. Latché, and K. Saleh. Low Mach number limit of some staggered schemes for compressible barotropic flows. In: *Mathematics of Computation* 90.329 (2021), pp. 1039–1087.

[61] R. Herbin, J.-C. Latché, and T. T. Nguyen. Consistent segregated staggered schemes with explicit steps for the isentropic and full Euler equations. In: *ESAIM: Mathematical Modelling and Numerical Analysis* 52.3 (2018), pp. 893–944. DOI: 10.1051/m2an/2017055.

[62] R. Herbin and J.-C. Latché. Kinetic energy control in the MAC discretization of the compressible Navier-Stokes equations. In: *International Journal On Finite Volumes* 7.41 (2010).

[63] J. Hu, S. Jin, and Q. Li. Asymptotic-Preserving Schemes for Multiscale Hyperbolic and Kinetic Equations. In: *Handbook of Numerical Methods for Hyperbolic Problems - Applied and Modern Issues*. Elsevier, 2017, pp. 103–129. DOI: 10.1016/bs.hna.2016.09.001.

[64] D. Iampietro, F. Daude, P. Galon, and J.-M. Hérard. A Mach-sensitive Implicit–Explicit Scheme Adapted to Compressible Multi-Scale Flows. In: *Journal of Computational and Applied Mathematics* 340 (Oct. 2018), pp. 122–150. DOI: 10.1016/j.cam.2018.02.019.

[65] S. Jin and Z. Xin. The relaxation schemes for systems of conservation laws in arbitrary space dimensions. In: *Communications on Pure and Applied Mathematics* 48.3 (1995), pp. 235–276. DOI: 10.1002/cpa.3160480303.

[66] J. Jung and V. Perrier. Steady low Mach number flows: Identification of the spurious mode and filtering method. In: *Journal of Computational Physics* 468 (Nov. 2022), p. 111462. DOI: 10.1016/j.jcp.2022.111462.

[67] K. Kaiser, J. Schütz, R. Schöbel, and S. Noelle. A New Stable Splitting for the Isentropic Euler Equations. In: *Journal of Scientific Computing* 70.3 (Mar. 2017), pp. 1390–1407. DOI: 10.1007/s10915-016-0286-6.

[68] S. A. Khan and A. Shah. Simulation of the two-dimensional Rayleigh-Taylor instability problem by using diffuse-interface model. In: *AIP Advances* 9.8 (Aug. 2019), p. 085312. DOI: 10.1063/1.5100791.

[69] R. Klein. Semi-Implicit Extension of a Godunov-Type Scheme Based on Low Mach Number Asymptotics I: One-dimensional Flow. In: *Journal of Computational Physics* 121.2 (Oct. 1995), pp. 213–237. DOI: 10.1016/S0021-9991(95)90034-9.

[70] O. Le Métayer and R. Saurel. The Noble-Abel Stiffened-Gas equation of state. In: *Physics of Fluids* 28.4 (Apr. 2016), p. 046102. DOI: 10.1063/1.4945981.

[71] D. Lecoanet, M. McCourt, E. Quataert, et al. A validated non-linear Kelvin–Helmholtz benchmark for numerical hydrodynamics. In: *Monthly Notices of the Royal Astronomical Society* 455.4 (Dec. 2015), pp. 4274–4288. DOI: 10.1093/mnras/stv2564.

[72] F. Lespagnol and G. Dakin. High order accurate schemes for Euler and Navier–Stokes equations on staggered Cartesian grids. In: *Journal of Computational Physics* 410 (June 2020), p. 109314. DOI: 10.1016/j.jcp.2020.109314.

[73] R. J. LeVeque. *Finite Volume Methods for Hyperbolic Problems.* Cambridge University Press, Aug. 2002. DOI: 10.1017/cbo9780511791253.

[74] M.-S. Liou. A sequel to AUSM, Part II: AUSM+-up for all speeds. In: *Journal of Computational Physics* 214.1 (May 2006), pp. 137–170. DOI: 10.1016/j.jcp.2005.09.020.

[75] R. Liska and B. Wendroff. Comparison of several difference schemes on 1D and 2D test problems for the Euler equations. In: *SIAM Journal on Scientific Computing* 25.3 (2003), pp. 995–1017. DOI: 10.1137/S1064827502402120.

[76] J. Llobell. Schémas volumes finis à mailles décalées pour la dynamique des gaz. PhD thesis. Université Côte d'Azur (ComUE), 2018. URL: http://www.theses.fr/2018AZUR4077/document.

[77] F. Miczek, F. K. Röpke, and P. V. F. Edelmann. New Numerical Solver for Flows at Various Mach Numbers. In: *Astronomy & Astrophysics* 576 (Apr. 2015), A50. DOI: 10.1051/0004-6361/201425059.

[78] W. Noh. Errors for calculations of strong shocks using an artificial viscosity and an artificial heat flux. In: *Journal of Computational Physics* 72.1 (1987), pp. 78–120. DOI: 10.1016/0021-9991(87)90074-x.

[79] T. Padioleau, P. Tremblin, E. Audit, P. Kestener, and S. Kokh. A high-performance and portable all-Mach regime flow solver code with well-balanced gravity. Application to compressible convection. In: *The Astrophysical Journal* 875.2 (2019), p. 128. DOI: 10.3847/1538-4357/ab0f2c.

[80] R. Rannacher and S. Turek. Simple nonconforming quadrilateral Stokes element. In: *Numerical Methods for Partial Differential Equations* 8 (1992), pp. 97–111.

[81] W. J. Rider. Revisiting Wall Heating. In: *Journal of Computational Physics* 162.2 (Aug. 2000), pp. 395–410. DOI: 10.1006/jcph.2000.6544.

[82] F. Rieper. A low-Mach number fix for Roe's approximate Riemann solver. In: *Journal of Computational Physics* 230.13 (June 2011), pp. 5263–5287. DOI: 10.1016/j.jcp.2011.03.025.

[83] F. Rieper and G. Bader. The influence of cell geometry on the accuracy of upwind schemes in the low mach number regime. In: *Journal of Computational Physics* 228.8 (May 2009), pp. 2918–2933. DOI: 10.1016/j.jcp.2009.01.002.

[84] B. E. Robertson, A. V. Kravtsov, N. Y. Gnedin, T. Abel, and D. H. Rudd. Computational Eulerian hydrodynamics and Galilean invariance. In: *Monthly Notices of the Royal Astronomical Society* 401.4 (Jan. 2010), pp. 2463–2476. DOI: 10.1111/j.1365-2966.2009.15823.x.

[85] S. Schochet. Fast Singular Limits of Hyperbolic PDEs. In: *Journal of Differential Equations* 114.2 (Dec. 1994), pp. 476–512. DOI: 10.1006/jdeq.1994.1157.

[86] J. M. Stone. *Kelvin-Helmholtz Instability Test.* URL: https://www.astro.princeton.edu/~jstone/Athena/tests/kh/kh.html.

[87] I. Suliciu. On the thermodynamics of rate-type fluids and phase transitions. I. Rate-type fluids. In: *International Journal of Engineering Science* 36.9 (1998), pp. 921–947. DOI: 10.1016/S0020-7225(98)00005-6.

[88] R. Témam. Sur l'approximation de la solution des équations de Navier-Stokes par la méthode des pas fractionnaires (II). In: *Archive for Rational Mechanics and Analysis* 33.5 (Jan. 1969), pp. 377–385. DOI: 10.1007/bf00247696.

[89] N. Therme. Schémas numériques pour la simulation de l'explosion. PhD thesis. Aix-Marseille Université, 2015. URL: http://www.theses.fr/2015AIXM4775/document.

[90] A. Thomann, G. Puppo, and C. Klingenberg. An all speed second order well-balanced IMEX relaxation scheme for the Euler equations with gravity. In: *Journal of Computational Physics* 420 (Nov. 2020), p. 109723. DOI: 10.1016/j.jcp.2020.109723.

[91] E. F. Toro. *Riemann solvers and numerical methods for fluid dynamics*. 3rd. Springer, 2009.

[92] E. Turkel. Preconditioned Methods for Solving the Incompressible and Low Speed Compressible Equations. In: *Journal of Computational Physics* 72.2 (Oct. 1987), pp. 277–298. DOI: 10.1016/0021-9991(87)90084-2.

[93] P. Virtanen, R. Gommers, T. E. Oliphant, et al. SciPy 1.0: Fundamental Algorithms for Scientific Computing in Python. In: *Nature Methods* 17 (2020), pp. 261–272. DOI: 10.1038/s41592-019-0686-2.

[94] J. VonNeumann and R. D. Richtmyer. A Method for the Numerical Calculation of Hydrodynamic Shocks. In: *Journal of Applied Physics* 21.3 (Mar. 1950), pp. 232–237. DOI: 10.1063/1.1699639.

[95] P. Wesseling. *Principles of Computational Fluid Dynamics*. Springer Berlin Heidelberg, 2001. DOI: 10.1007/978-3-642-05146-3.

[96] H. Weyl. Shock waves in arbitrary fluids. In: *Classic Papers in Shock Compression Science*. Ed. by J. N. Johnson and R. Chéret. New York, NY: Springer New York, 1998, pp. 497–519. DOI: 10.1007/978-1-4612-2218-7_12.

A Mass fluxes calculation on the dual faces

The computation of the dual flux $\widetilde{F}_{\sigma,\varepsilon}$ depends on the chosen discretization. It is defined so as to ensure that the mass balance over each half-dual cell remains consistent and proportional to the corresponding balance over the associated primal cell. Accordingly, we aim to express the mass flux over the dual face as a function of the mass flux over the primal face to ensure the stability of the scheme.

A.1 MAC discretization

In the case of the MAC discretization, we remind that the half dual cells at a given face σ is exactly the half volume of the corresponding primal cell volume. In other words we have

$$\forall \sigma = K|L \in \mathcal{E}_{int}, \qquad |D_{K,\sigma}| = \frac{|K|}{2}, \quad |D_{L,\sigma}| = \frac{|L|}{2}, \quad |D_\sigma| = |D_{K,\sigma}| + |D_{L,\sigma}|. \tag{120}$$

Thus, summing the half of (35a) over cells K and L and using definition (17) for ρ_{D_σ} leads to

$$\forall \sigma \in \mathcal{E}_{int}, \qquad \frac{|D_\sigma|}{\delta t} \left(\rho_{D_\sigma}^{n+1} - \rho_{D_\sigma}^{n}\right) + \sum_{\sigma \in \mathcal{E}(K)} \frac{\widetilde{F}_{K,\sigma}}{2} + \sum_{\sigma \in \mathcal{E}(L)} \frac{\widetilde{F}_{L,\sigma}}{2} = 0. \tag{121}$$

A natural choice for the dual mass fluxes $\widetilde{F}_{\sigma,\varepsilon}$ is:

$$\forall \sigma = K|L \in \mathcal{E}_{int}, \forall \varepsilon \in \mathcal{E}\left(D_\sigma\right), \quad \widetilde{F}_{\sigma,\varepsilon} = \frac{1}{2}\left(\widetilde{F}_{K,\sigma_K} + \widetilde{F}_{L,\sigma_L}\right), \tag{122}$$

with $(\sigma_K, \sigma_L) \in \mathcal{E}(K) \times \mathcal{E}(L)$ such that $\mathbf{n}_{K,\sigma_K} = \mathbf{n}_{L,\sigma_L} = \mathbf{n}_{\sigma,\varepsilon}$. In other words we combine primal mass fluxes of same orientation to build the corresponding dual mass fluxes. This means that the flux through a dual face which is located on two primal faces is the mean value of the sum of fluxes on the two primal faces, and the flux through a dual face located between two primal faces is again the mean value of the sum of fluxes on the two primal faces. We now present a practical example for 2D cartesian elements as shown in [62].
Let us consider a uniform 2D grid so that $|K| = |L|$ and $|D_\sigma| = \frac{1}{2}(|K| + |L|) = |K| = |L|$. We note the primal fluxes and dual fluxes associated to those elements as on Figure 21.

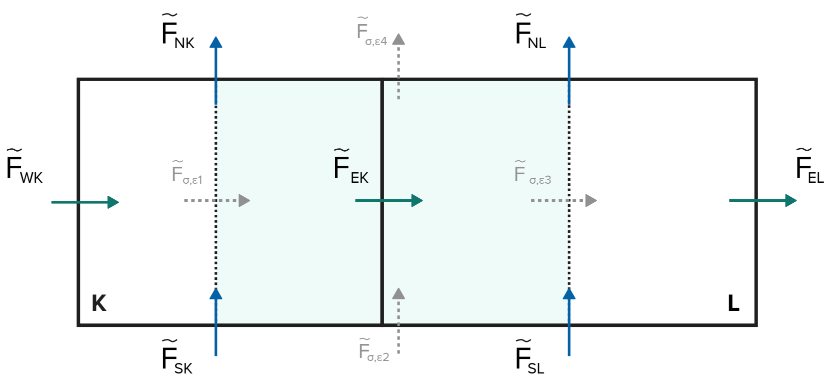

Figure 21: Local notations for the MAC discretization

Then the mass balance equations over the two primal cells K and L read

$$\frac{|K|}{\delta t}(\rho_K^{n+1} - \rho_K^n) - \widetilde{F}_{WK} - \widetilde{F}_{SK} + \widetilde{F}_{EK} + \widetilde{F}_{NK} = 0,$$
$$\frac{|L|}{\delta t}(\rho_L^{n+1} - \rho_L^n) - \widetilde{F}_{EK} - \widetilde{F}_{SL} + \widetilde{F}_{EL} + \widetilde{F}_{NL} = 0.$$

Thus, multiplying the two equations by half and summing them yields for $\sigma = K|L$,

$$\frac{|D_\sigma|}{\delta t}\left(\rho_{D_\sigma}^{n+1} - \rho_{D_\sigma}^n\right) - \frac{1}{2}\left[\widetilde{F}_{WK} + \widetilde{F}_{EK}\right] - \frac{1}{2}\left[\widetilde{F}_{SK} + \widetilde{F}_{SL}\right] + \frac{1}{2}\left[\widetilde{F}_{EK} + \widetilde{F}_{EL}\right] + \frac{1}{2}\left[\widetilde{F}_{NK} + \widetilde{F}_{NL}\right] = 0,$$

with $|D_{K,\sigma}| = |K|/2$ and $|D_{L,\sigma}| = |L|/2$, derived from the definition of the dual cell D_σ, while the densities $\rho_{D_\sigma}^{n+1}$, $\rho_{D_\sigma}^n$ on the dual cell are given by relation (17). This suggests the following definitions

$$\widetilde{F}_{\sigma,\varepsilon_1} = -\frac{1}{2}\left[\widetilde{F}_{WK} + \widetilde{F}_{EK}\right], \qquad \widetilde{F}_{\sigma,\varepsilon_2} = \frac{1}{2}\left[\widetilde{F}_{SK} + \widetilde{F}_{SL}\right],$$
$$\widetilde{F}_{\sigma,\varepsilon_3} = -\frac{1}{2}\left[\widetilde{F}_{EK} + \widetilde{F}_{EL}\right], \qquad \widetilde{F}_{\sigma,\varepsilon_4} = \frac{1}{2}\left[\widetilde{F}_{NK} + \widetilde{F}_{NL}\right].$$

A.2 RT/CR discretization

For the Rannacher-Turek and Crouzeix-Raviart elements, we mainly recall the previous work from [1, 11, 13, 37]. The fluxes through the dual faces of the dual mesh must satisfy the following three constraints.

1. The discrete mass balance over the half-diamond cells is satisfied, in the sense that for any cell $K \in \mathcal{M}$, the set of dual fluxes $\widetilde{F}_{\sigma,\varepsilon}, \varepsilon \in \widetilde{\mathcal{E}}\,(D_{K,\sigma})$, with $\widetilde{\mathcal{E}}\,(D_{K,\sigma})$ defined in (12), is solution of the following linear system

$$\begin{aligned} &\forall \sigma \in \mathcal{E}(K), \qquad \widetilde{F}_{K,\sigma} + \sum_{\varepsilon \in \widetilde{\mathcal{E}}(D_{K,\sigma})} \widetilde{F}_{\sigma,\varepsilon} = \xi_K^\sigma \sum_{\sigma' \in \mathcal{E}(K)} \widetilde{F}_{K,\sigma'}, \\ &\text{with} \sum_{\sigma \in \mathcal{E}(K)} \xi_K^\sigma = 1 \text{ and for any } \sigma \in \mathcal{E}(K),\ \xi_K^\sigma > 0. \end{aligned} \tag{123}$$

2. The dual fluxes are conservative meaning that for any $\varepsilon = D_\sigma | D_{\sigma'}, \widetilde{F}_{\sigma,\varepsilon} = -\widetilde{F}_{\sigma',\varepsilon}$.
3. The dual fluxes are bounded with respect to the primal fluxes, in the sense that there exists a constant real number C such that:

$$\forall \sigma \in \mathcal{E}_{int}, \varepsilon \in \widetilde{\mathcal{E}}\,(D_{K,\sigma}), \qquad \left|\widetilde{F}_{\sigma,\varepsilon}\right| \leq C \max\left\{\left|\widetilde{F}_{K,\sigma'}\right|, \sigma' \in \mathcal{E}(K)\right\}. \tag{124}$$

These three assumptions are sufficient to imply the consistency of the discrete convection operator. However, system of equation (123) is singular and has an infinite number of solutions. The choice of a particular solution depends on the type of grid. Since (123) is a linear system for the dual mass fluxes, a solution of (123) may be written as

$$\widetilde{F}_{\sigma,\varepsilon} = \sum_{\sigma' \in \mathcal{E}(K)} \beta_{K,\sigma'}^\varepsilon \widetilde{F}_{K,\sigma'}, \qquad \sigma \in \mathcal{E}(K), \varepsilon \in \widetilde{\mathcal{E}}\,(D_{K,\sigma}), \tag{125}$$

where $\beta^{\varepsilon}_{K,\sigma'}$ depends on the topology of cell K, the considered dual face ε and the considered primal face σ'. The constraint (124) amounts to require the coefficients $\beta^{\varepsilon}_{K,\sigma'}$ to be bounded by a constant. In practice, the coefficients used satisfy:

$$\sum_{\sigma' \in \mathcal{E}(K)} \left|\beta^{\varepsilon}_{K,\sigma'}\right| \leq 1.$$

Moreove, we set the coefficients ξ^{σ}_{K} for a given element K as follow

$$\xi^{\sigma}_{K} = \frac{1}{\operatorname{card}\left(\mathcal{E}(K)\right)}.$$

In our approach, we adopt the choice of solution presented in [13] for both triangular and quadrilateral meshes. We remind in the tables 5 and 6 the values of the coefficients $\beta^{\varepsilon}_{K,\sigma'}$ respectively for the case of a triangular element:

$$\widetilde{F}_{\sigma,\varepsilon} = \beta^{\varepsilon}_{W}\widetilde{F}_{W} + \beta^{\varepsilon}_{E}\widetilde{F}_{E} + \beta^{\varepsilon}_{S}\widetilde{F}_{S},$$

and for a quadrangle element:

$$\widetilde{F}_{\sigma,\varepsilon} = \beta^{\varepsilon}_{W}\widetilde{F}_{W} + \beta^{\varepsilon}_{E}\widetilde{F}_{E} + \beta^{\varepsilon}_{S}\widetilde{F}_{S} + \beta^{\varepsilon}_{N}\widetilde{F}_{N}.$$

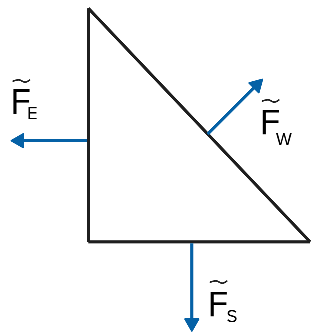

Figure 22: Primal flux over a triangle

$\varepsilon = D_\sigma \vert D_{\sigma'}$	β^{ε}_{W}	β^{ε}_{E}	β^{ε}_{S}
$W\vert S$	-1/3	0	1/3
$S\vert E$	0	1/3	-1/3
$E\vert W$	1/3	-1/3	0

Table 5: Values of the coefficients $\beta^{\varepsilon}_{K,\sigma'}$ for a triangular element

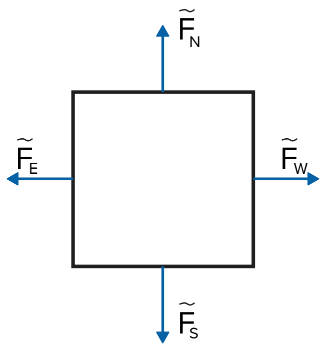

Figure 23: Primal flux over a quadrangle

$\varepsilon = D_\sigma \vert D_{\sigma'}$	β^{ε}_{W}	β^{ε}_{E}	β^{ε}_{S}	β^{ε}_{N}
$W\vert S$	-3/8	1/8	-1/8	-1/8
$S\vert E$	-1/8	3/8	-3/8	1/8
$E\vert W$	1/8	-3/8	-1/8	3/8
$N\vert W$	3/8	-1/8	1/8	-3/8

Table 6: Values of the coefficients $\beta^{\varepsilon}_{K,\sigma'}$ for a quadrangle element

B Reduction of the linear system to the relaxation pressure unknown in the acoustic step

In this section, we show how to reduce the linear system over $(\widetilde{u}_\sigma)_{\sigma\in\mathcal{E}_{\text{int}}}$ and $(\widetilde{\pi}_K)_{K\in\mathcal{M}}$, defined by equations (19b) and (19c) of the acoustic subsystem (19), into a linear system involving only the relaxation pressure $\widetilde{\pi}_K$, $\forall K\in\mathcal{M}$. The key idea is to apply the discrete divergence operator to equation (19b), and subsequently substitute the resulting expression into equation (19c). First we start by recalling the following definitions:

$$
\begin{aligned}
(\boldsymbol{\nabla}\cdot\widetilde{\mathbf{u}})_K &= \frac{1}{|K|}\sum_{\sigma\in\mathcal{E}(K)}|\sigma|\widetilde{u}^*_{K,\sigma},\\
\widetilde{u}^*_{K,\sigma} &= \widetilde{u}_{K,\sigma} - \frac{1}{2a^n_{D_\sigma}}\left(\widetilde{\pi}_L-\widetilde{\pi}_K\right),\\
(\boldsymbol{\nabla}\widetilde{\pi})_{D_\sigma} &= \frac{1}{|D_\sigma|}\left(\widetilde{\pi}_L-\widetilde{\pi}_K\right)|\sigma|\mathbf{n}_{K,\sigma}.
\end{aligned}
$$

We can first rewrite equation (19c) as:

$$
\forall K\in\mathcal{M},\qquad \frac{|K|}{\delta t}\rho^n_K\left(\widetilde{\pi}_K-\pi^n_K\right)+\left(a^n_K\right)^2\sum_{\substack{\sigma\in\mathcal{E}(K)\\ \sigma=K|L}}|\sigma|\left(\widetilde{u}_{K,\sigma}-\frac{1}{2a^n_{D_\sigma}}(\widetilde{\pi}_L-\widetilde{\pi}_K)\right)=0.
$$

Next, multiplying equation (19b) by the normal $\mathbf{n}_{K,\sigma}$ gives the update formula for $\widetilde{u}_{K,\sigma}$:

$$
\widetilde{u}_{K,\sigma}=u^n_{K,\sigma}-\frac{\lambda^n_\sigma}{\rho^n_{D_\sigma}}(\widetilde{\pi}_L-\widetilde{\pi}_K), \tag{126}
$$

where

$$
\lambda^n_\sigma=\delta t\frac{|\sigma|}{|D_\sigma|}. \tag{127}
$$

Substituting this expression into the previous equation gives:

$$
\forall K\in\mathcal{M},\qquad \widetilde{\pi}_K-\pi^n_K+\frac{\delta t}{\rho^n_K|K|}\left(a^n_K\right)^2\sum_{\substack{\sigma\in\mathcal{E}(K)\\ \sigma=K|L}}|\sigma|\left[u^n_{K,\sigma}-\left(\frac{1}{2a^n_{D_\sigma}}+\frac{\lambda^n_\sigma}{\rho^n_{D_\sigma}}\right)(\widetilde{\pi}_L-\widetilde{\pi}_K)\right]=0.
$$

Reorganizing terms yields the final expression for the reduced linear system on $(\widetilde{\pi}_K)_{K\in\mathcal{M}}$:

$$
\begin{aligned}
\left[1+\frac{\delta t\left(a^n_K\right)^2}{\rho^n_K|K|}\sum_{\sigma\in\mathcal{E}(K)}|\sigma|\left(\frac{1}{2a^n_{D_\sigma}}+\frac{\lambda^n_\sigma}{\rho^n_{D_\sigma}}\right)\right]\widetilde{\pi}_K-\frac{\delta t\left(a^n_K\right)^2}{\rho^n_K|K|}\sum_{\substack{\sigma\in\mathcal{E}(K)\\ \sigma=K|L}}|\sigma|\left(\frac{1}{2a^n_{D_\sigma}}+\frac{\lambda^n_\sigma}{\rho^n_{D_\sigma}}\right)\widetilde{\pi}_L&\\
=\pi^n_K-\frac{\delta t}{\rho^n_K|K|}\left(a^n_K\right)^2\sum_{\sigma\in\mathcal{E}(K)}|\sigma|u^n_{K,\sigma},\qquad \forall K\in\mathcal{M}.&
\end{aligned}\tag{128}
$$

In practice, we solve the linear system for the relaxation pressure using iterative solvers. For sparse square systems, we employ the bi-conjugate gradient stabilized method (BiCGStab) from the Eigen C++ library [45] or the LGMRES solver in Python from SciPy [93]. When supported by the chosen iterative solver, we also set the initial guess to π^n_K. Finally, it is worth noting that the sparse matrix associated to the linear system (128) tends to the identity matrix as $\delta t \to 0$, while the right-hand side tends to π_K^n.

C Proofs of stability results

C.1 Preliminary technical results

Lemma C.1. *Let $\overline{s} \in \mathbb{R}$, suppose that there exists $a > 0$ such that*

$$a^2 + \left(\frac{\partial p^{EOS}}{\partial \tau}\right)_s (\tau', \overline{s}) > 0, \quad \textit{for all } \tau' > 0. \tag{129}$$

For given $\pi \in \mathbb{R}$ and $\tau > 0$, if that there exists $\mathcal{V} > 0$ such that

$$p^{EOS}(\mathcal{V}, \overline{s}) + a^2 \mathcal{V} = \pi + a^2 \tau, \tag{130}$$

then is unique and it verifies

$$e^{EOS}(\tau, \overline{s}) \leq e^{EOS}(\mathcal{V}, \overline{s}) + \frac{\pi^2 - p^{EOS}(\mathcal{V}, \overline{s})^2}{2a^2}. \tag{131}$$

Proof. The subcharacteristic condition (129) implies that for any fixed $\overline{s} \in \mathbb{R}$, the function $\tau' > 0 \mapsto p^{\mathrm{EOS}}(\tau', \overline{s}) + a^2 \tau'$ is strictly increasing, which guarantees uniqueness for $\mathcal{V}$.

For fixed values of τ, π and $\mathcal{V}$ verifying (130). We have then

$$e^{\mathrm{EOS}}(\mathcal{V}, \overline{s}) + \frac{\pi^2 - p^{\mathrm{EOS}}(\mathcal{V}, \overline{s})^2}{2a^2} = e^{\mathrm{EOS}}(\mathcal{V}, \overline{s}) + \frac{a^2}{2}(\mathcal{V} - \tau)^2 + p^{\mathrm{EOS}}(\mathcal{V}, \overline{s})(\mathcal{V} - \tau). \tag{132}$$

We set $\Psi : \tau' \mapsto e^{\mathrm{EOS}}(\tau', \overline{s}) + \frac{1}{2}a^2(\tau' - \tau)^2 + p^{\mathrm{EOS}}(\tau', \overline{s})(\tau' - \tau)$. Let us prove that Ψ is lower bounded by $e^{\mathrm{EOS}}(\tau, \overline{s})$. Indeed, we have $\dfrac{\mathrm{d}\Psi}{\mathrm{d}\tau'}(\tau') = (\tau' - \tau)\left(a^2 + \left(\dfrac{\partial p^{\mathrm{EOS}}}{\partial \tau}\right)_s (\tau', \overline{s})\right)$, so that assumption (129) yields $\operatorname{sign}\left(\dfrac{\mathrm{d}\Psi}{\mathrm{d}\tau'}(\tau')\right) = \operatorname{sign}(\tau' - \tau)$. Consequently, Ψ reaches a minimum at $\tau' = \tau$, that is to say $\Psi(\tau') \geq \Psi(\tau) = e^{\mathrm{EOS}}(\tau, \overline{s})$, for all $\tau' > 0$, applying this result for $\tau' = \mathcal{V}$ yields inequality (131).

□

Let us remark that in (131), the only role of the variable $\overline{s}$ is that of a neutral parameter. Therefore, these relations remain valid if one supposes that $(\partial e^{\mathrm{EOS}}/\partial s)_\tau = 0$. In other words, (131) remains valid in the case of a barotropic EOS with $e^{\mathrm{EOS}}(\tau, \overline{s}) = e^{\mathrm{EOS}}(\tau)$ and $p^{\mathrm{EOS}}(\tau, \overline{s}) = p^{\mathrm{EOS}}(\tau) = -(\mathrm{d}e^{\mathrm{EOS}}/\mathrm{d}\tau)(\tau)$.

We have the following discrete gradient-divergence duality relation.

Lemma C.2. *For $(\boldsymbol{\nabla} \cdot \widetilde{\mathbf{u}})_K$ and $(\boldsymbol{\nabla}\widetilde{\pi})_{D_\sigma}$ defined by (20), and for the boundary conditions (13), we have the following relation:*

$$\sum_{K \in \mathcal{M}} |K| \widetilde{\pi}_K \, (\boldsymbol{\nabla} \cdot \widetilde{\mathbf{u}})_K + \sum_{\sigma = K|L \in \mathcal{E}_{int}} |D_\sigma| \mathbf{n}_{K,\sigma} \cdot (\boldsymbol{\nabla}\widetilde{\pi})_{D_\sigma} \, \widetilde{u}^*_{K,\sigma} = 0. \tag{133}$$

Proof. Let us first note that if the boundary terms verify (13), then

$$\widetilde{u}^*_{K,\sigma} = 0, \qquad \text{for } K \cap \partial\Omega \neq \emptyset,\ \sigma \subset \partial\Omega. \tag{134}$$

By mutiplying (20a) by $\widetilde{\pi}_K$ and taking the sum over all $K \in \mathcal{M}$, using (20b), we get

$$\sum_{K\in\mathcal{M}} |K|\widetilde{\pi}_K \left(\boldsymbol{\nabla}\cdot\widetilde{\mathbf{u}}\right)_K = \sum_{K\in\mathcal{M}} \sum_{\sigma\in\mathcal{E}(K)\cap\mathcal{E}_{\rm int}} |\sigma|\widetilde{\pi}_K\widetilde{u}^*_{K,\sigma} = \sum_{\sigma=K|L\in\mathcal{E}_{\rm int}} |\sigma|\left(\widetilde{\pi}_K\widetilde{u}^*_{K,\sigma} + \widetilde{\pi}_L\widetilde{u}^*_{L,\sigma}\right). \tag{135}$$

As $\widetilde{u}^*_{K,\sigma} = -\widetilde{\pi}_L\widetilde{u}^*_{L,\sigma}$ we have

$$\sum_{K\in\mathcal{M}} |K|\widetilde{\pi}_K \left(\boldsymbol{\nabla}\cdot\widetilde{\mathbf{u}}\right)_K = \sum_{\substack{\sigma\in\mathcal{E}_{\rm int}\\ \sigma=K|L}} |\sigma|(\widetilde{\pi}_K - \widetilde{\pi}_L)\widetilde{u}^*_{K,\sigma} = -\sum_{\substack{\sigma\in\mathcal{E}_{\rm int}\\ \sigma=K|L}} |D_\sigma|\widetilde{\mathbf{n}}_{K,\sigma}\cdot\left(\boldsymbol{\nabla}\widetilde{\pi}\right)_{D_\sigma}\widetilde{u}^*_{K,\sigma}. \tag{136}$$

□

Proof of Lemma 4.4. First of all, let us note that the mass equation (19a) reads

$$\frac{|K|}{\delta t}\left(\widetilde{\rho}_K - \rho^n_K\right) + \widetilde{\rho}_K|K|\left(\boldsymbol{\nabla}\cdot\widetilde{\mathbf{u}}\right)_K = 0. \tag{137}$$

Multiplying (137) over cells K and L respectively by $\frac{|D_{K,\sigma}|}{|K|}$, $\frac{|D_{L,\sigma}|}{|L|}$, summing and using definitions (28c) and (32) gives

$$\frac{|D_\sigma|}{\delta t}\left(\widetilde{\rho}_{D_\sigma} - \rho^n_{D_\sigma}\right) + \widetilde{\rho}_{D_\sigma}|D_\sigma|\left(\boldsymbol{\nabla}\cdot\widetilde{\mathbf{u}}\right)_{D_\sigma} = 0, \tag{138}$$

for all $\sigma \in \mathcal{E}_{int}$. This equation can also be written as

$$\widetilde{\rho}_{D_\sigma} = \frac{\rho^n_{D_\sigma}}{1 + \delta t\left(\boldsymbol{\nabla}\cdot\widetilde{\mathbf{u}}\right)_{D_\sigma}}, \tag{139}$$

which corresponds to a dual version of mass equation (24). Same operation is performed for equation (27a), that is

$$\frac{|D_\sigma|}{\delta t}\left(\rho^{n+1}_{D_\sigma} - \widetilde{\rho}_{D_\sigma}\right) + \sum_{\varepsilon\in\mathcal{E}(D_\sigma)} \widetilde{F}_{\sigma,\varepsilon} - \widetilde{\rho}_{D_\sigma}|D_\sigma|\left(\boldsymbol{\nabla}\cdot\widetilde{\mathbf{u}}\right)_{D_\sigma} = 0. \tag{140}$$

Then, by multiplying the equation (27b) by $\mathbf{u}^{n+1}_\sigma$, we have

$$\frac{|D_\sigma|}{\delta t}\left(\rho^{n+1}_{D_\sigma}\left|\mathbf{u}^{n+1}_\sigma\right|^2 - \widetilde{\rho}_{D_\sigma}\mathbf{u}^{n+1}_\sigma\cdot\widetilde{\mathbf{u}}_\sigma\right) + \mathbf{u}^{n+1}_\sigma\cdot\sum_{\varepsilon\in\mathcal{E}(D_\sigma)} \widetilde{F}_{\sigma,\varepsilon}\widetilde{\mathbf{u}}_\varepsilon - \widetilde{\rho}_{D_\sigma}\mathbf{u}^{n+1}_\sigma\cdot\widetilde{\mathbf{u}}_\sigma|D_\sigma|\left(\boldsymbol{\nabla}\cdot\widetilde{\mathbf{u}}\right)_{D_\sigma} = 0.$$

which is also equivalent to

$$\begin{aligned}\frac{|D_\sigma|}{\delta t}\left(\rho^{n+1}_{D_\sigma}\frac{\left|\mathbf{u}^{n+1}_\sigma\right|^2}{2} - \widetilde{\rho}_{D_\sigma}\frac{|\widetilde{\mathbf{u}}_\sigma|^2}{2}\right) + \frac{|D_\sigma|}{\delta t}\left(\rho^{n+1}_{D_\sigma}\frac{\left|\mathbf{u}^{n+1}_\sigma\right|^2}{2} - \widetilde{\rho}_{D_\sigma}\mathbf{u}^{n+1}_\sigma\cdot\widetilde{\mathbf{u}}_\sigma + \widetilde{\rho}_{D_\sigma}\frac{|\widetilde{\mathbf{u}}_\sigma|^2}{2}\right)\\ + \mathbf{u}^{n+1}_\sigma\cdot\sum_{\varepsilon\in\mathcal{E}(D_\sigma)} \widetilde{F}_{\sigma,\varepsilon}\widetilde{\mathbf{u}}_\varepsilon - \widetilde{\rho}_{D_\sigma}\mathbf{u}^{n+1}_\sigma\cdot\widetilde{\mathbf{u}}_\sigma|D_\sigma|\left(\boldsymbol{\nabla}\cdot\widetilde{\mathbf{u}}\right)_{D_\sigma} = 0.\end{aligned}$$

Using (140) to express $\rho_{D_\sigma}^{n+1}$ as a function of $\widetilde{\rho}_{D_\sigma}$ and dual fluxes $F_{\sigma,\varepsilon}$ and reinjecting into above equation gives the following:

$$\begin{aligned}\frac{|D_\sigma|}{\delta t}\left(\rho_{D_\sigma}^{n+1}\frac{\left|\mathbf{u}_\sigma^{n+1}\right|^2}{2}-\widetilde{\rho}_{D_\sigma}\frac{|\widetilde{\mathbf{u}}_\sigma|^2}{2}\right)+\frac{|D_\sigma|}{\delta t}\frac{\widetilde{\rho}_{D_\sigma}}{2}\left(\mathbf{u}_\sigma^{n+1}-\widetilde{\mathbf{u}}_\sigma\right)^2&\\ -\frac{\left|\mathbf{u}_\sigma^{n+1}\right|^2}{2}\sum_{\varepsilon\in\mathcal{E}(D_\sigma)}\widetilde{F}_{\sigma,\varepsilon}+\widetilde{\rho}_{D_\sigma}\frac{\left|\mathbf{u}_\sigma^{n+1}\right|^2}{2}|D_\sigma|\left(\boldsymbol{\nabla}\cdot\widetilde{\mathbf{u}}\right)_{D_\sigma}&\\ +\mathbf{u}_\sigma^{n+1}\cdot\sum_{\varepsilon\in\mathcal{E}(D_\sigma)}\widetilde{F}_{\sigma,\varepsilon}\widetilde{\mathbf{u}}_\varepsilon-\widetilde{\rho}_{D_\sigma}\mathbf{u}_\sigma^{n+1}\cdot\widetilde{\mathbf{u}}_\sigma|D_\sigma|\left(\boldsymbol{\nabla}\cdot\widetilde{\mathbf{u}}\right)_{D_\sigma}&=0.\end{aligned}$$

With (138), this equation also writes:

$$\begin{aligned}\frac{|D_\sigma|}{\delta t}\left(\rho_{D_\sigma}^{n+1}\frac{\left|\mathbf{u}_\sigma^{n+1}\right|^2}{2}-\widetilde{\rho}_{D_\sigma}\frac{|\widetilde{\mathbf{u}}_\sigma|^2}{2}\right)+\frac{|D_\sigma|}{\delta t}\frac{\rho_{D_\sigma}^{n}}{2}\left|\mathbf{u}_\sigma^{n+1}-\widetilde{\mathbf{u}}_\sigma\right|^2-\frac{\widetilde{\rho}_{D_\sigma}}{2}\left|\mathbf{u}_\sigma^{n+1}-\widetilde{\mathbf{u}}_\sigma\right|^2|D_\sigma|\left(\boldsymbol{\nabla}\cdot\widetilde{\mathbf{u}}\right)_{D_\sigma}&\\ -\frac{\left|\mathbf{u}_\sigma^{n+1}\right|^2}{2}\sum_{\varepsilon\in\mathcal{E}(D_\sigma)}\widetilde{F}_{\sigma,\varepsilon}+\widetilde{\rho}_{D_\sigma}\frac{\left|\mathbf{u}_\sigma^{n+1}\right|^2}{2}|D_\sigma|\left(\boldsymbol{\nabla}\cdot\widetilde{\mathbf{u}}\right)_{D_\sigma}&\\ +\mathbf{u}_\sigma^{n+1}\cdot\sum_{\varepsilon\in\mathcal{E}(D_\sigma)}\widetilde{F}_{\sigma,\varepsilon}\widetilde{\mathbf{u}}_\varepsilon-\widetilde{\rho}_{D_\sigma}\mathbf{u}_\sigma^{n+1}\cdot\widetilde{\mathbf{u}}_\sigma|D_\sigma|\left(\boldsymbol{\nabla}\cdot\widetilde{\mathbf{u}}\right)_{D_\sigma}&=0.\end{aligned}$$

Finally, by adding-substracting the convective term of the kinetic energy, we have

$$\begin{aligned}\frac{|D_\sigma|}{\delta t}\left(\rho_{D_\sigma}^{n+1}\frac{\left|\mathbf{u}_\sigma^{n+1}\right|^2}{2}-\rho_{D_\sigma}^{n}\frac{|\widetilde{\mathbf{u}}_\sigma|^2}{2}\right)+\sum_{\varepsilon\in\mathcal{E}(D_\sigma)}\widetilde{F}_{\sigma,\varepsilon}\frac{|\widetilde{\mathbf{u}}_\varepsilon|^2}{2}-\sum_{\varepsilon\in\mathcal{E}(D_\sigma)}\widetilde{F}_{\sigma,\varepsilon}\frac{|\widetilde{\mathbf{u}}_\varepsilon|^2}{2}&\\ -\frac{\left|\mathbf{u}_\sigma^{n+1}\right|^2}{2}\sum_{\varepsilon\in\mathcal{E}(D_\sigma)}\widetilde{F}_{\sigma,\varepsilon}+\mathbf{u}_\sigma^{n+1}\cdot\sum_{\varepsilon\in\mathcal{E}(D_\sigma)}\widetilde{F}_{\sigma,\varepsilon}\widetilde{\mathbf{u}}_\varepsilon&\\ -\widetilde{\rho}_{D_\sigma}\frac{|\widetilde{\mathbf{u}}_\sigma|^2}{2}|D_\sigma|\left(\boldsymbol{\nabla}\cdot\widetilde{\mathbf{u}}\right)_{D_\sigma}&=-\frac{|D_\sigma|}{\delta t}\frac{\rho_{D_\sigma}^{n}}{2}\left|\mathbf{u}_\sigma^{n+1}-\widetilde{\mathbf{u}}_\sigma\right|^2.\end{aligned}$$

Noticing that $\mathbf{u}_\sigma^{n+1}$ does not depend on index ε, which means that it can be inserted inside the terms of sum on the second line, leads to the final equation (33) with source term (34).
We finally show the CFL condition associated with (38a). We note σ' the downstream face of the dual face ε. Then using (18) allows us to decompose R_σ^{n+1} as follow

$$\begin{aligned}R_\sigma^{n+1}&=\frac{|D_\sigma|}{\delta t}\frac{\rho_{D_\sigma}^{n}}{2}\left|\mathbf{u}_\sigma^{n+1}-\widetilde{\mathbf{u}}_\sigma\right|^2-\sum_{\varepsilon\in\mathcal{E}(D_\sigma)}\frac{\widetilde{F}_{\sigma,\varepsilon}}{2}\left|\mathbf{u}_\sigma^{n+1}-\widetilde{\mathbf{u}}_\varepsilon\right|^2\\ &=\frac{|D_\sigma|}{\delta t}\frac{\rho_{D_\sigma}^{n}}{2}\left|\mathbf{u}_\sigma^{n+1}-\widetilde{\mathbf{u}}_\sigma\right|^2-\sum_{\varepsilon\in\mathcal{E}(D_\sigma)}\frac{\widetilde{F}_{\sigma,\varepsilon}^{+}}{2}\left|\mathbf{u}_\sigma^{n+1}-\widetilde{\mathbf{u}}_\sigma\right|^2+\sum_{\varepsilon\in\mathcal{E}(D_\sigma)}\frac{\widetilde{F}_{\sigma,\varepsilon}^{-}}{2}\left|\mathbf{u}_\sigma^{n+1}-\widetilde{\mathbf{u}}_{\sigma'}\right|^2\\ &=\frac{1}{2}\left|\mathbf{u}_\sigma^{n+1}-\widetilde{\mathbf{u}}_\sigma\right|^2\underbrace{\left(\frac{|D_\sigma|}{\delta t}\rho_{D_\sigma}^{n}-\sum_{\varepsilon\in\mathcal{E}(D_\sigma)}\widetilde{F}_{\sigma,\varepsilon}^{+}\right)}_{\geq 0\text{ under condition (38a)}}+\underbrace{\sum_{\varepsilon\in\mathcal{E}(D_\sigma)}\frac{\widetilde{F}_{\sigma,\varepsilon}^{-}}{2}\left|\mathbf{u}_\sigma^{n+1}-\widetilde{\mathbf{u}}_{\sigma'}\right|^2}_{\geq 0\ \forall\delta t},\end{aligned}$$

which ends the proof. □

Proof of proposition 4.2.
Multiplying (19c) (resp. (57d)) by $\widetilde{\pi}_K$ yields $(\widetilde{\pi}_K^2 - \widetilde{\pi}_K \pi_K^n) + \delta t (a_K^n)^2 \tau_K^n \widetilde{\pi}_K (\boldsymbol{\nabla} \cdot \widetilde{\mathbf{u}})_K = 0$. Using $-2\widetilde{\pi}_K \pi_K^n = (\widetilde{\pi}_K - \pi_K^n)^2 - \widetilde{\pi}_K^2 - (\pi_K^n)^2$, we get $\frac{1}{2}\left(\widetilde{\pi}_K^2 - (\pi_K^n)^2\right) + \delta t (a_K^n)^2 \tau_K^n \widetilde{\pi}_K (\boldsymbol{\nabla} \cdot \widetilde{\mathbf{u}})_K = -(\widetilde{\pi}_K - \pi_K^n)^2$, hence relation (25).

Adding the sum of (25) over all $K \in \mathcal{M}$ and the sum of (21) over all $\sigma \in \mathcal{E}_{int}$ yields

$$\sum_{K \in \mathcal{M}} |K| \frac{\rho_K^n}{\delta t} \left[\frac{(\widetilde{\pi}_K)^2}{2(a_K^n)^2} - \frac{(\pi_K^n)^2}{2(a_K^n)^2} \right] + \sum_{\sigma \in \mathcal{E}_{int}} \frac{|D_\sigma|}{\delta t} \rho_{D_\sigma}^n \left[\frac{|\widetilde{\mathbf{u}}_\sigma|^2}{2} - \frac{|\mathbf{u}_\sigma^n|^2}{2} \right] + \sum_{K \in \mathcal{M}} |K| \widetilde{\pi}_K (\boldsymbol{\nabla} \cdot \widetilde{\mathbf{u}})_K$$
$$+ \sum_{\sigma \in \mathcal{E}_{int}} \widetilde{u}_{K,\sigma}^* |D_\sigma| (\boldsymbol{\nabla} \widetilde{\pi})_{D_\sigma} \cdot \mathbf{n}_{K,\sigma} = - \sum_{K \in \mathcal{M}} |K| \frac{\rho_K^n}{\delta t} \frac{(\widetilde{\pi}_K - \pi_K^n)^2}{2(a_K^n)^2} - \sum_{\sigma \in \mathcal{E}_{int}} \widetilde{R}_\sigma, \quad (141)$$

then relation (133) yields (26). □

Proof of proposition 4.3.
Let us consider the linear system (19b)-(19c). If $(\widetilde{\pi}_K)_{K \in \mathcal{M}}$ and $(\widetilde{\mathbf{u}}_\sigma)_{\sigma \in \mathcal{E}_{int}}$ belong to the kernel of the matrix associated with (19b)-(19c), then they verify (19b)-(19c) with $\pi_k^n = 0$, for all $K \in \mathcal{M}$ and $\mathbf{u}_\sigma^n = \mathbf{0}$ for all $\sigma \in \mathcal{E}_{int}$. In this case, (26) reads

$$\sum_{K \in \mathcal{M}} |K| \frac{\rho_K^n}{\delta t} \frac{(\widetilde{\pi}_K)^2}{2(a_K^n)^2} + \sum_{\sigma \in \mathcal{E}_{int}} \frac{|D_\sigma|}{\delta t} \rho_{D_\sigma}^n \frac{|\widetilde{\mathbf{u}}_\sigma|^2}{2} \leq 0. \quad (142)$$

This implies that $\widetilde{\pi}_K = 0$ for all $K \in \mathcal{M}$ and $\widetilde{\mathbf{u}}_\sigma = \mathbf{0}$ for all $\sigma \in \mathcal{E}_{int}$. □

C.2 Proofs of stability estimates for the barotropic system

Proof of proposition 4.5.
Proof of point 1: granted that $1 + \delta t (\boldsymbol{\nabla} \cdot \widetilde{\mathbf{u}})_K \geq 1 - \delta t \sum_{\sigma \in \mathcal{E}(K)} \frac{|\sigma|}{|K|} \left(\widetilde{u}_{K,\sigma}^*\right)^-$, using definition (24) of $\widetilde{\rho}_K$, we see that the CFL condition (38b) implies $\widetilde{\rho}_K \geq 0$, which proves the first inequality of (39). The second equation of (39) is a direct consequence of (19a) and (19c). We now remark that at the instant t^n, the pressure π is at equilibrium: $\pi_K^n = p^{\mathrm{EOS}}(\tau_K^n)$. This means that (130) is verified with $\tau = \widetilde{\tau}_K$, $\pi = \widetilde{\pi}_K$, $\mathcal{V} = \tau_K^n$. We can thus apply (131) which yields the third relation of (39).

Proof of point 2: relation (25) yields

$$\frac{\rho_K^n}{\delta t} \left(e^{\mathrm{EOS}}(\tau_K^n) + \frac{(\widetilde{\pi}_K)^2}{2(a_K^n)^2} - \frac{(\pi_K^n)^2}{2(a_K^n)^2} - e^{\mathrm{EOS}}(\tau_K^n) \right) + \widetilde{\pi}_K (\boldsymbol{\nabla} \cdot \widetilde{\mathbf{u}})_K \leq 0. \quad (143)$$

The third relation of (39) then yields (40).

Proof of point 3: the strict convexity of $\rho \mapsto \rho e^{\mathrm{EOS}}(1/\rho)$, relation (37) and the CFL condition (38b) imply that

$$\rho_K^{n+1} e^{\mathrm{EOS}}(\tau_K^{n+1}) = \rho_K^{n+1} e^{\mathrm{EOS}}(1/\rho_K^{n+1}) \leq \mathrm{Cvx}\left(\widetilde{\rho} e^{\mathrm{EOS}}(1/\widetilde{\rho})\right)_K = \mathrm{Cvx}\left(\widetilde{\rho} e^{\mathrm{EOS}}(\widetilde{\tau})\right)_K, \quad (144)$$

so that

$$\rho_K^{n+1} e^{\mathrm{EOS}}(\tau_K^{n+1}) + \frac{\delta t}{|K|} \sum_{\sigma \in \mathcal{E}(K)} F_{K,\sigma} e^{\mathrm{EOS}}(\widetilde{\tau}_\sigma) \leq \widetilde{\rho}_K e^{\mathrm{EOS}}(\widetilde{\tau}_K)(1 - \delta t (\boldsymbol{\nabla} \cdot \widetilde{\mathbf{u}})_K). \quad (145)$$

Thanks to (24) and (40) we have

$$\rho_K^{n+1} e^{\mathrm{EOS}}(\tau_K^{n+1}) + \frac{\delta t}{|K|} \sum_{\sigma\in\mathcal{E}(K)} F_{K,\sigma} e^{\mathrm{EOS}}(\widetilde{\tau}_\sigma) \le \rho_K^n e^{\mathrm{EOS}}(\widetilde{\tau}_K) \le \rho_K^n e(\tau_K^n) - \delta t \widetilde{\pi}_K \left(\boldsymbol{\nabla}\cdot\widetilde{\mathbf{u}}\right)_K, \quad (146)$$

which proves (41).

Proof of point 4: relation (42) is obtained by summing equations (19) and (140) and also using defintion (139).

Proof of point 5: we suppose that the CFL condition (38a) is satisfied and we consider the sum of (41) over all $K\in\mathcal{M}$ and the sum of (42) over all $\sigma\in\mathcal{E}_{\mathrm{int}}$, that is to say

$$\sum_{\sigma\in\mathcal{E}(K)} \frac{|K|}{\delta t}\left(\rho_K^{n+1} e^{\mathrm{EOS}}(\tau_K^{n+1}) - \rho_K^n e(\tau_K^n)\right) + \sum_{K\in\mathcal{E}(K)}\sum_{\sigma\in\mathcal{E}(K)} F_{K,\sigma} e^{\mathrm{EOS}}(\widetilde{\tau}_\sigma) \\ + \sum_{K\in\mathcal{E}(K)} |K| \widetilde{\pi}_K \left(\boldsymbol{\nabla}\cdot\widetilde{\mathbf{u}}\right)_K \le 0, \quad (147)$$

and

$$\sum_{\sigma\in\mathcal{E}_{\mathrm{int}}} \frac{|D_\sigma|}{\delta t}\left(\rho_{D_\sigma}^{n+1}\frac{\left|\mathbf{u}_\sigma^{n+1}\right|^2}{2} - \rho_{D_\sigma}^n \frac{|\mathbf{u}_\sigma^n|^2}{2}\right) + \sum_{\sigma\in\mathcal{E}_{\mathrm{int}}}\sum_{\varepsilon\in\widetilde{\mathcal{E}}(D_\sigma)} F_{\sigma,\varepsilon}\frac{|\widetilde{\mathbf{u}}_\varepsilon|^2}{2} \\ + \sum_{\sigma\in\mathcal{E}_{\mathrm{int}}} \widetilde{u}_{K,\sigma}^{*} \left(\boldsymbol{\nabla}\widetilde{\pi}\right)_\sigma \cdot \mathbf{n}_{K,\sigma} = \sum_{\sigma\in\mathcal{E}_{\mathrm{int}}} -\widetilde{R}_\sigma - R_\sigma^{n+1} \le 0. \quad (148)$$

Let us remark that in both (147) and (148) the conservative fluxes cancel out in the sum. Then, taking the sum of (147) and (148) and using (133) we get

$$\sum_{\sigma\in\mathcal{E}(K)} \frac{|K|}{\delta t}\left(\rho_K^{n+1} e^{\mathrm{EOS}}(\tau_K^{n+1}) - \rho_K^n e(\tau_K^n)\right) + \sum_{\sigma\in\mathcal{E}_{\mathrm{int}}} \frac{|D_\sigma|}{\delta t}\left(\rho_{D_\sigma}^{n+1}\frac{\left|\mathbf{u}_\sigma^{n+1}\right|^2}{2} - \rho_{D_\sigma}^n \frac{|\mathbf{u}_\sigma^n|^2}{2}\right) \le 0. \quad (149)$$

Inequality (149) is true for any $n\ge 0$. By dividing by δt and taking the sum over all $0\le n\le N-1$ we obtain the relation (44). □

C.3 Proofs of stability estimates for the full Euler system

Proof of proposition 5.1. Proof of point 1: we use similar lines as for (39). By combining (70b) and (24) one obtains the first inequality of (71). The second relation of (71) is a consequence of (57a) and (57d). The equilibrium at instant t^n implies that $\pi_K^n = p^{\mathrm{EOS}}(\tau_K^n, s^{\mathrm{EOS}}(\tau_K^n, e_K^n))$ so that (130) is verified with $\tau = \widetilde{\tau}_K$, $\pi = \widetilde{\pi}_K$, $\mathcal{V} = \tau_K^n$ and $\overline{s} = s_k^n$. Inequality (131) then yields the third relation of (71).

Proof of point 2: substracting relation (25) and (57c) gives

$$\frac{\rho_K^n}{\delta t}\left(\frac{(\widetilde{\pi}_K)^2}{2(a_K^n)^2} - \frac{(\pi_K^n)^2}{2(a_K^n)^2} + e^{\mathrm{EOS}}(\tau_K^n, s_K^n) - \widetilde{e}_K\right) \le -\widetilde{S}_K - \frac{\rho_K^n}{\delta t}\frac{(\widetilde{\pi}_K - \pi_K^n)^2}{2(a_K^n)^2}. \quad (150)$$

Using the second relation of (71) we get $\frac{\rho_K^n}{\delta t}\left(-\widetilde{e}_K + e^{\mathrm{EOS}}(\widetilde{\tau}_K, s_K^n)\right) \le -\widetilde{S}_K - \frac{\rho_K^n}{\delta t}\frac{(\widetilde{\pi}_K - \pi_K^n)^2}{2(a_K^n)^2} \le 0$, so that $e^{\mathrm{EOS}}(\widetilde{\tau}_K, s_K^n) \le \widetilde{e}_K$. Thanks to hypothesis (47) we get $0 \le \widetilde{e}_K$. Moreover, as $e' \mapsto s^{\mathrm{EOS}}(\widetilde{\tau}_K, e')$ is an increasing function we obtain $s_K^n \le \widetilde{s}_K$.

Proof of point 3: the proof of the first relation (73) is the same as that of (37). For the second relation of (73), consider now the energy flux in (63c), we have

$$F_{K,\sigma}\widetilde{e}_\sigma = |\sigma|\widetilde{\rho}_K\widetilde{e}_K(\widetilde{u}^*_{K,\sigma})^+ - |\sigma|\widetilde{\rho}_L\widetilde{e}_L(\widetilde{u}^*_{K,\sigma})^-, \quad \sigma = K|L \in \mathcal{E}(K). \tag{151}$$

Consequently (63c) reads

$$\begin{aligned}
\rho_K^{n+1}e_K^{n+1} &= \widetilde{\rho}_K\widetilde{e}_K - \delta t \sum_{\sigma\in\mathcal{E}(K)} \frac{|\sigma|}{|K|}\left\{\widetilde{\rho}_K\widetilde{e}_K(\widetilde{u}^*_{K,\sigma})^+ - \widetilde{\rho}_L\widetilde{e}_L(\widetilde{u}^*_{K,\sigma})^- - \widetilde{\rho}_K\widetilde{e}_K\widetilde{u}^*_{K,\sigma}\right\} + \frac{\delta t}{|K|}S_K^{n+1} \\
&= \widetilde{\rho}_K\widetilde{e}_K\left[1 - \delta t\sum_{\sigma\in\mathcal{E}(K)}\frac{|\sigma|}{|K|}\left((\widetilde{u}^*_{K,\sigma})^+ - \widetilde{u}^*_{K,\sigma}\right)\right] + \delta t\sum_{\sigma\in\mathcal{E}(K)}\frac{|\sigma|}{|K|}\widetilde{\rho}_L\widetilde{e}_L(\widetilde{u}^*_{K,\sigma})^- + \frac{\delta t}{|K|}S_K^{n+1},
\end{aligned} \tag{152}$$

which yields the second relation of (73).

Proof of point 4. Using the definition (66), we have

$$\begin{aligned}
S_{K,\sigma}^{n+1} &= \frac{|D_{K,\sigma}|}{\delta t}\frac{\rho_K^n}{2}\left|\mathbf{u}_\sigma^{n+1} - \widetilde{\mathbf{u}}_\sigma\right|^2 - \sum_{\varepsilon\in\widetilde{\mathcal{E}}(D_{K,\sigma})}\alpha_{K,\varepsilon}\frac{\widetilde{F}_{\sigma,\varepsilon}}{2}\left|\mathbf{u}_\sigma^{n+1} - \widetilde{\mathbf{u}}_\varepsilon\right|^2 \\
&= \frac{|D_{K,\sigma}|}{\delta t}\frac{\rho_K^n}{2}\left|\mathbf{u}_\sigma^{n+1} - \widetilde{\mathbf{u}}_\sigma\right|^2 - \sum_{\varepsilon\in\widetilde{\mathcal{E}}(D_{K,\sigma})}\alpha_{K,\varepsilon}\frac{\widetilde{F}^+_{\sigma,\varepsilon}}{2}\left|\mathbf{u}_\sigma^{n+1} - \widetilde{\mathbf{u}}_\sigma\right|^2 \\
&\qquad + \sum_{\varepsilon\in\widetilde{\mathcal{E}}(D_{K,\sigma})}\alpha_{K,\varepsilon}\frac{\widetilde{F}^-_{\sigma,\varepsilon}}{2}\left|\mathbf{u}_\sigma^{n+1} - \widetilde{\mathbf{u}}_{\sigma'}\right|^2 \\
&= \frac{1}{2}\left|\mathbf{u}_\sigma^{n+1} - \widetilde{\mathbf{u}}_\sigma\right|^2\underbrace{\left(\frac{|D_{K,\sigma}|}{\delta t}\rho_K^n - \sum_{\varepsilon\in\widetilde{\mathcal{E}}(D_{K,\sigma})}\alpha_{K,\varepsilon}\widetilde{F}^+_{\sigma,\varepsilon}\right)}_{\ge 0 \text{ under condition (70c)}} + \underbrace{\sum_{\varepsilon\in\widetilde{\mathcal{E}}(D_{K,\sigma})}\frac{\alpha_{K,\varepsilon}\widetilde{F}^-_{\sigma,\varepsilon}}{2}\left|\mathbf{u}_\sigma^{n+1} - \widetilde{\mathbf{u}}_{\sigma'}\right|^2}_{\ge 0},
\end{aligned}$$

Proof of point 5: let us note: $\Lambda : (\rho', \rho' e') \mapsto -\rho' s^{\mathrm{EOS}}(\frac{1}{\rho'}, \frac{\rho' e'}{\rho'})$ and remark that Λ is convex (see [41]) and $\rho' e' \mapsto \Lambda(\rho_K^{n+1}, \rho' e')$ is decreasing under assumption (48). Now, if CFL condition (70c) is verified then $S_K^{n+1} \ge 0$, so that (73) yields $\rho_K^{n+1}e_K^{n+1} \ge \mathrm{Cvx}(\widetilde{\rho e})_K$. Consequently

$$-\rho_K^{n+1}s_K^{n+1} = \Lambda(\rho_K^{n+1}, \rho_K^{n+1}e_K^{n+1}) \le \Lambda\Big(\rho_K^{n+1}, \mathrm{Cvx}(\widetilde{\rho e})_K\Big) = \Lambda\Big(\mathrm{Cvx}(\widetilde{\rho})_K, \mathrm{Cvx}(\widetilde{\rho e})_K\Big) \tag{153}$$

Using the convexity of Λ and CFL condition (38b), we then obtain

$$\begin{aligned}
-\rho_K^{n+1}s_K^{n+1} \le \mathrm{Cvx}\left(\Lambda(\widetilde{\rho}, \widetilde{\rho e})\right)_K = \mathrm{Cvx}(-\widetilde{\rho s})_K = (-\widetilde{\rho}_K\widetilde{s}_K)&\left[1 - \delta t\sum_{\sigma\in\mathcal{E}(K)}\frac{|\sigma|}{|K|}\left((\widetilde{u}^*_{K,\sigma})^+ - \widetilde{u}^*_{K,\sigma}\right)\right] \\
&+ \delta t\sum_{\sigma\in\mathcal{E}(K)}\frac{|\sigma|}{|K|}(-\widetilde{\rho}_L\widetilde{s}_L)(\widetilde{u}^*_{K,\sigma})^-,
\end{aligned} \tag{154}$$

which also reads

$$|K|(-\rho_K^{n+1} s_K^{n+1}) \leq |K|(-\widetilde{\rho}_K \widetilde{s}_K) - \delta t \sum_{\sigma \in \mathcal{E}(K)} \Big(|\sigma| (\widetilde{u}^*_{K,\sigma})^+ (-\widetilde{\rho}_K \widetilde{s}_K) + |\sigma| (\widetilde{u}^*_{K,\sigma})^- (-\widetilde{\rho}_L \widetilde{s}_L) \Big) + \delta t |K| (-\widetilde{\rho}_K \widetilde{s}_K) \left(\boldsymbol{\nabla} \cdot \widetilde{\mathbf{u}} \right), \quad (155)$$

hence relation (75).

Proof of point 6: replacing $\widetilde{\rho}_K$ thanks to (63a) into (75) and using (72) yields (76).

Proof of point 7: we consider (68c) and take the sum over all $K \in \mathcal{M}$ along with (42) and its sum over all $\sigma \in \mathcal{E}_{int}$.

$$\sum_{K \in \mathcal{M}} \frac{|K|}{\delta t} \left(\rho_K^{n+1} e_K^{n+1} - \rho_K^n e_K^n \right) + \sum_{K \in \mathcal{M}} \sum_{\sigma \in \mathcal{E}(K)} F_{K,\sigma} \widetilde{e}_\sigma + \sum_{K \in \mathcal{M}} \widetilde{\pi}_K \left(\boldsymbol{\nabla} \cdot \widetilde{\mathbf{u}} \right)_K = \sum_{K \in \mathcal{M}} \widetilde{S}_K + S_K^{n+1} \quad (156a)$$

$$\sum_{\sigma \in \mathcal{E}_{int}} \frac{|D_\sigma|}{\delta t} \left(\rho_{D_\sigma}^{n+1} \frac{\left| \mathbf{u}_\sigma^{n+1} \right|^2}{2} - \widetilde{\rho}_{D_\sigma} \frac{|\mathbf{u}_\sigma^n|^2}{2} \right) + \sum_{\sigma \in \mathcal{E}_{\rm int}} \sum_{\varepsilon \in \widetilde{\mathcal{E}}(D_\sigma)} \widetilde{F}_{\sigma,\varepsilon} \frac{|\widetilde{\mathbf{u}}_\varepsilon|^2}{2} + \sum_{\sigma \in \mathcal{E}_{\rm int}} \widetilde{u}^*_{K,\sigma} \left(\boldsymbol{\nabla} \widetilde{\pi} \right)_\sigma \cdot \mathbf{n}_{K,\sigma} = - \sum_{\sigma \in \mathcal{E}_{\rm int}} \widetilde{R}_\sigma + R_\sigma^{n+1}. \quad (156b)$$

In both (156a) and (156b) the conservative fluxes terms cancel each other in the sums. Then, adding (156a) and (156b) we see that the source terms cancel out each other by (60) and (65). Moreover, the pressure-velocity product terms also cancel out by (133), so that we get

$$\sum_{K \in \mathcal{M}} \frac{|K|}{\delta t} \left(\rho_K^{n+1} e_K^{n+1} - \rho_K^n e_K^n \right) + \sum_{\sigma \in \mathcal{E}_{int}} \frac{|D_\sigma|}{\delta t} \left(\rho_{D_\sigma}^{n+1} \frac{\left| \mathbf{u}_\sigma^{n+1} \right|^2}{2} - \widetilde{\rho}_{D_\sigma} \frac{|\mathbf{u}_\sigma^n|^2}{2} \right) = 0. \quad (157)$$

As (157) is true for any $n \geq 0$, taking the sum for $0 \leq n \leq N-1$ yields (77). □